



University of Kentucky
UKnowledge

Theses and Dissertations--Physics and
Astronomy

Physics and Astronomy


2021

A MULTI-WAVELENGTH STUDY OF THE DISK WINDS AND THEIR ROLE IN THE AGN STUDIES

Maryam Dehghanian

University of Kentucky, mde277@uky.edu

Author ORCID Identifier:

 <https://orcid.org/0000-0002-0964-7500>

Digital Object Identifier: <https://doi.org/10.13023/etd.2021.012>

[Right click to open a feedback form in a new tab to let us know how this document benefits you.](#)

Recommended Citation

Dehghanian, Maryam, "A MULTI-WAVELENGTH STUDY OF THE DISK WINDS AND THEIR ROLE IN THE AGN STUDIES" (2021). *Theses and Dissertations--Physics and Astronomy*. 80.

https://uknowledge.uky.edu/physastron_etds/80

This Doctoral Dissertation is brought to you for free and open access by the Physics and Astronomy at UKnowledge. It has been accepted for inclusion in Theses and Dissertations--Physics and Astronomy by an authorized administrator of UKnowledge. For more information, please contact UKnowledge@lsv.uky.edu.

STUDENT AGREEMENT:

I represent that my thesis or dissertation and abstract are my original work. Proper attribution has been given to all outside sources. I understand that I am solely responsible for obtaining any needed copyright permissions. I have obtained needed written permission statement(s) from the owner(s) of each third-party copyrighted matter to be included in my work, allowing electronic distribution (if such use is not permitted by the fair use doctrine) which will be submitted to UKnowledge as Additional File.

I hereby grant to The University of Kentucky and its agents the irrevocable, non-exclusive, and royalty-free license to archive and make accessible my work in whole or in part in all forms of media, now or hereafter known. I agree that the document mentioned above may be made available immediately for worldwide access unless an embargo applies.

I retain all other ownership rights to the copyright of my work. I also retain the right to use in future works (such as articles or books) all or part of my work. I understand that I am free to register the copyright to my work.

REVIEW, APPROVAL AND ACCEPTANCE

The document mentioned above has been reviewed and accepted by the student's advisor, on behalf of the advisory committee, and by the Director of Graduate Studies (DGS), on behalf of the program; we verify that this is the final, approved version of the student's thesis including all changes required by the advisory committee. The undersigned agree to abide by the statements above.

Maryam Dehghanian, Student

Dr. Gary Ferland, Major Professor

Dr. Christopher Crawford, Director of Graduate Studies

A MULTI-WAVELENGTH STUDY OF THE DISK WINDS AND THEIR ROLE IN
THE AGN STUDIES

DISSERTATION

A dissertation submitted in partial
fulfillment of the requirements for the
degree of Doctor of Philosophy in the
College of Arts and Sciences at the
University of Kentucky

By
Maryam Dehghanian
Lexington, Kentucky

Director: Dr. Gary Ferland, Professor of Physics and Astronomy
Lexington, Kentucky
2021

Copyright© Maryam Dehghanian 2021
<https://orcid.org/0000-0002-0964-7500>

ABSTRACT OF DISSERTATION

A MULTI-WAVELENGTH STUDY OF THE DISK WINDS AND THEIR ROLE IN THE AGN STUDIES

Active galactic nuclei (AGNs) are located at the centers of massive galaxies and are the most luminous objects in the universe. Each AGN embeds a super-massive black hole which produces outflows of gas, or winds. These winds are important because they provide a reasonable physical basis for the connections between the black hole and the properties of their host galaxy. While AGNs have been extensively studied, several fundamental questions about them are yet to be answered. These include the structure and dynamics of the central source and their winds, and questions regarding the evolution of these galaxies.

NGC 5548 is a bright and well-studied AGN that has been the target of many monitoring campaigns since 1987. The most extensive observations were in 2013 and 2014, in which its emission and absorption lines behaved in an anomalous way that had never before been seen. For a two-month period during the observations, emission and absorption lines did not respond to the variations of the continuum – the HST team said that the spectral lines had “gone on holiday”. The main goal of my thesis is to model the pan-spectral data available for the NGC 5548 not only to explain the abnormal holiday, but also to use the data as a laboratory to investigate the inner structure of the AGNs and their evolution.

Here I explain the physics by which the variations of a disk wind produce the observed holiday. The disk wind acts as a shield between the central source and the clouds that produce the emission and absorption lines. I simulate the behavior of the wind to explain the holiday, and also investigate and model the general characteristics of such winds to predict their effects on the observations. My newly proposed models lead to novel tools to detect the footprint of the disk winds in the observations and track their evolution. This project is a systematic study of UV and X-ray spectroscopic signatures of the wind in the NGC 5548 and is widely applicable to the family of AGNs. Although the comprehensive data set that is used here belongs to one AGN, the results are applicable to all AGNs.

KEYWORDS: Active Galaxy, Black Hole, Disk Wind, Emission Lines, Absorption Lines

Maryam Dehghanian

February 10, 2021

A MULTI-WAVELENGTH STUDY OF THE DISK WINDS AND THEIR ROLE
IN THE AGN STUDIES

By
Maryam Dehghanian

Dr. Gary Ferland

Director of Dissertation

Dr. Christopher Crawford

Director of Graduate Studies

02/10/2021

Date

Dedicated to my beloved husband and daughter.

ACKNOWLEDGMENTS

I would like to express my gratitude and appreciation for my advisor, Dr. Gary. J. Ferland, for all the support and encouragement he gave me throughout my Ph.D. work. Without his guidance and constant feedback this project would not have been successful.

I would also like to thank Dr. Bradley M. Peterson and Gerard. A. Kriss for their support and contribution to this research.

My thanks also go to Dr. Francisco Guzman and Dr. Marios Chatzikos who were always so helpful and provided me with their support and collaboration throughout my dissertation.

Finally, I would like to thank my husband, Alireza Valian, for all of his devotion and love during my Ph.D. studies.

TABLE OF CONTENTS

Acknowledgments	iii
List of Tables	vi
List of Figures	vii
Chapter 1 INTRODUCTION	1
1.1 What is an AGN?	1
1.2 NGC 5548 as a template for AGNs	2
1.3 Discussion and summary	4
Chapter 2 THE ABSORPTION-LINE HOLIDAY	5
2.1 The geometry and the obscurer	5
2.2 The holiday	6
2.3 The “standard” model of component 1	7
2.4 What happened?	10
2.5 Physics behind the “holiday”	12
2.6 Testing the covering factor model	17
2.7 Discussion and summary	19
Chapter 3 THE EMISSION-LINE HOLIDAY	21
3.1 A baseline BLR with changing luminosity	21
3.2 The SED transmitted through the equatorial obscurer	23
3.3 The response of the BLR to changes of the transmitted continuum	25
3.4 Discussion and summary	28
Chapter 4 A NOVEL APPROACH TO IDENTIFY THE DISK WIND	30
4.1 Cloudy modeling	30
4.2 Wind properties from the observations	31
4.3 Discussion and summary	37
Chapter 5 AN ATLAS OF UV AND X-RAY SPECTROSCOPIC SIGNATURES OF THE DISK WIND IN NGC 5548	41
5.1 The disk wind	41
5.2 The effects of different parameters-general considerations	43
5.3 LIMITS ON THE OBSCURER: THE GLOBAL COVERING FACTOR	54
5.4 EMISSION FROM THE WIND	57
Chapter 6 CONCLUSION	62
Bibliography	63

Vita 67

LIST OF TABLES

5.1	Upper limits for the ionization parameter to have various ionization fronts. . . .	48
-----	--	----

LIST OF FIGURES

2.1	The geometry of the emission and absorption components discussed in this paper. The line of sight obscurer covers 70% to 100% of the X-ray source (Mehdipour et al. 2016). The gray clouds show other possible obscurers. These will be discussed in the next paper in this series. The blue blobs indicate the BLR clouds surrounding the source. Component 1, the narrow absorption line component with the highest outflow velocity (-1165 km s^{-1}), is also shown. Component 1 is the absorbing component studied in this paper.	5
2.2	Both panels show the arbitrarily scaled FUV continuum in red, as a function of Heliocentric Julian Date -24400000 . The upper panel shows the equivalent width of the $\text{Ly}\alpha$ absorber of Component 1 in blue and the lower panel shows the equivalent width of the corresponding NV, $\lambda 1238$ absorption line. Shaded area indicates the time in which the "holiday" is happening.	7
2.3	The intrinsic (unobscured) SED available in version 17 of <code>Cloudy(C17)</code> is shown in dashed-style black line. It was zero outside the indicated range. The green line shows the improved SED (Mehdipour et al. (2015)) which will be implemented in future versions of <code>Cloudy</code>	8
2.4	The expected SED transmitted through the obscurer and striking Component 1. Each line segment shows the energy required to produce the ion (left end) and to destroy the ion (right end). In this Figure, we assumed that the obscurer fully covers the continuum source. The column density to make the transmitted SED is $N(\text{H}) = 1.2 \times 10^{22} \text{ cm}^{-2}$	9
2.5	This shows how Component 1 column densities change as the ionization parameter changes. The hydrogen column density is divided by 1000 for comparison purposes. The solid lines are correlated species while the dashed lines are decorrelated. These changes are unlike those seen in the holiday, ruling out changes in U alone as the reason for the holiday.	11
2.6	The variations of the SED striking Component 1 for different LOS CFs. The Arav et al. (2015) ionization parameter is reproduced at zero coverage. The Figure indicates the soft and hard X-ray energies, i.e., 0.3–1.5 keV and 1.5–10 keV (Mehdipour et al. 2016).	12
2.7	The effects of changes in the obscurer LOS CF upon the column densities observed by <i>HST</i> . Low-ionization species (solid lines) remained correlated while high ionization (dashed) species were decorrelated during the holiday, as expected from changes in the obscurer covering factor. The ionization parameters adopted for the obscurer and Component 1 are $\log \xi = -1.2$ (erg cm s^{-1}) and $\log U = -1.5$, respectively.	13
2.8	Variations of the column densities of different ionization stages as the obscurer LOS CF changes. Si, C, and He are shown in three panels, from top to bottom, respectively.	14

2.9	Diffuse emission field at the midplane of Component 1 with 96% obscuration. The left terminus of the horizontal lines shows the minimum energy needed to destroy the ion and produce the higher stage ion. RRC stands for radiative recombination continua and H I RRC is the Lyman continuum emission	15
2.10	Opacity per hydrogen atom is shown as a function of energy. This shows the total opacity at the Component 1 midplane. The vertical axis has been scaled by $h\nu^3$ for clarity, as described in the text.	16
2.11	The upper panel shows the radiation field striking Component 1 as the blue line and the radiation field at the midplane of the cloud as the red line. The lower panel shows the photoionization rate at each energy.	17
2.12	The EW of the $\text{Ly}\alpha$ absorption line in Component 1 is shown as the blue line in the upper panel and the EW of the corresponding NV absorption line is shown in the lower panel. The red line shows the <i>HST</i> FUV continuum while the green line is the LOS covering factor of the obscurer derived from the X-ray hardness ratio as defined by Mehdipour et al. (2016). $\text{Ly}\alpha$ absorption line is correlated with the <i>HST</i> continuum while NV absorption line anticorrelates with the covering factor.	18
2.13	The effects of changes in the LOS CF on the ionic column densities over the full range of covering factor are shown. The dashed and solid lines indicate decorrelated and correlated species, respectively. Their behavior swaps around in the low and high covering factor limits, offering a test of the variable covering factor model. In this models, the ionization parameter for Component 1 is $\log U = -1.5$	19
3.1	Diagram of the disk wind in NGC 5548 (not to scale). The BH is surrounded by the accretion disk. At larger radii the BLR is indicated by orange/red turbulent clouds. The disk wind rises nearly vertically from the surface of the accretion disk, where it has a dense, high-column-density base. At higher elevations, radiation pressure accelerates the wind and bends the streamlines down along the 30 degree inclination of the observer's LOS to the rotation axis of the disk (Kaastra et al. 2014).	22
3.2	EW of emission lines vs. the flux of hydrogen ionizing photons. The EWs are normalized to the continuum at 1367Å. For most of the lines, the predicted EWs decrease when $\phi(\text{H}) > 10^{20}$, the observed behavior. The bow tie shows the range of β observed for various lines before the holiday.	23
3.3	The SED transmitted through equatorial obscurer and incident upon the BLR is shown for three different values of the hydrogen density. The unextinguished SED is also shown. The SED is dramatically dependent on the hydrogen density of the obscurer. High hydrogen densities produce strong absorption in XUV region and strong emission in FUV/optical regions.	25
3.4	EW of all observed emission lines and Mg II versus the density of the equatorial obscurer. The plot is divided into three different cases, labeled at the top, based on the behavior of the EWs. The cases are described in the text. The shaded area shows the range in which the holiday observed in NGC 5548 will be produced.	26

3.5	The total spectrum, including transmitted and reflected emission from the BLR for two densities of the equatorial obscurer. The upper panel shows the the UV regions and the lower panel shows the optical wavelengths. This Figure shows how phenomena similar to changing-look AGN, in which a Seyfert I turns into a Seyfert II, would occur without changes in the intrinsic luminosity of the AGN	27
4.1	The contours show total hydrogen column density of the equatorial obscurer as a function of the flux of ionizing photons and the hydrogen density. The orange line indicates the LOS obscurer's column density (D19a) and the dashed black line shows the location of the BLR based on the observed CIV lag.	32
4.2	Upper four panels show the predicted EW of strong lines emitted by the equatorial obscurer as the contours. The colored lines indicate the HST observed value and arrows show the direction in which the equatorial obscurer must be chosen in order for its emission to not dominate the HST emission lines. All the EWs are relative to the 1215 Å continuum. The lowest panel shows the predicted luminosity of Fe Kα as the contours and the blue lines show the XMM-Newton observed values.	34
4.3	The left panel maps the Thomson scattering optical depth and the right panel maps the temperature of the obscurer. A and B are two regions with allowed properties of the equatorial obscurer. The red star indicates our preferred model, which is the most consistent with all observational constraints	35
4.4	This Figure compares our model with the observations from HST, XMM-Newton, and NuSTAR. Panels A & B show the case for CIV, for which the obscurer produces a very broad component (panel A, blue) with an EW of half of that produced by the BLR (panel A, red). Panels C & D show the case for Fe Kα, for which the obscurer produces a very broad component (panel C, blue) with an EW equal to that produced by the BLR (panel C, red). It is plausible that a broad base similar to CIV is present, although the S/N is not high enough to say for sure. In both cases our predictions are very similar to the observations, suggesting that the disk wind could be responsible for the observed very broad emission line components.	37
4.5	Cartoon of the disk wind in NGC 5548 (not to scale). The disk wind (blue) surrounds the central black hole and extends to the line of sight to HST in the upper right corner. The BLR is shown as the orange cloud around the disk. The green cloud at the upper right shows the absorbing cloud discussed in D19a. The bright region in the lower part of the wind indicates that the wind is a major contributor to the very broad components of the observed emission lines .	40

5.1	Left panel: The obscurer's transmitted SED. As the lines show the transmitted SED is very sensitive to the ionization parameter in soft X-ray energies. Right panel: total emission(sum of the transmitted and reflected continua plus attenuated incident continuum) from the obscurer for different values of the ionization parameter. The attenuated incident continuum is included. The spectra represent $\log \xi = 2, 1, 0.5, 0,$ and -0.5 from top to bottom. (There is an animation associated with this Figure which shows how the transmitted SED responses to the variations of the ionization fraction).	44
5.2	Top panel shows the variation of atomic hydrogen column density as the ionization parameter changes. The bottom panel shows the ratio of $399\text{\AA}/1365\text{\AA}$ as a function of the ionization parameter.	46
5.3	The ionization fraction of the noted ions as a function of the depth into the cloud (lower X-axis) in correspondence with the hydrogen column density (upper X-axis). The dashed lines show the depths corresponding to cases 1, 2, and 3, for assumptions of fixed gas density and incident ionizing photon flux. Figure 5.4 shows how the transmitted and emitted SEDs would be for these three different depths.	50
5.4	: Left panel: transmitted SED in different depths of a thick cloud. Right panel: total emission (sum of the transmitted and reflected continua plus attenuated incident continuum) from the obscurer for the same three cases.	51
5.5	Changes in the SED for different values of the obscurer hydrogen density for two models of ionization parameters. Both upper panels have ionization parameter $\log \xi = -1.2 \text{ erg cm s}^{-1}$. Upper left panel shows the results for the transmitted SED and the upper right shows the results for the total emission from the obscurer (sum of the transmitted and reflected continua plus attenuated incident continuum). Lower panels show the same concept for an ionization parameter $\log \xi = 0.5 \text{ erg cm s}^{-1}$	52
5.6	Top panel shows the variation of atomic hydrogen column density as the ionization parameter changes, for three different hydrogen densities. The bottom panel shows the ratio of $399\text{\AA}/1365\text{\AA}$ as a function of the ionization parameter for the same three hydrogen densities.	53
5.7	Changes in the SED for different values of the metallicity for two models of ionization parameters. Both upper panels have ionization parameter $\log \xi = -1.2 \text{ erg cm s}^{-1}$. Upper left panel shows the results for the transmitted SED and the upper right shows the results for the total emission from the obscurer (sum of the transmitted and reflected continua plus attenuated incident continuum). Lower panels show the same concept for an ionization parameter $\log \xi = 0.5 \text{ erg cm s}^{-1}$	54
5.8	Top panel shows the variation of the obscurer atomic hydrogen column density as the ionization parameter changes for two different values of the metallicity. The bottom panel shows the ratio of the $399\text{\AA}/1365\text{\AA}$ transmitted continuum as a function of the ionization parameter.	55

5.9	Changes in the luminosity of the emission features of the obscurer as the separation between the obscurer and the black hole varies between 10^{15} and 10^{19} cm. The luminosities are predicted for full source coverage. The observed values refer to a combination of broad, medium broad, and very broad emission components observed by HST.	56
5.10	The EW of CIV emission line as a function of both the flux of hydrogen ionizing photons and the hydrogen density. Different panels show the variation of the EW for each of the discussed cases. The intervals between decades are logarithmic in 0.2 dex steps.	58
5.11	The EW of Ly α emission line as a function of both the flux of hydrogen ionizing photons and the hydrogen density. Different panels show the variation of the EW for each of the discussed cases.	59
5.12	The EW of HeII emission line as a function of both the flux of hydrogen ionizing photons and the hydrogen density. Different panels show the variation of the EW for each of the discussed cases.	59
5.13	The EW of SiIV emission line as a function of both the flux of hydrogen ionizing photons and the hydrogen density. Different panels show the variation of the EW for each of the discussed cases.	59
5.14	The EW of Fe K α emission line as a function of both the flux of hydrogen ionizing photons and the hydrogen density. Different panels show the variation of the EW for each of the discussed cases.	60
5.15	The EW of H β emission line as a function of both the flux of hydrogen ionizing photons and the hydrogen density. Different panels show the variation of the EW for each of the discussed cases.	60

Chapter 1 INTRODUCTION

1.1 What is an AGN?

AGNs (Active Galactic Nuclei) are the compact central regions of massive galaxies and the most luminous objects in the universe. Because of their high luminosity, they can be detected at very high redshift and emit across the entire electromagnetic spectrum. This brightness results from the accretion of matter into a super-massive black hole (SMBH) at their center. The mass of the central black hole and the mass accretion rate are the two most important properties scientists wish to determine (Peterson & Grier 2012).

The main sub-classes of AGNs are called “quasars” and “Seyfert” galaxies. Quasars are extremely luminous with a tremendous power resulting from the accretion of matter into their central super massive black hole. Their super massive black hole has a mass ranging from millions to billions of times the solar mass. Seyfert galaxies are known to have high surface brightness and their spectra includes strong, high-ionisation emission lines. They are powered by the same process as in quasars and have a luminosity between 10^8 and 10^{11} solar luminosities. The principal difference between these two categories is due to the amount of the energy distributed by the central engine: In quasars the nuclear source is 100 times brighter than all of the stars included in the galaxy, however in a Seyfert galaxy the brightness of the nucleus is almost equal to the total brightness of the stars (Peterson 1997).

1.1.1 super massive black hole

It is now broadly accepted that SMBHs are present in most massive galaxies (Kormendy & Richstone 1995; King 2003). This implies that most of the galaxies had been an AGN when the black hole was in an active phase (Lynden-Bell 1969). Furthermore, the presence of an observed robust correlation between the black hole and bulge mass (Kormendy & Richstone 1995; Magorrian et al. 1998; Gebhardt et al. 2000a; Ferrarese & Merritt 2000) shows that there is a relation between the evolution of the central black hole and its host galaxy. These show that investigating the structure of the AGN and black hole mass will provide crucial information regarding the evolution of the massive galaxies (Gebhardt et al. 2000; King 2003; Häring & Rix 2004; McLure & Dunlop 2004).

Measuring the mass of the central black hole is challenging. There are indirect methods such as the M - σ relation that correlate stellar velocity dispersions with the mass (Ferrarese & Merritt 2000; Gebhardt et al. 2000). The relationship between black hole mass and the galactic bulge luminosity is another way to estimate the mass of the BH. This “Magorrian” relationship (Magorrian et al. 1998) is an indirect method to estimate the BH mass (Bentz et al. 2009). The good correlation between the mass of the central black hole and the physical properties of the surrounding stellar bulge provides evidence that black holes play a key role in the evolution of galaxies (Häring & Rix 2004).

Reverberation mapping (RM) is the fundamental method for determining the inner structure and mass of AGNs. RM measures the “lag” between the continuum and the

emission-line variations. This time delay reflects the distance between the central continuum source and the broad line region (BLR). One can find the mass from the velocity, determined by the Doppler broadening of the line, and the distance, determined from the lag, by applying the virial theorem. Having the black hole mass and AGN geometry in hand, we can find answers for questions like; How does the black hole mass correlate with properties of the galaxy? How can these be used to trace the evolution of galaxies through feedback processes, measure the black hole mass, and chemical evolution of the galaxy?

Determination of AGN structure is possible through studying its outflows, the disk winds. These outflows are powerful highly ionized winds which are a common feature in X-ray and UV spectra of luminous AGNs. They are likely to play a role in the established relationship between the SMBHs and their surrounding environment (King & Pounds, 2015). These winds might affect the evolution of both the black hole and their host galaxies (Hamann et al. 2019). This supports the idea that AGN winds are an effective tool to transfer energy to the intergalactic medium (IGM) as required by the existence of large-scale outflows in most ultraluminous infrared galaxies (Tombesi et al. 2015). Understanding the mechanism of the outflows is the path toward understanding the evolution of the quasars and galaxies.

1.2 NGC 5548 as a template for AGNs

NGC 5548 is a Type I Seyfert galaxy with a bright active nucleus. It is approximately 75 Mpc away with a redshift $z = 0.017$. This object was one of the first AGNs in which broad emission-line flux variability was detected (Peterson et al. 1982; Stirpe, de Bruyn, & van Groningen 1988) and one of the first AGNs for which extended monitoring campaigns were undertaken (Peterson 1987; Netzer et al. 1990; Rosenblatt & Malkan 1990; Wamsteker et al. 1990). This target has been intensively monitored since the 1970s in which broad emission-line flux variability was detected and for which extended monitoring campaigns were undertaken. It provides a unique long-term baseline for exploring the time-dependence of emission and absorption-line variability, and a test of reverberation results that ought to be immutable over time (e.g., the BH mass). As explained below, the most intensive observations of this source had been performed in 2014 by the STORM project, in which some exceptional discoveries were uncovered.

In 2013 and 2014, NASA & ESA awarded an unprecedented amount of time on six space observatories (Hubble space telescope (HST), Chandra, Swift, INTEGRAL, NuSTAR, and XMM-Newton), to make a definitive study of NGC 5548. The “AGN space telescope and optical reverberation mapping (STORM)” project (DeRosa et al. 2015; Edelson et al. 2015; Fausnaugh et al. 2016; Goad et al. 2016; Mathur et al. 2017; Pei et al. 2017; Starkey et al. 2017; Dehghanian et al. 2019a; Kriss et al. 2019; Horne et al. 2020; Dehghanian et al. 2020; Williams et al. 2020; Dehghanian et al. 2021) and the “Anatomy of the AGN NGC 5548” (Kaastra et al. 2014; Mehdipour et al. 2015, 2016; Arav et al. 2015; Ursini et al. 2015; Di Gesu et al. 2015; Whewell et al. 2015; Ebrero et al. 2016; Cappi et al. 2016) campaign carried out the observations and revealed some surprising behavior.

1.2.1 The anatomy campaign: the line-of-sight obscurer

The “Anatomy of the AGN in NGC 5548” campaign, hereafter “the anatomy” campaign, observed the AGN in 2013 and 2014 using the XMM-Newton, Swift, NuSTAR, INTEGRAL, Chandra, and HST satellites along with two ground-based observatories (Mehdipour et al. 2015). The main result of these extensive observations was to detect a heavy absorption in X-ray spectra of NGC 5548 (Mehdipour et al. 2015). This was the first time that such a heavy absorption was detected in NGC 5548. This absorption was caused by an obscurer located between the observer and the black hole (Kaastra et al. 2014). The obscurer is an ionized gas that filters the spectral energy distribution (SED) produced by the black hole and accretion disk before striking the absorbing cloud. As explained by Kaastra et al. (2014) and only based on the X-ray analysis, the obscurer has a hydrogen density of $1.2 \times 10^{26} \text{m}^{-2}$ and $\log \xi = -1.2$ (in units of 10^{-9}W m) and covers 86% of the X-ray source and up to 30% of the UV source. Later, by taking UV data into account, higher ionization parameters were estimated for the obscurer (Cappi et al. 2016; Kriss et al. 2019).

Below, I explain that this obscurer is the upper part of a disk wind which originates from the vicinity of the black hole and extends into our line of sight. During this study I explore the characteristics of such disk wind to show how they affect the intrinsic SED and emission/absorption lines, causing complications in the mass-measurement methods such as RM.

1.2.2 The STORM campaign: the holidays

The AGN STORM campaign monitored NGC 5548 for a 6-month period in 2014 from January to July. During almost 120 days of the campaign, the BLR emission exhibited the expected correlation with the continuum. The lines and the continuum emission started to decorrelate about 75 days after the first HST observation and continued for 60 to 70 days (Goad et al. 2016). The abnormal observed behavior is called “the holiday”. The lines then returned to their normal behavior. Goad et al. (2016) and Pei et al. (2017) note that the strong and broad emission lines became significantly fainter (e.g. in CIV and H β) during the holiday.

At almost the same time, a very similar anomaly was detected in some of the narrow absorption lines (Kriss et al. 2019; Dehghanian et al. 2019a), called the absorption-line holiday. Based on these observations, the lower-ionization lines continued to correlate with the observed UV continuum, while the higher-ionization did not.

Nothing like these holidays had been observed in any AGN and were discovered in NGC 5548, this is probably because the data available for the NGC 5548 is the largest and the most complete data set available for a single AGN. Below I explain that this behavior may easily happen in any AGN but not be noticed without extensive HST data. Such holidays affect the observations dramatically, so must be explained and considered in all AGN investigations.

1.3 Discussion and summary

Measuring the masses of the black holes is the top priority in most AGN studies. Among the available approaches to determine the BH mass, reverberation mapping is the only direct way to find the geometry of the inner regions of AGNs, the mass of the black hole, and their effects on the evolution of massive galaxies. This method relies on a causal connection between variations of the continuum source and the formation of the emission and absorption lines. This makes understanding the holidays in NGC 5548 so important: the holiday is a time in which the causal connection was disappeared and fundamental atomic physics did not seem to work. The holiday tells us that these models are incomplete and brings into question all existing interpretations.

Below, I investigate the holidays and explain the process by which such anomalies happen. My modeling demonstrates, for the first time, the importance of “cloud shadowing”, in which one cloud partially blocks the SED ionizing other clouds. The now-standard “LOC”¹ model of the BLR (Baldwin et al. 1995), and all other BLR theories, ignore the effects of cloud shadowing and assume that all clouds see an unobscured SED. Shadowing may be the missing ingredient in understanding the physics of AGN spectra. In this way, the lessons of the two large space-based campaigns on NGC 5548 have implications for all AGN research and will influence extragalactic astrophysical studies.

In this study, I use the pan-spectral data from the Anatomy and STORM observations and simulate the behavior of the NGC 5548. I create `Cloudy` models to predict the behavior of the AGN and explain the physics behind the holidays. The outcome includes a physics-based explanation for the holidays as well as proposing a new geometry for the AGN. I also introduce novel tools to track the evolution of the disk winds in all AGNs.

The rest of this study is structured as follows. In Chapter 2, the absorption-line holiday and the physics behind it are explained. These are followed by a Chapter explaining the emission-line holiday and proposing a new geometry for the AGN NGC 5548. In Chapter 4, I introduce a novel method by which it is possible to determine the characteristics of the disk wind based on single-spectrum observations. Finally, Chapter 5 is dedicated to the general characteristics of the disk winds and their possible effects on the transmitted and emitted SEDs under different circumstances.

I developed a toolkit which enables other astronomers to detect the presence of the disk winds and trace their evolution when having a similar dataset available. I also predicted how a variety of disk winds with different properties will alter the SED and affect the observations. These simulations are available as an atlas that can be used for all wind-related studies. The published results from this research form a quarter of all the papers published during the STORM campaign, with three first-author papers by me. These papers plus a first-author letter published in the *Astrophysical Journal Letter* (ApJL) provide the only physical model ever proposed for the observed holidays and are widely applicable to future AGN studies.

¹locally optimally emitting cloud

Chapter 2 THE ABSORPTION-LINE HOLIDAY

2.1 The geometry and the obscurer

Historically, our line of sight to the central regions of NGC 5548 has been fairly clear, with no heavy obscuration in the soft X-ray, although “warm absorbers” are present (Mathur, Elvis & Wilkes 1995; Kaastra et al. 2000). Dramatic changes in the broadband soft X-ray absorption occurred and were interpreted as being due to a cloud, “the obscurer”, passing across our line of sight (Kaastra et al. 2014; Mehdipour et al. 2016). This kind of heavy obscuration had never been seen before in NGC 5548 although a similar extinction occurred in NGC 4151 (Ferland & Mushotzky 1982). Soft X-ray absorption by the obscurer was first observed in NGC 5548 in 2012 and 2013 (Mehdipour et al. 2016; Arav et al. 2015). Here we briefly summarize the geometry inferred by the “Anatomy” series of papers (Kaastra et al. 2014; Mehdipour et al. 2015, 2016; Arav et al. 2015; Ursini et al. 2015). Figure 2.1 shows a sketch of the overall geometry, including the black hole and accretion disk which produce the intrinsic (unobscured) SED. The observer is located in the direction of the HST icon.

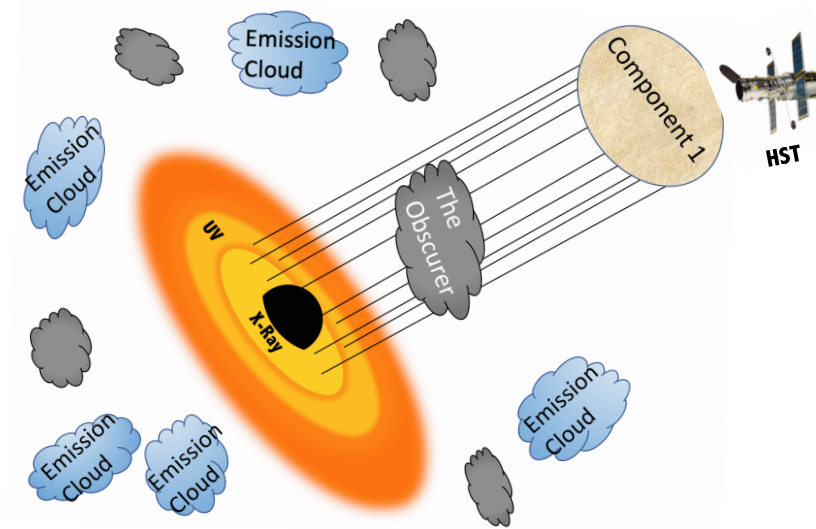


Figure 2.1: The geometry of the emission and absorption components discussed in this paper. The line of sight obscurer covers 70% to 100% of the X-ray source (Mehdipour et al. 2016). The gray clouds show other possible obscurers. These will be discussed in the next paper in this series. The blue blobs indicate the BLR clouds surrounding the source. Component 1, the narrow absorption line component with the highest outflow velocity (-1165 km s^{-1}), is also shown. Component 1 is the absorbing component studied in this paper.

A set of six intrinsic, narrow FUV¹ absorption lines potentially associated with the X-

¹We refer to the region 6 – 13.6 eV (912 Å to 2000 Å) as FUV; 13.6 – 54.4 eV (228 Å to 912 Å) as EUV;

ray warm absorber in NGC 5548 (Mathur, Elvis & Wilkes 1995) have been studied in detail by Mathur, Elvis & Wilkes (1999), Crenshaw et al. (2003), Arav et al. (2015) and Kriss et al. (2019). They are numbered from 1 to 6 in order of decreasing outflow velocity from -1165 km s^{-1} to $+250 \text{ km s}^{-1}$. In this chapter, we specifically study the cloud producing Component 1, which is also illustrated in Figure 2.1. Component 1 is the closest narrow FUV absorber to the central source, and it is the target of our study since it shows the most dramatic changes during the obscuration (Arav et al. 2015). This component also has the greatest assortment of associated UV absorption lines, permitting its characteristics to be determined in detail. The full physical properties of this component were derived by Arav et al. (2015). In particular, it has a density of $\log n_e = 4.8 \pm 0.1 \text{ cm}^{-3}$, as measured using the metastable absorption lines of CIII and SiIII. This leads to a well determined distance of $3.5 \pm 0.1 \text{ pc}$, placing it outside the BLR but within the narrow-line region (NLR) (Peterson et al. 2013).

Little is known about the density and location of the obscurer, but the ionization state, inferred high density, the kinematics, absorption line profiles, and the covering factors all suggest an origin in the BLR (Kaastra et al. 2014; Di Gesu et al. 2015; Mehdipour et al. 2015). BLR lags of two days to \sim ten days would imply a distance of between $6 \times 10^{15} - 3 \times 10^{16} \text{ cm}$ (DeRosa et al. 2015). The soft X-ray observations show that the obscurer does not fully cover the X-ray source. The covering factor varied between 0.7 and 1.0 over the period 2012 to 2015 (Mehdipour et al. 2016). This change may be caused by either transverse motions of the obscurer, changes in its internal structure, or changes in the size of the X-ray source (Mehdipour et al. 2016). Finally, it is possible that other obscurers lie within the central regions, as shown in Figure 2.1.

2.2 The holiday

In photoionization equilibrium, there is a correlation between the brightness of the ionizing radiation field and the ionization state of the gas. Reverberation measurements rely on this, with the only complication being the time lag caused by the finite speed of light. ‘‘Holidays,’’ where the correlation breaks down, are not expected. This section outlines the absorption and emission line holidays that occurred during the AGN STORM campaign.

2.2.1 Narrow absorption lines and their holiday

Some, but not all, of the Component 1 absorption lines displayed a holiday similar to the emission lines. Three low-ionization species — HI, SiII, and CII — showed good correlations with the HST FUV continuum, while the higher-ionization species — SiIII, SiIV, CIII, CIV, and NV — showed decorrelated behavior (Kriss et al. 2019). Figure 2.2 shows examples of both behaviors, Ly α and NV λ 1238. The red line shows the arbitrarily scaled HST FUV continuum while the blue lines are Component 1 absorption line equivalent widths (EW). Both lines correlate for most of the campaign, but, like the broad emission lines, there is an almost 70-day period when NV is decorrelated.

and 54.4 eV to few hundred eV (less than 228 Å) as XUV.

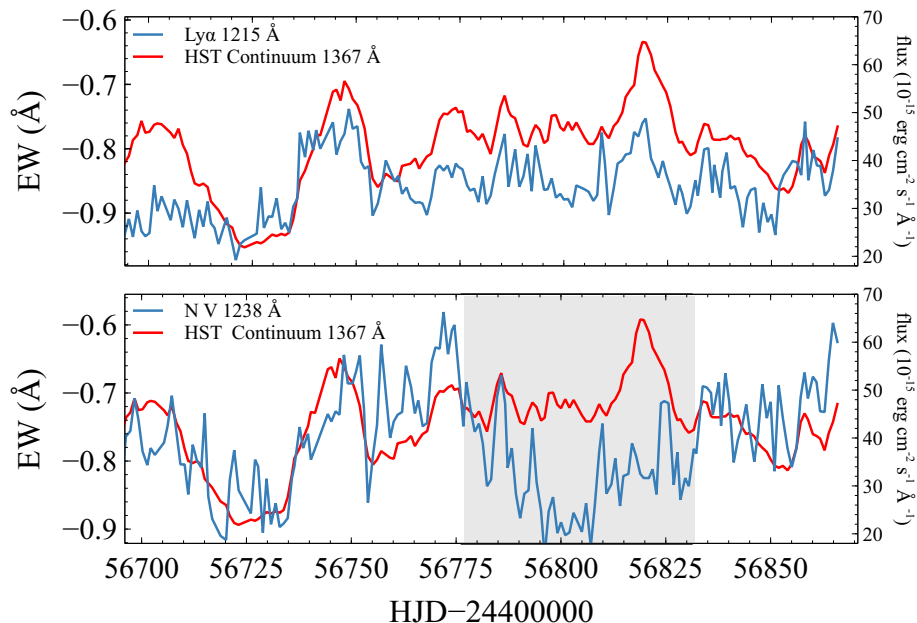


Figure 2.2: Both panels show the arbitrarily scaled FUV continuum in red, as a function of Heliocentric Julian Date -24400000 . The upper panel shows the equivalent width of the Ly α absorber of Component 1 in blue and the lower panel shows the equivalent width of the corresponding NV, $\lambda 1238$ absorption line. Shaded area indicates the time in which the "holiday" is happening.

2.3 The “standard” model of component 1

Below we use photoionization models to investigate why some absorption lines correlate with the FUV continuum and some do not. We first adopt the intrinsic SED emitted by the accretion disk, shown in Figure 2.3. This was derived by continuum modeling during the multi-wavelength campaign data on NGC 5548 (Mehdipour et al. 2015) and is used in all calculations presented below. This is based on a Comptonized thermal accretion disk model. This model was derived using simultaneous, coordinated multiwavelength observations including FUV and soft X-ray (Kaastra et al. 2014) and hard X-ray continua (Ursini et al. 2015). This SED was incorporated into the developmental version of `Cloudy`, most recently described by Ferland et al. (2017), and will be available in the next release. We use this developmental version throughout this paper. Version 17, the latest public release of `Cloudy`, included an NGC 5548 SED derived by Tek P. Adhikari from CAMK (Warsaw), by digitizing figure 10 of Mehdipour et al. (2015). That SED did not include data for energies not included in the published figure. The improved SED used by Mehdipour et al. (2015) covers the entire electromagnetic spectrum, and includes the observed Fe $K\alpha$ line.

The principal conclusion of Hopkins et al. (2004) is that extinction in SDSS quasars is typically $E(B-V) = 0.013$ mag with an SMC-like extinction curve. There are, of course, “red quasars” that are heavily extinguished (Gaskell 2017), but NGC 5548 is not one of them. There are hard X-ray observations with NuSTAR and INTEGRAL observatories, and the

SED model that we use matches the observed flux and shape of the hard X-ray continuum (Ursini et al. 2015). The SED model that was derived by Mehdipour et al. (2015) is fully consistent with simultaneous observations taken with multiple observatories from optical to hard X-rays.

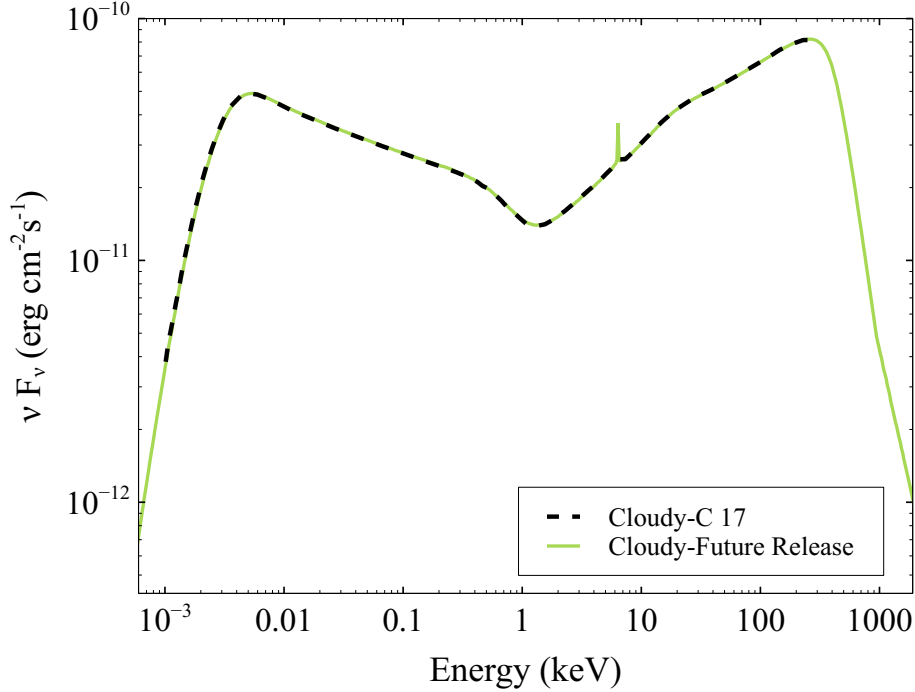


Figure 2.3: The intrinsic (unobscured) SED available in version 17 of `Cloudy`(C17) is shown in dashed-style black line. It was zero outside the indicated range. The green line shows the improved SED (Mehdipour et al. (2015)) which will be implemented in future versions of `Cloudy`.

We adopt the obscurer parameters — $N(\text{H}) = 1.2 \times 10^{22} \text{ cm}^{-2}$ and $\log \xi = -1.2$ (erg cm s^{-1}) — derived by Kaastra et al. (2014). The ionization parameter ξ is defined as (Tarter, Tucker, & Salpeter 1969; Kallman & Bautista 2001)

$$\xi = \frac{L}{n(\text{H})R^2}, \quad (2.1)$$

where L is the luminosity of the ionizing source over the 1–1000 Ryd (13.6 eV to 13.6 keV) band in erg s^{-1} , R is the distance from the source in cm. For the hydrogen density, we adopt $n(\text{H}) = 10^{10} \text{ cm}^{-3}$, which is a typical BLR cloud density. We adopt the `Cloudy` default value² for solar abundances, which are generally within 30% of the Lodders (2003) meteoritic abundances used in some of the previous modeling. The transmitted

²More information about the default values can be find in HAZY: <https://www.nublado.org/wiki/DownloadLinks>

SED calculated with these parameters is shown in Figure 2.4, in which we assume that the obscurer fully covers the continuum source. This figure shows the net transmitted radiation field at the shielded face of the obscurer. It includes the attenuated incident radiation field produced by the central object along with line and continuum emission produced by the obscurer. The effects of filtering the continuum has been discussed in other literature but within different contexts (Ferland & Mushotzky 1982; Leighly, 2004). The horizontal lines in Figure 2.4 indicate the ionization energies for the species studied by Kriss et al. (2019). The left terminus of each line shows the energy needed to produce the ion, while the right terminus indicates the amount of energy required to destroy the ion by further ionization. The high ionization-potential species (indicated by dotted lines) did not correlate with the FUV during the holiday, while lower ionization potential species (solid lines) remained correlated.

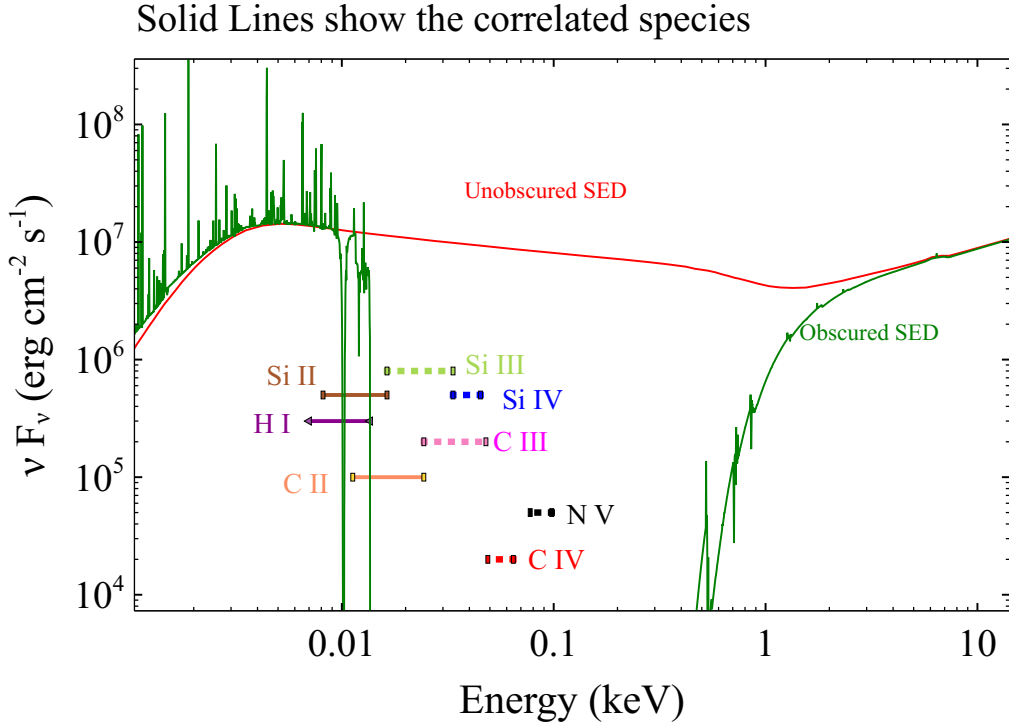


Figure 2.4: The expected SED transmitted through the obscurer and striking Component 1. Each line segment shows the energy required to produce the ion (left end) and to destroy the ion (right end). In this Figure, we assumed that the obscurer fully covers the continuum source. The column density to make the transmitted SED is $N(\text{H}) = 1.2 \times 10^{22} \text{ cm}^{-2}$

In the case of Component 1, we adopt the parameters from Arav et al. (2015), $\log n(\text{H}) = 4.72 \text{ (cm}^{-3}\text{)}$ and ionization parameter $\log U = -1.5$, which is defined to be (Osterbrock & Ferland 2006):

$$U = \frac{Q(\text{H})}{4\pi R^2 n(\text{H})c}, \quad (2.2)$$

where $Q(\text{H})$ is the number of hydrogen-ionizing photons emitted by the source per second, R is the cloud distance from the ionizing continuum source, which is 3-5 pc for Component 1. In the above equation c is the speed of light. Note that the papers modeling the obscurer (Kaastra et al. 2014) and Component 1 (Arav et al. 2015) use different definitions for the ionization parameter. For the unobscured SED, the relation $\log U = \log \xi - 1.6$ can be used to convert between these ionization parameters. For the obscured SED (Figure 2.4, green line), the conversion relation is $\log U = \log \xi - 3.3$.

2.4 What happened?

We hypothesize that two independent events occurred. First, the luminosity of the AGN varied, causing the entire SED to become brighter or fainter. This would cause the expected correlated variations. Second, the obscurer moved across our line of sight, perhaps due to its orbital motion around the black hole, changing the fraction of the central source that is covered. We will show below that absorption by the obscurer changes the EUV, XUV, and soft X-ray portions of the SED but has little effect on the optical, UV, or FUV, where the obscurer is transparent. This variable absorption, caused by the changing covering factor, would affect the high ionization absorption lines but have little effect on the FUV or optical continuum, so would produce decorrelated changes i.e., a "holiday". In the rest of this section, we investigate these two events in more detail.

2.4.1 Changing the luminosity of the source

The changing luminosity is directly seen via optical, FUV, and X-ray observations. In photoionization equilibrium, this implies a varying ionization parameter, which would change the column densities of all species. As a test, we checked what happens to the column densities of Component 1 absorbing species when the continuum luminosity changes, while keeping the unobscured shape of the SED the same. We use the Arav et al. (2015) standard Component 1 parameters as described above, but we let the ionization parameter U vary by one dex to either side of the standard value of $\log U = -1.5$. This would correspond to changes in the continuum luminosity by the same amount. For comparison, the 1157Å *HST* continuum varied over a range of 0.6 dex during the STORM campaign. Figure 2.5 shows the results of these calculations. The solid lines show the correlated species while the dashed lines are decorrelated. All the column densities change dramatically, however around the standard value of $\log U = -1.5$, the columns of the correlated species are changing very fast, and faster than those of the decorrelated ones. This is not enough to explain the holiday. Thus, simple changes in the luminosity of NGC 5548 cannot explain the absorption line holiday. We must look elsewhere.

2.4.2 Changing the obscurer covering factor

The soft X-ray extinction measures the fraction of the continuum source covered by the obscurer. We refer to this as the "line of sight covering factor" (LOS CF). Changes in the LOS CF affect the absorption lines seen with *HST* since the SED transmitted through the obscurer is responsible for the ionization of Component 1.

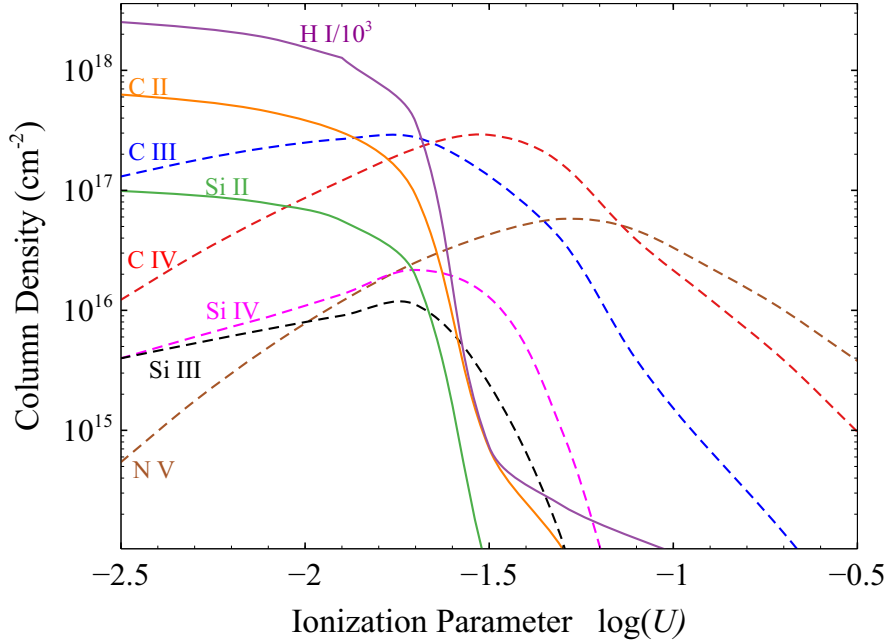


Figure 2.5: This shows how Component 1 column densities change as the ionization parameter changes. The hydrogen column density is divided by 1000 for comparison purposes. The solid lines are correlated species while the dashed lines are decorrelated. These changes are unlike those seen in the holiday, ruling out changes in U alone as the reason for the holiday.

Figure 2.6 shows how changes in the LOS CF affects SED_{inc} , the SED striking Component 1. This is defined as:

$$SED_{inc} = (LOS\ CF) \times (SED_{extinguished}) + (1 - LOS\ CF) \times SED \quad (2.3)$$

for various LOS CF. Here “SED” indicates the unattenuated SED shown in Figure 2.3. The intensity is adjusted to $\log U = -1.5$ with $LOS\ CF = 0$ (Arav et al. 2015). We keep the brightness of SED_{inc} constant at 4558 \AA (0.2 Ryd), and vary the LOS CF to obtain different shapes. We chose the energy 0.2 Rydberg since this is an energy where the obscurer is transparent. In Equation (3), $LOS\ CF = 0$ will be the full unattenuated SED and 100% coverage would be the Mehdipour et al. (2015) extinguished SED (Figure 2.4). Figure 2.6 shows that the 1 keV X-ray absorption is highly affected by changes in the LOS CF. The hard X-rays are not absorbed and so do not change. Note that this assumes that the LOS CF is the same for the EUV and XUV, whereas these components may form in different regions (Gardner & Done 2017; Edelson et al. 2018). Note that the SEDs shown in Figure 2.6 are the *incident* radiation field striking the illuminated face of Component 1. The data come

from the second column of the `cloudy save continuum`. The effects of diffuse fields from the obscurer are included when generating the extinguished SED.

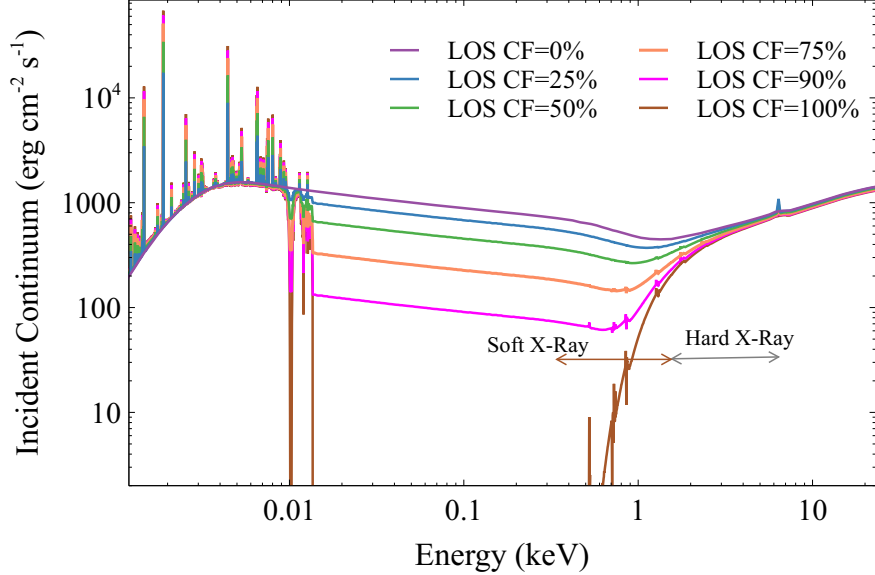


Figure 2.6: The variations of the SED striking Component 1 for different LOS CFs. The Arav et al. (2015) ionization parameter is reproduced at zero coverage. The Figure indicates the soft and hard X-ray energies, i.e., 0.3–1.5 keV and 1.5–10 keV (Mehdipour et al. 2016).

Variations of the obscurer LOS CF produce considerable changes in the transmitted SED without producing observable changes in the FUV since the obscurer is transparent in the FUV (see Figure 2.6). Perhaps this can provide an explanation for the correlated and decorrelated behavior of the narrow absorption lines of Component 1. Next, we investigate how the column densities of Component 1 are affected by the changes in the obscurer LOS CF. We used SEDs like those illustrated in Figure 2.6 to predict the column densities of the Component 1 species measured by Kriss et al. (2019). These are shown in Figure 2.7. The column densities of high ionization species decrease while low-ionization species change little at high LOS CF values. Clearly, then, changes in the obscurer LOS CF are capable of causing the absorption line holiday. The next section outlines the physics behind Figure 2.7.

2.5 Physics behind the “holiday”

Figure 2.7 focused on the absorption line species observed in the *HST* spectra. These are not necessarily the dominant or most important ions. Figure 2.8 shows how the physically important ions change, and includes helium, which *HST* did not observe. Silicon and carbon are mainly singly ionized, while He is mostly neutral.

As the LOS CF increases, the column densities of the higher ionization-potential decorrelated ions decrease dramatically, as also seen in Figure 2.7. The ions He^+ and He^{+2}

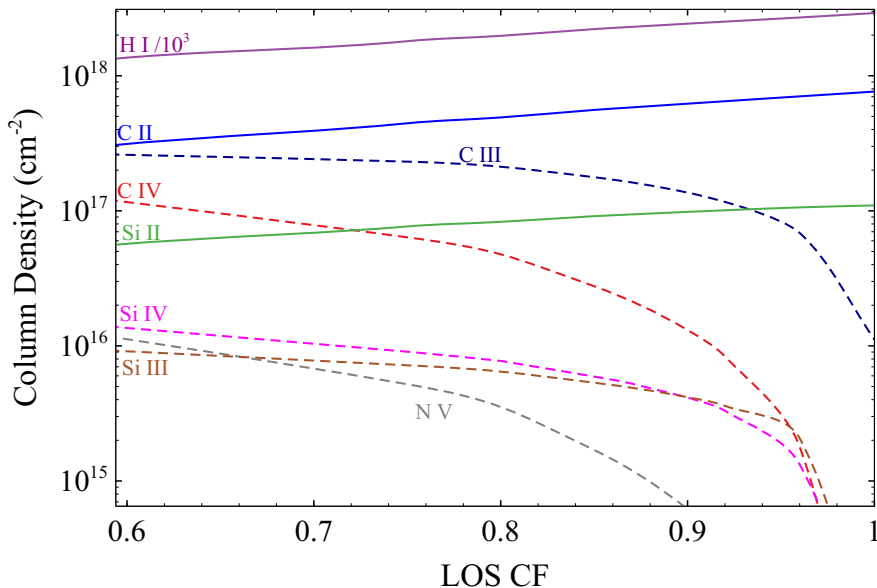


Figure 2.7: The effects of changes in the obscurer LOS CF upon the column densities observed by *HST*. Low-ionization species (solid lines) remained correlated while high ionization (dashed) species were decorrelated during the holiday, as expected from changes in the obscurer covering factor. The ionization parameters adopted for the obscurer and Component 1 are $\log \xi = -1.2$ (erg cm s^{-1}) and $\log U = -1.5$, respectively.

behave like the higher ionization-potential decorrelated species. Si^+ and C^+ are the most abundant ions, and their column densities change only slightly. To understand this behavior, we must isolate what photoionizes the dominant and correlated low-ionization species to produce the decorrelated behavior in the higher ionization species. To answer this, we consider the radiation field within Component 1. Figure 2.9 shows the diffuse radiation field at the midplane, the middle of the Component 1 cloud. The midplane is a representative location, and its properties give insight into the physics of the cloud. We chose a LOS CF of 96%, which is representative of the regions of Figure 2.7 where the correlated/decorrelated behavior is pronounced. This covering factor is so large that the EUV and XUV portion of the incident SED shown in Figure 2.6 is faint. The diffuse radiation field shown is produced by emission from the absorbing gas itself and is dominated by line and continuum emission produced by recombining helium. Several of the prominent emission features are labeled. The horizontal lines indicate the range of photon energy that can photoionize the indicated species.

Examination of the photoionization rates shows that C^+ and Si^+ are produced by photoionization of the neutral atoms by the Balmer continuum. They are destroyed by valence-shell photoionization, with thresholds of 24.4 eV and 16.3 eV for C^+ and Si^+ , respectively. Inner shell photoionization by the soft X-rays is much less important. The He I radiative recombination continua (RRC) (for C^+ and Si^+) and singlet and triplet $2p - 1s$ transitions of He^0 (for Si^+) are the primary sources of photoionization at energies of $\sim 20 - 25$ eV, the

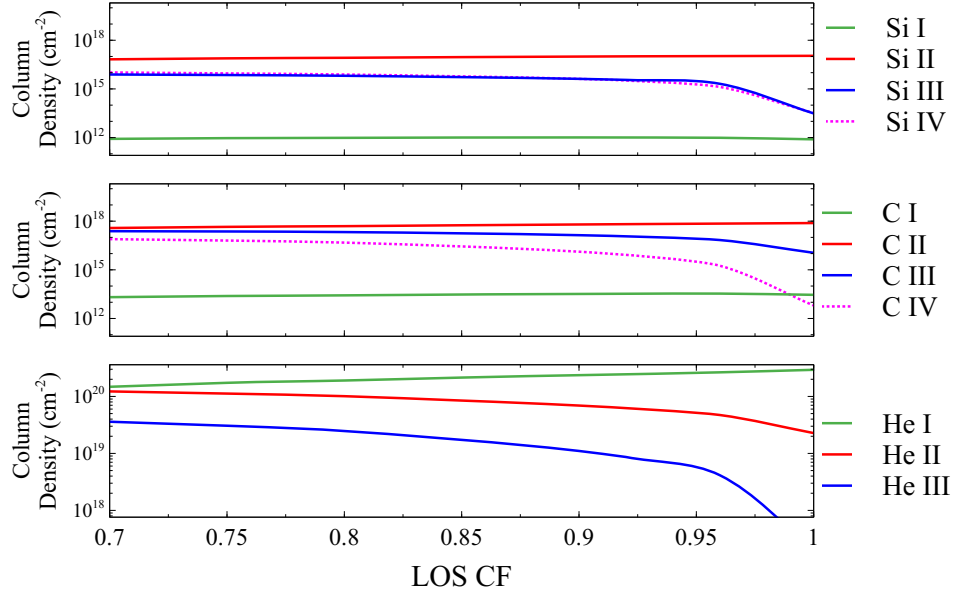


Figure 2.8: Variations of the column densities of different ionization stages as the obscurer LOS CF changes. Si, C, and He are shown in three panels, from top to bottom, respectively.

threshold for destroying these dominant species. These are all produced by recombination of He^+ . This means that the abundances of the decorrelated high-ionization species follow the abundance of He^+ and subsequent HeI emission. Figure 2.8 shows that the decrease in column density of the decorrelated species tracks changes in the He^+ column density. What is responsible for photoionization of He^0 , producing He^+ ? He^0 is the dominant ion stage in Component 1 (Figure 2.8). Examination of the contributors to the photoionization rates shows that He^+ is produced through photoionization by soft X-rays from the attenuated SED of the AGN. Figure 2.9 shows only the diffuse fields and does not include the attenuated incident SED. He^0 is an important opacity source for soft X-rays. Figure 2.10 shows the continuous opacity at the midplane of the Component 1 cloud. We evaluated the total gas opacity for the predicted distribution of ions and the assumed solar composition. This shows the opacity per hydrogen and is multiplied by the cube of the photon energy so that it can be compared with standard plots of the total ISM opacity (Ride & Walker 1977). The green line shows the total opacity while the other lines show some of the important contributors to it. H^0 is dominant in the low-energy EUV, He^0 is dominant in the high-energy EUV and XUV, and the heavy elements dominate around 0.5 – 1 keV (Crudace et al. 1974; Ride & Walker 1977, their figure 2), causing the stepped rise in the right part of the diagram. Helium is mainly neutral (Figure 2.8) and Figure 2.10 shows that helium is a major contributor to the total opacity for energies from 24 to 300 eV.

The gas photoionization rate is the integral of the opacity shown in Figure 2.10 over the radiation field shown in Figure 2.9 (see Osterbrock & Ferland 2006, equation 2.30). It is critical to know which part of the radiation field dominates the total photoionization rate, since this has the greatest effect on the ionization of Component 1. This is shown in

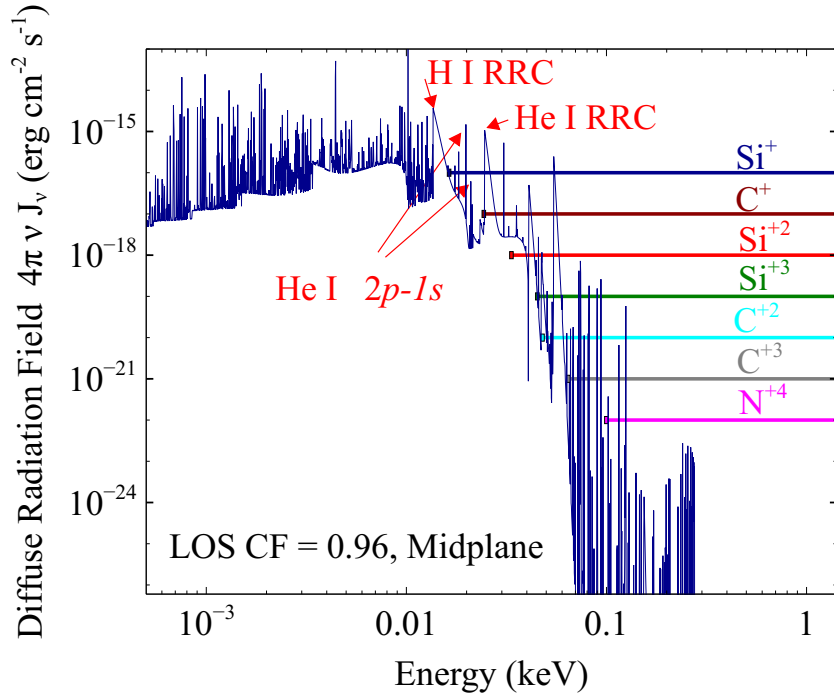


Figure 2.9: Diffuse emission field at the midplane of Component 1 with 96% obscuration. The left terminus of the horizontal lines shows the minimum energy needed to destroy the ion and produce the higher stage ion. RRC stands for radiative recombination continua and H I RRC is the Lyman continuum emission

the lower panel of Figure 2.11. This panel shows the values of the terms entering in the photoionization rate integral, namely the product $\nu^2 (4\pi J_\nu / h\nu) \times \alpha_\nu$. In this equation, α_ν is the opacity and J_ν is the mean intensity. This shows the coupling between the radiation and the gas. Only interactions at energies greater than 13.6 eV affect the ionization of the gas, and the strongest coupling occurs at energies between ~ 200 eV to ~ 2 keV. When the LOS CF varies, the soft X-rays change, as shown in Figure 2.6. This carries over into changes in the ionization of He⁰. This leads to changes in the He⁰ EUV recombination radiation, which produces the highly ionized species seen by *HST*.

The upper panel of Figure 2.11 shows the incident SED as a solid blue line. The solid red line shows the total radiation field, including both the diffuse and attenuated incident, at the midplane of Component 1. This is the net transmitted continuum which is the 5th column of the `save continuum` command in `cloudy`. Similar to Figure 2.6, the effects of diffuse field within the obscurer are included when making a table of the SED passing through the obscurer. We then used this table to generate the appropriate SED in midplane of the Component 1. The EUV and XUV portions of the SED are heavily extinguished so that most radiation at the midplane is due to diffuse gas emission (Figure 2.9 showed only the diffuse emission).

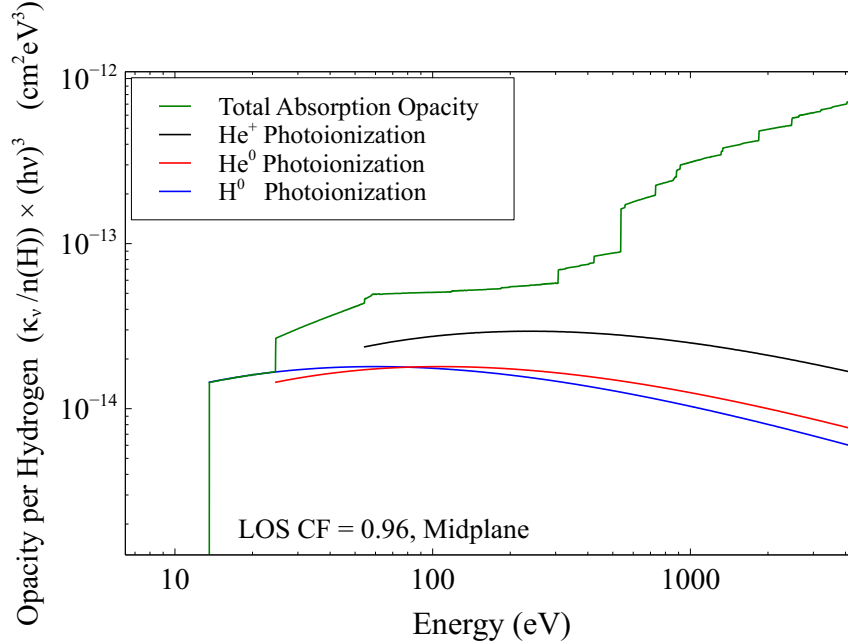


Figure 2.10: Opacity per hydrogen atom is shown as a function of energy. This shows the total opacity at the Component 1 midplane. The vertical axis has been scaled by $h\nu^3$ for clarity, as described in the text.

As it is obvious from Figure 1, Component 1 is between the Earth and the obscurer so the obscured Mehdipour et al. (2015) SED is what strikes Component 1. The original continuum used here (Figure 3 and Figure 4 red curve) is now available in Cloudy version 17. This observed continuum is quite a bit harder than the SED in figure 1 of Mathews & Ferland (1987). The latter was based on observations of very luminous Palomar/Green quasars. The SED adopted here is based on observations of NGC 5548 obtained in 2013 and 2014 by the Anatomy and STORM campaigns. It is worth mentioning that tests show that the choice of intrinsic SED has very little effect on our predictions, which mainly depend on the properties of the obscurer.

To summarize, we have investigated, in detail, how changes in the LOS CF affect the ionization of the higher-ionization species observed by *HST* and identified a unique physical cycle. The LOS CF changes the soft X-ray part of the SED but not the FUV continuum, so the resulting changes would not correlate with the FUV. The soft X-rays change the ionization of helium. The ionizing radiation emitted by recombining He^+ changes the ionization rate and abundance of the decorrelated species. However, anything that changes the soft X-rays without affecting the FUV could have a similar effect. This might include the Comptonization scenario outlined by Mathur et al. (2017), the Falling Corona Model studied by Sun et al. (2018) the partial dust obscuration model of Gaskell & Harrington (2018), or other models such as non-axisymmetric continuum (Dexter & Agol 2011) or anisotropic continuum models (Gaskell & Klimek 2003).

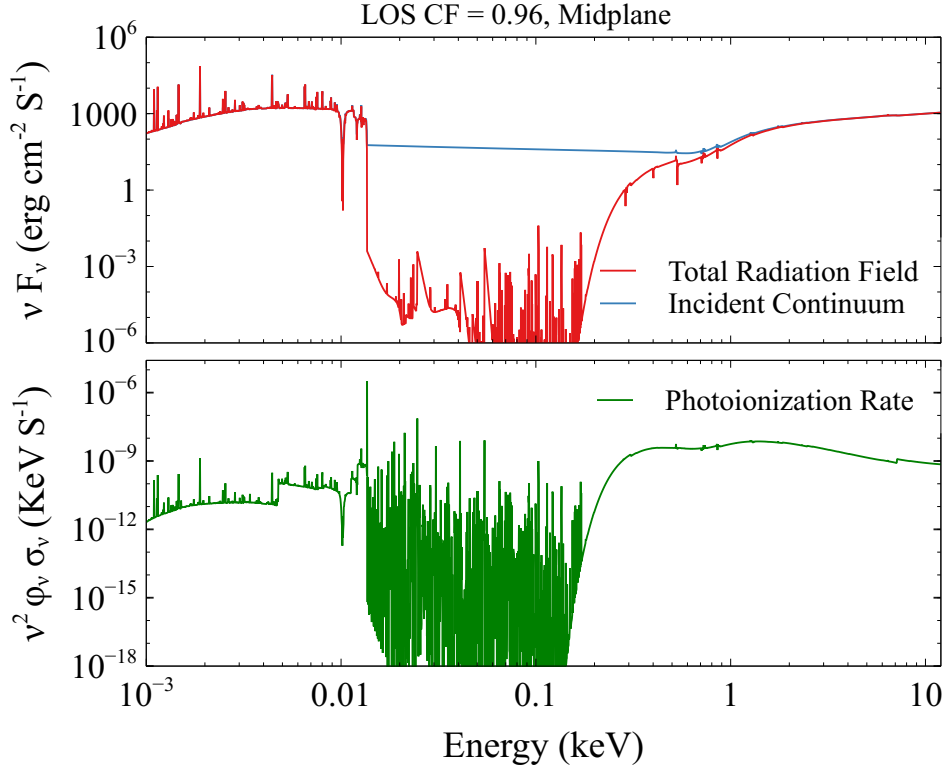


Figure 2.11: The upper panel shows the radiation field striking Component 1 as the blue line and the radiation field at the midplane of the cloud as the red line. The lower panel shows the photoionization rate at each energy.

2.6 Testing the covering factor model

In this paper, we did not try to model any particular observation but examined how changes in the obscurer can affect parts of the SED and result in the observed correlated/decorrelated behavior. We have identified a physical cycle which can reproduce the observed behavior. Here we outline two observational tests of this model.

2.6.1 Existing observations: X-ray hardness ratio and inferred LOS CF

Figure 2.12 summarizes *Swift* and *HST* observations described by Kriss et al. (2019). The red line is the *HST* continuum at 1367 Å, the blue line shows Ly α absorption line and NV absorption line in the upper and lower panels, respectively. These are examples of correlated and decorrelated lines. These are similar to the blue line in the panels of Figure 2.2. In our model, the changing obscurer covering factor is responsible for the absorption-line holiday. The X-ray hardness ratio measured by *Swift*, a measure of the hard to soft X-ray brightness, is also a measure of the LOS covering factor, as demonstrated by Mehdipour et al. (2016), equation 2. The obscurer LOS CF changes, derived by Mehdipour et al. (2016) using the broadband spectral modeling of the *Swift* data, are shown in Figure 2.12 as a

green line for comparison. The right CF axis is inverted, decreasing from bottom to top, to make it easier to compare with the other quantities plotted. The upper panel shows that Ly α absorption line is correlated with the *HST* continuum. The LOS CF is also shown in that panel but with a thinner line to not divert attention. The lower panel is drawn similarly, showing that NV absorption line has a better anti-correlation with the LOS CF rather than the correlation with the *HST* continuum.

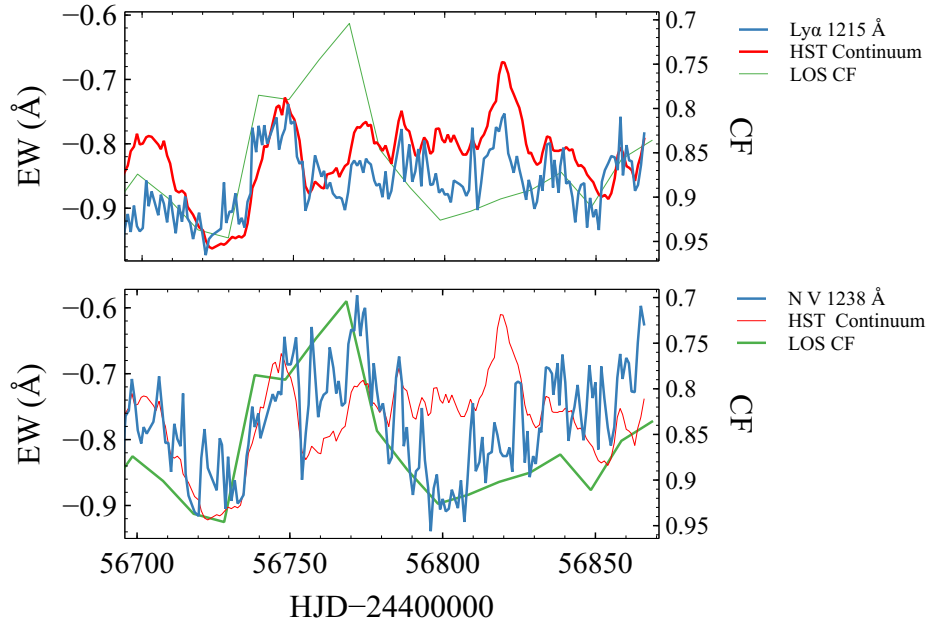


Figure 2.12: The EW of the Ly α absorption line in Component 1 is shown as the blue line in the upper panel and the EW of the corresponding NV absorption line is shown in the lower panel. The red line shows the *HST* FUV continuum while the green line is the LOS covering factor of the obscurer derived from the X-ray hardness ratio as defined by Mehdipour et al. (2016). Ly α absorption line is correlated with the *HST* continuum while NV absorption line anticorrelates with the covering factor.

Figure 2.12 shows that NV absorption responds to variations of the LOS CF better than the *HST* continuum. Figure 2.7 shows that larger covering factors and greater extinction cause NV absorption to weaken: NV absorption line is predicted to be anticorrelated with the covering factor. These trends are in the same sense as our predictions.

2.6.2 Future observations: the full range of obscurer covering factor

Figure 2.7 focuses on large values of the LOS CF because the covering factor was in this range during the holiday (Mehdipour et al. 2016). There were other times when the obscurer was not present. Although this was not observed, there must have been times when the obscurer was first coming into our line of sight, and the LOS CF was increasing from small values. Figure 2.13 illustrates the full range of the covering factor. The behaviors of the correlated and decorrelated species are reversed for values of LOS CF in the range

0.3-0.5: The correlated species show dramatic changes while the decorrelated ones remain almost constant. Very small values of the LOS CF represented times before 2011 when there was no obscurer. As Figure 2.13 shows, lower ionization potential species almost disappear. Observations that were performed before 2011 confirm the predictions of Figure 2.13 (Crenshaw et al. 2009). This motivates future observational tests. Continued monitoring of NGC 5548 by *Swift* could identify times when the LOS CF becomes small again. *HST* observations could then be obtained to follow changes in the absorption lines.

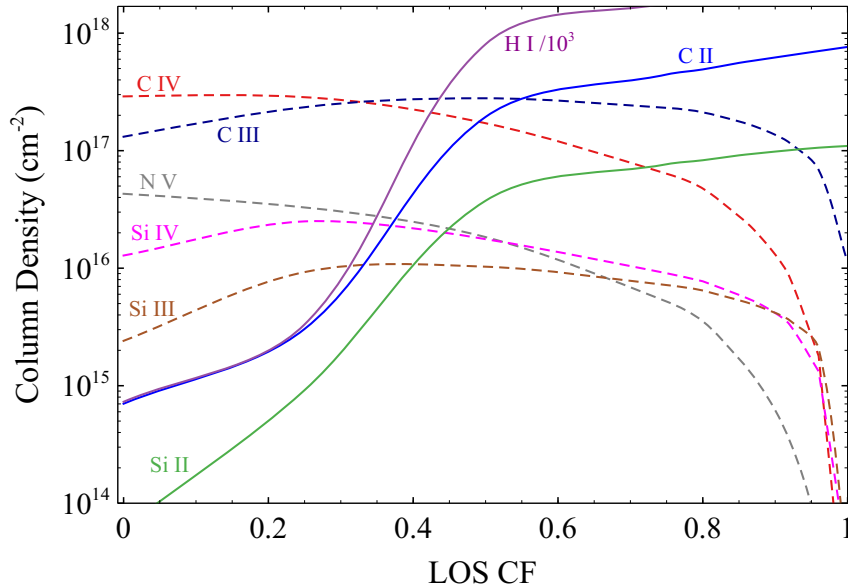


Figure 2.13: The effects of changes in the LOS CF on the ionic column densities over the full range of covering factor are shown. The dashed and solid lines indicate decorrelated and correlated species, respectively. Their behavior swaps around in the low and high covering factor limits, offering a test of the variable covering factor model. In this models, the ionization parameter for Component 1 is $\log U = -1.5$.

2.7 Discussion and summary

The reverberation mapping method relies on a causal connection between variations in the lines and continuum. This correlation broke down during the so-called “holiday” period as discovered by the AGN STORM project. The complications due to these abnormalities may have an effect on derived BLR radii and BH masses, which is why it is important to identify the physics which allows such holidays to occur. The fact that high-ionization absorption lines displayed the holiday while low-ionization absorption lines did not is an important clue to what is happening. It is worth emphasizing that “holiday” was first seen in the Broad emission-lines which have a more complicated geometry (Goad et al. 2016). We showed that changes in the luminosity of the AGN do not produce the observed behavior. This suggests that changes in the shape of the SED are responsible. Strong soft X-ray

absorption, produced by a transient cloud referred to as the obscurer, was present throughout the AGN STORM campaign. The obscurer covered only a fraction of the continuum source, which we refer to as the “line of sight covering factor,” LOS CF. The soft X-ray absorption was not present before 2011, showing that the LOS CF can change dramatically.

We investigated the effect of a changing SED on Component 1 cloud producing the strong absorption lines. We have shown that changes in the LOS CF reproduce the observed behavior for large values of the LOS CF. We identified a unique physical cycle in which changes in the LOS CF have a significant effect on soft X-ray portion of the SED. This changes the ionization stage of helium and the ionizing radiation produced as helium recombines drives the changes in the decorrelated absorption lines. Changes in the LOS CF do not affect the optical or UV continuum since the obscurer is transparent at these energies. We identified two tests of this model. The first is the *Swift* measurements of the X-ray hardness ratio. This can be converted into an obscurer covering factor. This LOS covering factor does seem to correlate with the high ionization “decorrelated” absorption lines. We show that the sense of the correlation/decorrelation reverses for smaller covering fractions in the range 0.3-0.5, which can be used to test this scenario in future observations. The tests would have to take place when the covering factor is very low. The photoionization models we produced used a variable covering factor to change the soft X-ray portion of the SED. However, other models in which the soft X-ray part of the SED changes independently of the optical / UV continuum could produce similar effects. The Comptonization model proposed by Mathur et al. (2017) and the Falling Corona Model of Sun et al. (2018) could also produce the required changes in the SED. This will be the subject of future work.

Chapter 3 THE EMISSION-LINE HOLIDAY

Here, we examine the physics by which a related emission-line holiday could occur. We take the obscurer to be a wind launched from the accretion disk, with variable mass-loss rate and hydrogen density. Figure 3.1 shows a cartoon with one possible geometry. We show that for low hydrogen densities the obscurer near the disk is almost transparent and so has no effect on the SED striking the BLR. However, for higher densities it can obscure much of the ionizing radiation, producing the emission-line holiday. In this case, the observed UV continuum is not a good proxy for the ionizing flux. Finally, for even higher gas densities, little ionizing radiation strikes the BLR. In this case, broad-line emission is strongly suppressed, resulting in something like a changing-look AGN. We suggest that an equatorial obscurer associated with a disk wind produces the BLR holiday, and may in more extreme circumstances contribute to causing a changing-look AGN.

3.1 A baseline BLR with changing luminosity

Figure 3.1 shows the geometry of the central regions, including the obscurer, based on Kaastra et al. (2014) figure 4. We note that the Kaastra et al. (2014) figure only highlights the portion of the disk wind that forms the obscurer along our LOS. The critical differences in our illustration in Figure 3.1 are (1) we show the disk wind as an axisymmetric structure, (2) we show the full wind, with streamlines tracing from the surface of the disk to the gas lying along our LOS, and (3) we locate the obscurer interior to the BLR. The LOS obscurer is the upper part of the wind, and we refer to the lower part as the “equatorial obscurer”.

Although some of the properties of the LOS obscurer are known (such as its column density and x-ray absorption), there is no way to determine the properties of the obscurer near the disk. The density at the base is likely to be higher than at higher altitudes and the column density through the base of the wind toward the BLR is higher than along the LOS, and therefore the wind is potentially opaque. Although our LOS samples only a specific sight line through the wind, we assume the structure along all other sight lines is comparable and therefore can affect the whole of the BLR. The obscurer has persisted over at least four years (Mehdipour et al. 2016). If it is located interior to the BLR at < 0.5 light days, where the orbital timescale is only 40 days, this longevity implies that the wind extends a full 360-degrees around the black hole. It thus forms an axisymmetric, cylindrical continuous flow around the BH and so always fully shields the BLR. For this reason, it is not likely that a changing CF of the equatorial obscurer could explain the broad emission-line holiday as well.

Here we develop a baseline model for the BLR to investigate how its emission lines are affected by the variations of the SED striking it. At this stage, we avoid including the equatorial obscurer in our modeling, so changes in the emission-line spectrum are caused by the variations of the luminosity of the source. For simplicity, we do not model a full LOC¹ similar to figure 2 of Korista & Goad (2000). Our baseline model is sufficient for

¹Locally optimally emitting clouds

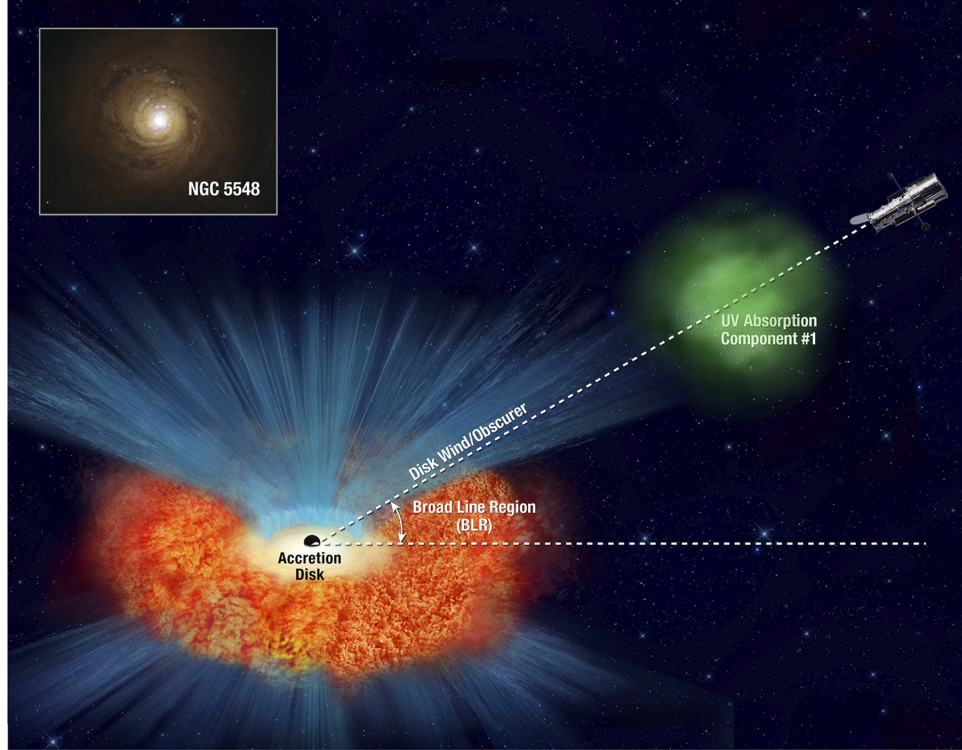


Figure 3.1: Diagram of the disk wind in NGC 5548 (not to scale). The BH is surrounded by the accretion disk. At larger radii the BLR is indicated by orange/red turbulent clouds. The disk wind rises nearly vertically from the surface of the accretion disk, where it has a dense, high-column-density base. At higher elevations, radiation pressure accelerates the wind and bends the streamlines down along the 30 degree inclination of the observer's LOS to the rotation axis of the disk (Kaastra et al. 2014).

the goal of this paper, which is to test how changes in the equatorial obscurer change the observed EW of the broad emission lines. We use the development version of Cloudy (C17), last described by Ferland et al. (2017), for all the photoionization models presented here.

To model the BLR, we fix its hydrogen column density to be $N(\text{H})=10^{23} \text{ cm}^{-2}$, choose a hydrogen density of $n(\text{H})=10^{11} \text{ cm}^{-3}$, and use solar abundances (Ferland et al. 2017). These are all typical values for the BLR (following Ferland et al. 1992; Goad & Koratkar 1998; Kaspi & Netzer 1999). The remaining parameter is the flux of hydrogen ionizing photons $\phi(\text{H})$ (ionizing photons $\text{cm}^{-2} \text{ s}^{-1}$) striking the cloud. For a given SED shape (we use that of Mehdipour et al. 2015, as discussed by D19) and location of the BLR, this flux depends on the luminosity, so changes in the flux simulate changes in the luminosity. We assume thermal line broadening evaluated for the gas kinetic temperature and atomic weight of each species.

The line EWs were observed to decrease as the luminosity increased before the holiday. Figure 3.2 shows our predicted EWs. The observations report a slope β that fits $\text{EW} \propto L^\beta$. G16 find β in the range -0.48 to -0.75 for Ly α , Si IV+O IV], CIV, and He II+O III], while Pei et al. (2017) find $\beta = -0.85$ for H β . This range of β values is shown as the bow tie

in the lower left corner. Each of these lines has its own reverberation timescale, formation radius, and value of $\phi(H)$. Future work will examine using EW and β to better constrain LOC models.

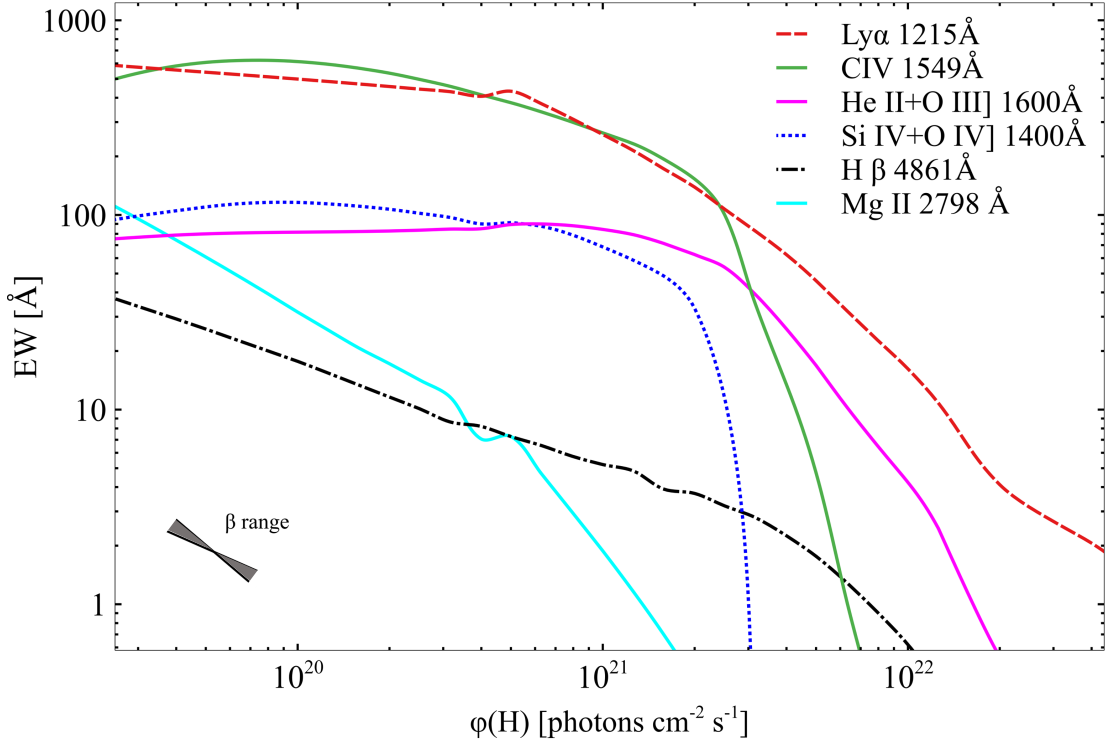


Figure 3.2: EW of emission lines vs. the flux of hydrogen ionizing photons. The EWs are normalized to the continuum at 1367\AA . For most of the lines, the predicted EWs decrease when $\phi(H) > 10^{20}$, the observed behavior. The bow tie shows the range of β observed for various lines before the holiday.

As Figure 3.2 shows, variations of the luminosity can dramatically affect the BLR. For $\phi(H) > 10^{20} \text{ cm}^{-2} \text{ s}^{-1}$ the CIV EW, shown in green, behaves as in G16’s figure 1b. Changes in the EW of CIV and $H\beta$ are consistent with G16 and Pei et al. (2017).

In the next Section, we consider the effects of the equatorial obscurer on the BLR. To do this, we only change the parameters of the obscurer, while we freeze all BLR parameters, including the unobscured flux, which we take to be $\phi(H) = 10^{20} \text{ cm}^{-2} \text{ s}^{-1}$. Our goal is only to demonstrate a scenario that produces emission-line holidays, so we are not trying to fine tune the parameters.

3.2 The SED transmitted through the equatorial obscurer

As Figure 3.1 shows, we assume that the obscurer is a wind extending from the equator to at least our LOS. This means that the BLR is ionized by the SED transmitted through the lowest part of the wind, the equatorial obscurer. Here we investigate how the SED transmitted through the equatorial obscurer changes as the wind parameters change.

There are no observational constraints on the equatorial obscurer, but it seems likely that it is denser, perhaps with a larger column density, than the more distant LOS obscurer. For simplicity, we hold its column density fixed at $N(\text{H}) = 10^{23} \text{ cm}^{-2}$ and assume solar abundances. Since the broad UV absorption associated with the LOS obscurer partially covers the BLR and has velocities ($\sim 1500 \text{ km s}^{-1}$) typical of the BLR (Kaastra et al. 2014), we assume that the LOS obscurer is near or coincident with the outer portion of the BLR. The equatorial obscurer must be closer to the black hole since it is launched from the disk. We choose $\phi(\text{H}) = 10^{20.3} \text{ cm}^{-2} \text{ s}^{-1}$, twice that of the BLR, placing the obscurer at $r_{\text{obscurer}} = 0.7 \times r_{\text{BLR}}$. We do not know the exact location of the equatorial obscurer and these values are chosen based only on the fact that it must be inside the BLR.

As in D19, we are trying to identify the phenomenology that makes the observed changes possible and not to model any particular observation (section 3.3 of that paper). We wish to see how the changes in the optical depth of the intervening wind affects emission from the BLR. These changes could be caused by variations in the physical thickness of the wind, its density, the AGN luminosity, or the distance from the black hole. For simplicity we vary only one of these, the density, while keeping the others fixed. As discussed in following sections, this change, while simple, does serve to illustrate the types of SEDs that will filter through the wind.

Changes in the mass-loss rate of the wind can cause changes in the hydrogen density of the equatorial obscurer. We examine the effects of such variations upon the transmitted SED in Figure 3.3, which shows three typical SEDs. As the Figure shows, the shape of the SED is highly sensitive to the value of the hydrogen density.

The density and flux parameters chosen here do not matter in detail. The transmitted SED actually depends on the ionization parameter, which is the ratio of the ionizing flux to the hydrogen density (Osterbrock & Ferland 2006). Increasing the hydrogen density lowers the ionization parameter inversely. Particular values of the density and flux do not matter as long as the ratio giving the ionization parameter is kept constant.

As the ionization parameter increases the level of ionization of the gas increases. The gas opacity decreases as the number of bound electrons decreases. The ionization structure changes in ways that produce the three characteristic SEDs shown in Figure 3.3. These are the three cases:

- Case 1 has the lowest density and the highest ionization, and is shown in black. This wind is fully ionized, has no H or He ionization fronts, and nearly fully transmits the entire incident SED.
- Case 2 has an intermediate density and is shown in blue. This has a $\text{He}^{2+} - \text{He}^+$ ionization-front but no H ionization-front. The incident SED is heavily absorbed for the XUV energies², although most of the hydrogen-ionizing radiation is transmitted.
- Finally, Case 3 is shown with the red line and has the highest density. The wind has both H and He ionization-fronts, and much of the light in the EUV and XUV regions is absorbed.

²We refer to the region 6 – 13.6 eV (912 Å to 2000 Å) as FUV; 13.6 – 54.4 eV (228 Å to 912 Å) as EUV; and 54.4 eV to few hundred eV (less than 228 Å) as XUV.

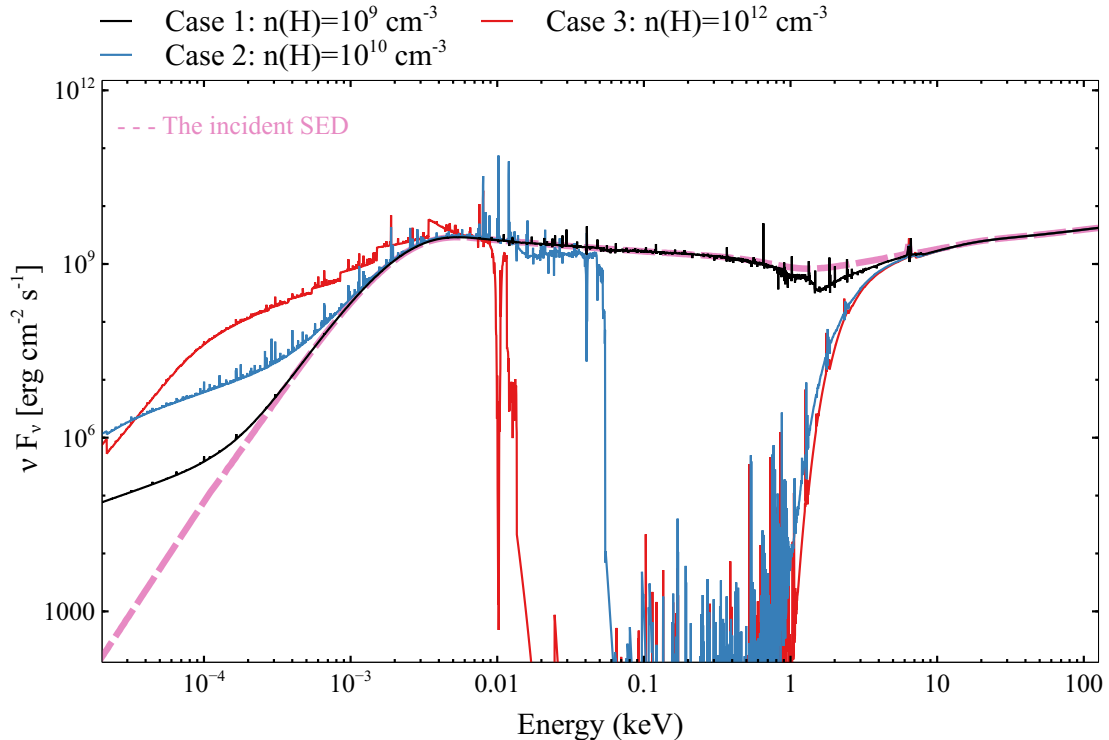


Figure 3.3: The SED transmitted through equatorial obscurer and incident upon the BLR is shown for three different values of the hydrogen density. The unextinguished SED is also shown. The SED is dramatically dependent on the hydrogen density of the obscurer. High hydrogen densities produce strong absorption in XUV region and strong emission in FUV/optical regions.

3.3 The response of the BLR to changes of the transmitted continuum

We now show how the EWs of the BLR lines in Figure 3.2 are affected by changes in the transmitted SED of the equatorial obscurer. Figure 3.4 shows how the EW of the strongest observed lines react as the density, $n(\text{H})$, of the equatorial obscurer varies. These changes are due to variations in the SED filtering through the equatorial obscurer. The three general types of SED shown in Figure 3.2 produce the three different BLR regimes shown in Figure 3.4. We examine each of these three cases in more detail:

- Case 1: In this low density regime (approximately $n(\text{H}) < 6 \times 10^9 \text{ cm}^{-3}$), the equatorial obscurer is transparent and has little effect on the SED or BLR. This may be the usual geometry in most AGN and results in a standard response of lines to the changes in the continuum luminosity. For low densities, the intervening wind has little effect on the optical/UV BLR, however, it does emit in other spectral ranges. This emission will be the subject of our future work. Changes in the EWs of the BLR emission lines follow the variations of the continuum luminosity.
- Case 2: In this case the obscurer has a higher density ($6 \times 10^9 \text{ cm}^{-3}$ to $4 \times 10^{10} \text{ cm}^{-3}$). As Figure 3.4 shows, for this range of hydrogen density, the BLR EW decreases

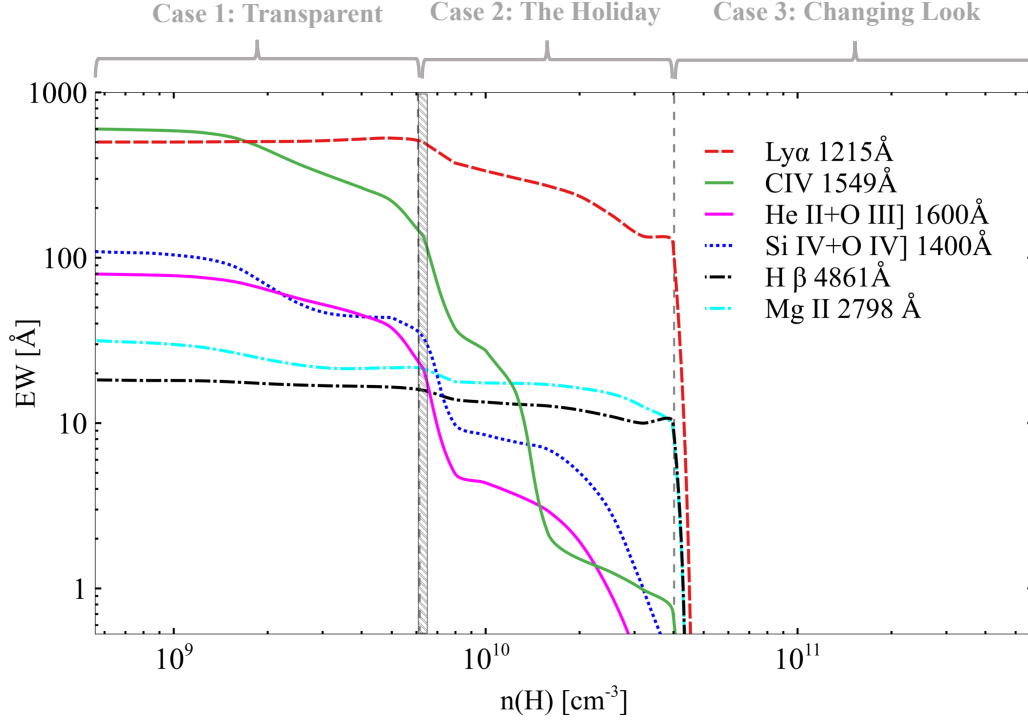


Figure 3.4: EW of all observed emission lines and Mg II versus the density of the equatorial obscurer. The plot is divided into three different cases, labeled at the top, based on the behavior of the EWs. The cases are described in the text. The shaded area shows the range in which the holiday observed in NGC 5548 will be produced.

independently of the AGN luminosity and the holiday occurs. Large changes in EW at $n(\text{H}) = 6 \times 10^9 \text{ cm}^{-3}$ are due to the He^{2+} - He^+ ionization front reaching the outer edge of the wind. Much of the SED in the XUV region is absorbed.

Case 2 produces the emission-line holiday. In this scenario, the obscurer's density increased only slightly above Case 1. When the ionization front appears, there are significant changes in the transmitted SED and the BLR follows these changes. These changes are independent of the observed far-ultraviolet continuum longward of 912 Å, so appear as a holiday.

One check of this model of the holiday is the $\sim 19\%$ deficit in CIV EW observed by G16. A smaller deficit, $\sim 6\%$, was observed by Pei et al. (2017) for $\text{H}\beta$. Figure 3.4 shows that only small changes in the density ($\sim 8\%$) are needed to produce this CIV deficit. The change needed to produce the holiday is shown by the gray shaded area. Our model predicts the largest deficits for Si IV+O IV], He II+O III], and CIV EWs, with a smaller deficit for $\text{Ly}\alpha$ EW, and the smallest deficit for $\text{H}\beta$ EW. These predictions are in the same sense as the AGN STORM observations (G16 & Pei et al. 2017).

Mg II was not observed by the STORM campaign, however we report this line for future reference. The line is nearly constant when the obscurer is in Case 1 while

in Case 2 it is slightly affected. This is reasonable, since we do not expect such a low-ionization line to be affected as much as CIV or other similar lines.

- Case 3: In this case, the obscurer has the highest density ($> 4 \times 10^{10} \text{ cm}^{-3}$) and most of the ionizing radiation is blocked. As Figure 3.4 shows, many of the broad emission lines vanish. A dense equatorial obscurer provides a scenario to produce a “changing-look” quasar, transitioning from Seyfert 1 to Seyfert 2. Figure 3.5 compares the optical/UV BLR spectrum for Cases 1 and 3. The upper panel shows that UV broad lines are suppressed by the dense equatorial obscurer. The optical lines in the lower panel almost disappear. This Figure suggests that dense disk winds could contribute to the changing-look AGN phenomenon, since changes in the equatorial obscurer can cause transitions between Seyfert 1 and 2 without affecting the optical / UV continuum. The LOS obscurer, if present, is transparent at those wavelengths. This would remove BLR emission during times when the black hole remained active, a different form of the changing-look phenomenon.

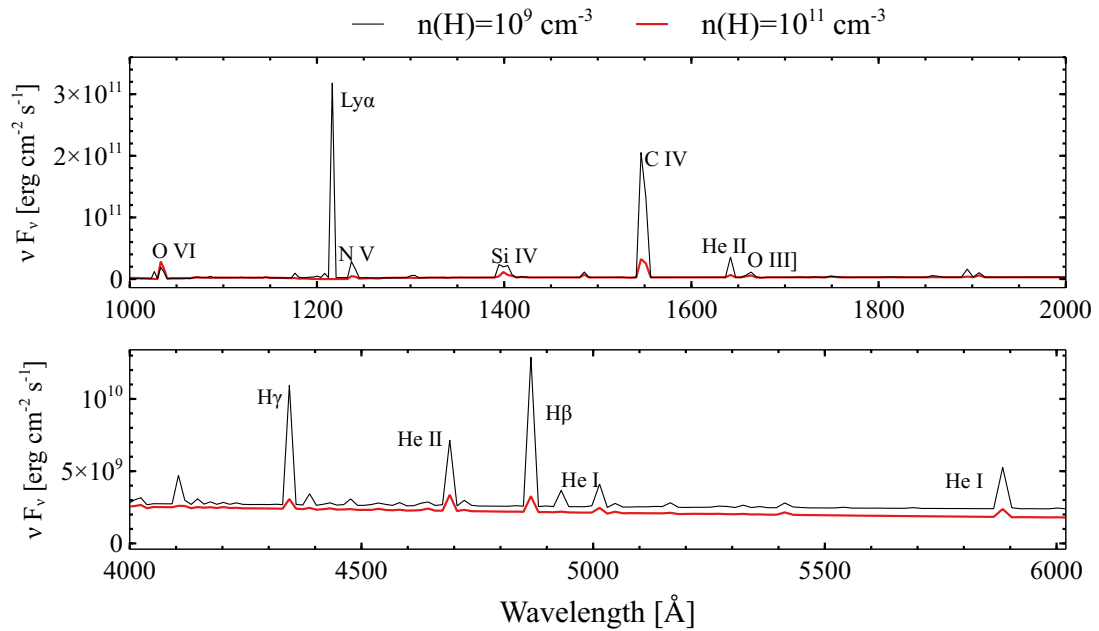


Figure 3.5: The total spectrum, including transmitted and reflected emission from the BLR for two densities of the equatorial obscurer. The upper panel shows the the UV regions and the lower panel shows the optical wavelengths. This Figure shows how phenomena similar to changing-look AGN, in which a Seyfert I turns into a Seyfert II, would occur without changes in the intrinsic luminosity of the AGN

3.4 Discussion and summary

Various types of winds are commonly seen in AGN. They launch from inner regions of the disk, so the geometry shown in Figure 3.1 might be typical, but usually in the transparent state (Case 1). A nearly fully ionized wind does not have a dramatic effect on the SED or lines.

The observed holiday corresponds to a temporary change in the density of the wind. We suggest that wind shielding is usually happening, but for most of the time we just do not notice it, because the wind is transparent. Such shadowing can be the missing ingredient in many AGN models.

Our model requires that the normal state of the equatorial obscurer is one where the ionization front is near the outer radius of the wind. The ionization-front location depends on the wind's parameters. This variation greatly affects the transmitted SED, as the wind density changes. The original Kaastra et al. (2014) model of the LOS obscurer ($\log U \approx -2.8$ or $\log \xi = -1.2 \text{ erg cm s}^{-1}$) has an H ionization-front and strong absorption at the Lyman limit (Arav et al. 2015). Later Cappi et al. (2016) proposed $\log U \approx -1$ ($\log \xi = 0.5 - 0.8 \text{ erg cm s}^{-1}$) for the LOS obscurer, and our tests show that this obscurer transmits the Lyman continuum, corresponding to the blue line, Case 2, in Figure 3.3. This shows it is likely that the physical state of the equatorial obscurer is such that the H, He ionization fronts are near the outer edge of the wind so that small changes in the model affect its location. This is why small changes in the obscurer's density (Figure 3.4) can produce significant changes in the SED and result in the holiday.

This model appears fine-tuned since it is sensitive to the location of the ionization front. But this geometry has a physical motivation from dynamical stability arguments. Mathews & Blumenthal (1977) point out that radiatively driven clouds become Rayleigh-Taylor unstable near ionization fronts so that the cloud tends to truncate at that point. This happens because the Lyman continuum radiative acceleration depends on the ion density, so falls precipitously when the gas recombines. This instability provides a natural explanation for why the obscurer tends to have an ionization front near its outer edge.

Although this paper discusses the emission-line holiday, a simultaneous holiday happened for higher-ionization narrow absorption lines (Kriss et al. 2019, D19). D19 show that changes in the CF of the LOS obscurer could be responsible for the absorption-line holiday. This obscurer is part of the same wind that produces the equatorial obscurer. The density of the equatorial obscurer, the base of the wind, might change because of instabilities in the flow. This produces the emission-line holiday, as shown in Figure 3.4. At the same time, it seems likely that injecting more mass from the base of the wind into our LOS causes the wind to produce a substantial flow and larger wind. This produces a larger CF for the LOS obscurer, producing the absorption-line holiday. So, a denser equatorial obscurer results in a more extensive LOS obscurer. In other words, the emission and absorption-line holidays are unified by the structure of the wind. This is the first physical model of the holidays observed in NGC 5548, and the relationship between them.

As Figures 3.3 shows, the SED transmitted through Case 2 is stronger than Case 1 for energies $\lesssim 1 \text{ eV}$. In Case 3, the SED is stronger than Case 1 for energies $\lesssim 5 \text{ eV}$. The emission is mainly due to hydrogen radiative recombination in the optical and NIR and Bremsstrahlung in the IR. These show that a dense equatorial obscurer can be a source of

continuum, even in Case 2. Such emission could explain the significant thermal diffuse continuum component spanning the entire UV–optical–near IR continuum” discussed in Goad et al. (2019) and may be the source of the non-disk optical continuum emission discussed by Ferland et al. (1990), Shields et al. (1995), and Chelouche et al. (2019). The BLR itself is also a source of non-disk continuum emission (Korista & Goad 2001).

To summarize, we have demonstrated, for the first time, a physical model by which several different phenomena are unified by the presence of the disk wind: an absorption-line holiday, an emission-line holiday, non-disk emission from the inner regions, and a contributor to the changing-look phenomenon. This shows the importance of “wind shielding”, in which a wind partially blocks the continuum ionizing other clouds. Large CF required by previous models (e.g Korista & Goad (2000); Kaspi & Netzer (1999); Goad et al. (1993)) supports the idea the “wind shielding” is likely. It may be the missing ingredient in understanding many AGN phenomena.

We came to a model in which an intervening obscurer filters the continuum striking emission and absorption line cloud after consideration of how they respond to changes during the STORM campaign. Many papers have considered cloud shadowing as an appropriate explanation for very different observations. Murray et al. (1995)’s study of accretion disk winds from AGN found that a dense gas could block the soft X-ray and transmit UV photons. Shielding permits wind acceleration to high velocities. This wind produces smooth line profiles and has a covering fraction of 10%. Leighly. (2004), suggested a wind model in which the continuum filtered through the wind would better fit her models of BLR emission. Finally, Shemmer & Lieber (2015) reproduced the Baldwin effect by use of such filtering. As the STORM campaign demonstrated, and these previous investigation suggested, cloud shadowing is a key ingredient in the physics of inner regions of AGN and must be considered in future studies.

Chapter 4 A NOVEL APPROACH TO IDENTIFY THE DISK WIND

In this chapter we consider new models of the equatorial obscurer. We do not provide new models of the BLR but rather rely on the results of chapter 3. Figure 4 of D19b shows that the equatorial obscurer will lead to a holiday if hydrogen is fully ionized and a He^+ ionization front is present within it (their Case 2). All models in this paper have a column density adjusted so that the optical depth is 8 at 4 Rydberg. This optical depth belongs to the left threshold of Case 2 in D19b, and ensures the presence of the emission-line holiday.

4.1 Cloudy modeling

We adopt the SED of Mehdipour et al. (2015) in `Cloudy` (developer version, Ferland et al. 2017) and an open geometry¹ for the equatorial obscurer. An open geometry is appropriate when the emission-line cloud CF is small since diffuse emission is assumed to escape from the AGN. The global BLR covering factor is about 50% (integrated cloud covering fraction, Korista & Goad 2000) and the equatorial obscurer must cover at least this much. So, it is intermediate between an open and closed geometry. Inspired by figure 1 of D19b, we adopt an open geometry. In order to make our predictions more accurate, we increased the number of levels to $n = 100$ for H like atoms. This allows a better representation of the collision physics that occurs within higher levels of the atom. We also set the spectral resolution to 5000 km s^{-1} . Changing the velocity width does not resolve the lines but changes the line-to-continuum contrast ratio to simulate a spectrometer measuring an unresolved line. We further assume photospheric solar abundances (Ferland et al. 2017).

With the assumptions above, we computed two-dimensional grids of photoionization models, similar to those of Korista et al. (1997). Each grid consists of a range of total hydrogen density, $10^{10} \text{ cm}^{-3} < n(\text{H}) < 10^{18} \text{ cm}^{-3}$, and a range of incident ionizing photon flux, $10^{20} \text{ s}^{-1} \text{ cm}^{-2} < \phi(\text{H}) < 10^{24} \text{ s}^{-1} \text{ cm}^{-2}$. The right vertical axis on all plots (Figures 4.1 to 4.3) shows the distance from the incident ionizing continuum source in light days. The flux of ionizing photons $\phi(\text{H})$, the total ionizing photon luminosity $Q(\text{H})$, and the distance in light days are related by:

$$\phi(\text{H}) = \frac{Q(\text{H})}{4\pi r^2}. \quad (4.1)$$

For the SED of Mehdipour et al. (2015) and the observed luminosity of L (1-1000Ryd)= $2 \times 10^{44} \text{ ergs}^{-1}$, the $Q(\text{H}) = 1.81 \times 10^{54} \text{ s}^{-1}$.

The STORM campaign reports observed lags between 2 and 9 light days for various strong emission lines (DeRosa et al. 2015, table 4). In Figure 4.1, we show contours of the predicted obscurer's column density. As mentioned earlier, we maintain a constant optical depth of 8 at an energy of 4 Rydbergs, the lower limit to have a holiday (D19b, figure 4).

Next, we combine these predictions with the observations to derive the properties of the equatorial obscurer.

¹Refer to section 2.3.4 of the `Cloudy`'s documentation, (Ferland et al. 2017)

Before going on, we establish a nomenclature for the different components that we discuss in this paper. For the case of UV lines, Goad et al. (2016) and many other previous work report the total “time-averaged broad emission line (BEL) EWs”. We refer to this as the “total” emission. Subsequent work by Kriss et al. (2019) model this total emission as the combination of three components: a “broad” component, a “medium broad” component, and a “very broad” component. The sum of the two first components (broad and medium broad) dominates in the line core, and we refer to them as the BLR/core. For CIV line, these components have FWHMs of 3366 ± 15 and 8345 ± 20 km/s, with an average of ~ 5000 km/s. Our calculations in Section 3 suggest that the very broad component (FWHM= 16367 ± 18 km/s, Kriss et al. 2019) forms in the equatorial obscurer. For reference, table 1 of Kriss et al. (2019) report that the very broad component of CIV comprises almost 47% of the total emission.

For Fe $K\alpha$, Cappi et al. (2016) report the presence of a time-steady “narrow” component with an upper-limit of 2340 km/s on the line width, or to be specific, $\text{FWHM} \leq 5500$ km/s. This is very similar to the BLR component of CIV (broad plus medium broad, Kriss et al. 2019). Assuming the line is broadened by orbital motions, and adopting the BH mass quoted by Cappi et al. (2016), they argue that this component forms a few light days away from the central source (0.006 pc), consistent with the lag observed for CIV. We refer to this component as the “BLR” Fe $K\alpha$ emission. The S/N ratios of the X-ray spectra do not permit a definitive detection of the very broad component modeled in the HST data, although Cappi et al. (2016) note that there appears to be a broad, redshifted component underlying the Fe $K\alpha$ profile.

4.2 Wind properties from the observations

The equatorial obscurer has a higher column density than the LOS obscurer since it is closer to the accretion disk, the site where the wind is launched. The orange line in Figure 4.1 shows the column density of the LOS obscurer, $N(\text{H}) = 1.2 \times 10^{22} \text{cm}^{-2}$ (Kaastra et al. 2014). The orange arrow shows the direction of possible higher column density obscurers.

The horizontal dashed black line indicates the location of the BLR adopting the CIV lag reported by DeRosa et al. (2015). To ensure that the base of the wind is located between the central SMBH and the BLR, we must choose an obscurer with a smaller distance (higher flux of ionizing photons) from the continuum source, than that for the BLR, the region suggested by the black arrow.

As Figure 4.1 shows, lines with constant column density are almost parallel for $N(\text{H}) > 10^{21} \text{cm}^{-2}$, and their values increase toward the upper left corner, closer to the source. These lines also represent a nearly constant ionization parameter, which increases toward the upper left corner.

The properties of the equatorial obscurer are constrained by observations. The equatorial obscurer is a source of emission itself since energy is conserved, and it must re-radiate the energy that is absorbed. If the equatorial obscurer emission is strong enough, then it produces a second emission-line region between the original BLR and the source. Since re-emission by the obscurer is not evident in the observations, we must find a model of the obscurer which not only explains the holiday, but also does not dominate the strong lines seen by HST and XMM-Newton. To do this, we considered the total observed equivalent

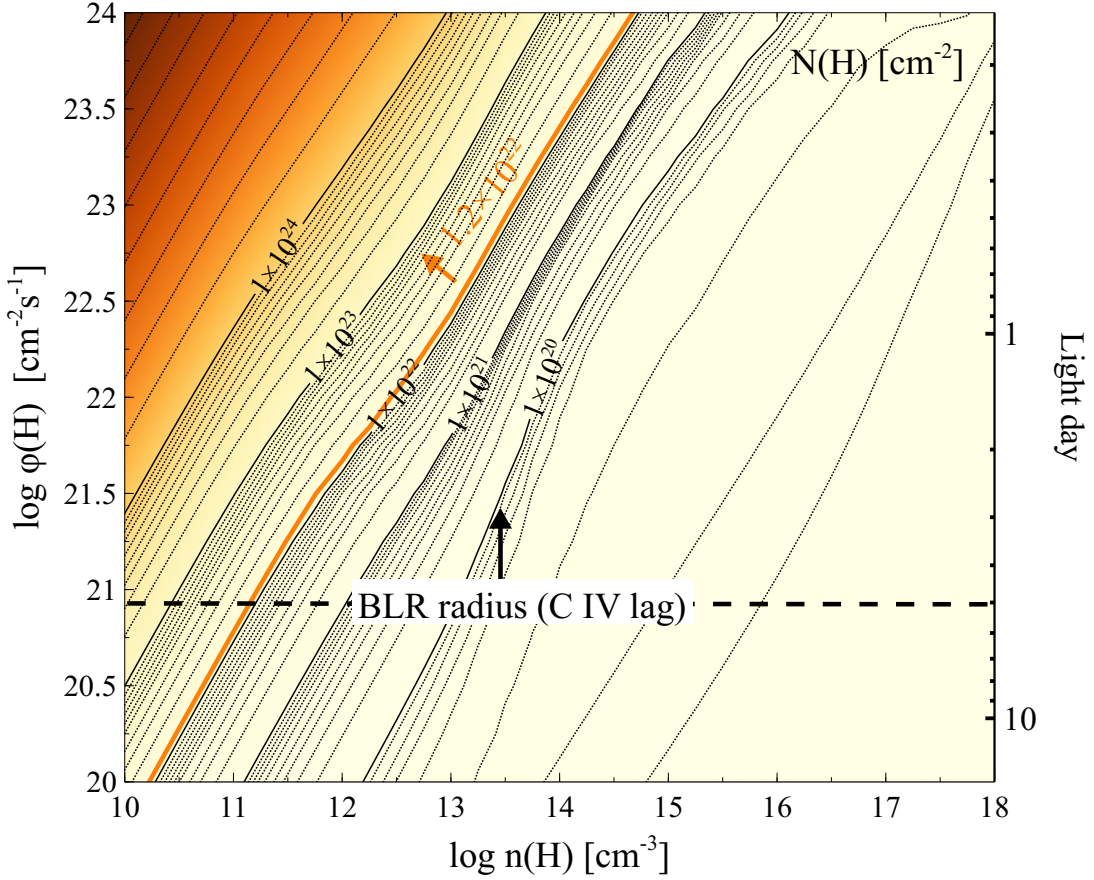


Figure 4.1: The contours show total hydrogen column density of the equatorial obscurer as a function of the flux of ionizing photons and the hydrogen density. The orange line indicates the LOS obscurer’s column density (D19a) and the dashed black line shows the location of the BLR based on the observed CIV lag.

widths (EWs) of strong emission lines from the STORM data (Goad et al. 2016; Pei et al. 2017) and the total luminosity of Fe $K\alpha$ observed by XMM-Newton (Mehdipour et al. 2015).

In general, an obscuring cloud may cover only a small fraction of the continuum source, as in the leaky LOS obscurer shown in figure 6 of D19a, or it can fully cover the continuum source (CF=100% in their figure). Here we assume that the equatorial obscurer fully covers the central object along the LOS of the BLR, which is the preferred situation explained by D19b.

We wish to directly compare our predictions with the observations. We report all lines as EW relative to the continuum at 1215Å so that ratios of EWs are the same as ratios of intensities.

The EW is proportional to the ratio of a line luminosity to the continuum. We assume that the continuum is isotropic and that HST had an unextinguished view of it. The contin-

uum luminosity is not affected by the equatorial obscurer’s CF. The luminosities of lines emitted by the equatorial obscurer are linearly proportional to the equatorial global CF, the fraction of 4π steradian covered by the obscurer. The equatorial obscurer covering factor is not known but must be at least 50% if it is to shield the BLR. We report EWs for full coverage with the understanding that the actual EW of the obscurer is:

$$\text{EW}(\text{obscurer}) = \frac{\Omega}{4\pi} \times \text{EW}(\text{pred}) \sim 50\% \text{EW}(\text{pred}). \quad (4.2)$$

On the other hand, the equatorial obscurer is not a dominant contributor to the emission lines. As a first step in the modeling, we set a limit to the amount of emission from the obscurer is less than half of the total emission. To choose this value, we were motivated by the ratio of the flux of very broad CIV to the flux of total observed CIV, 47%, as measured by Kriss et al. (2019):

$$\text{EW}(\text{obscurer}) \leq 50\% \text{EW}(\text{observed}). \quad (4.3)$$

Based on equations 4.2 and 4.3, the two factors of 50% cancel:

$$\text{EW}(\text{pred}) \leq \text{EW}(\text{observed}), \quad (4.4)$$

which means any model of the equatorial obscurer that produces lines with EW less than the observed total values are allowed. We map the obscurer’s predicted emission lines in Figure 4.2. We also include the observed values as colored lines in each panel. The arrows show the physical conditions where the obscurer will *not* dominate the emission line fluxes of observed HST spectrum.

The lowest panel of Figure 4.2 shows the predicted luminosity of Fe $K\alpha$ for full coverage. When the obscurer is highly ionized, Fe $K\alpha$ is strong (dark orange). It becomes weaker in the extreme upper left corner where the obscurer is fully ionized. In this regime, there are few bound electrons and there is no iron emission line or edge. The observed time-averaged value of its luminosity for the 2013 campaign is $(2.0 \pm 0.3) \times 10^{41}$ erg/s (Mehdipour et al. 2015) and is indicated by the blue lines in Figure 4.2.

Satisfying the constraints from Equations 4.2 and 4.3 guarantees that the obscurer does not produce strong emission lines. For the rest of the modeling, we assume this holds for all lines except HeII and broad Fe $K\alpha$. As discussed below, the lag profiles measured by Horne et al. (2020) show that HeII forms very close to the central source. We assume that all of the UV HeII comes from the obscurer. The Fe $K\alpha$ profile discussed below is consistent with half of the line forming in the BLR with a broad base forming in the obscurer.

Figure 4.3 shows the regions which satisfy all the constraints inferred from Figures 4.1&4.2. All the forbidden areas are colored in gray. The right panel shows the variation of the temperature as a function of both the flux and the density. The temperature increases as the distance to the central source decreases. The left panel maps the Thomson scattering optical depth as a function of flux and density. Gas in the upper left corner of the plot has a significant column density and Thomson scattering optical depth. Note that the soft X-ray observations constrain the ionization parameter but not the density or distance from the center so any location along the line is allowed. In both panels, all the constraints from Figure 4.2 are shown as faint colored lines, in order to show how we recognize the forbidden region.

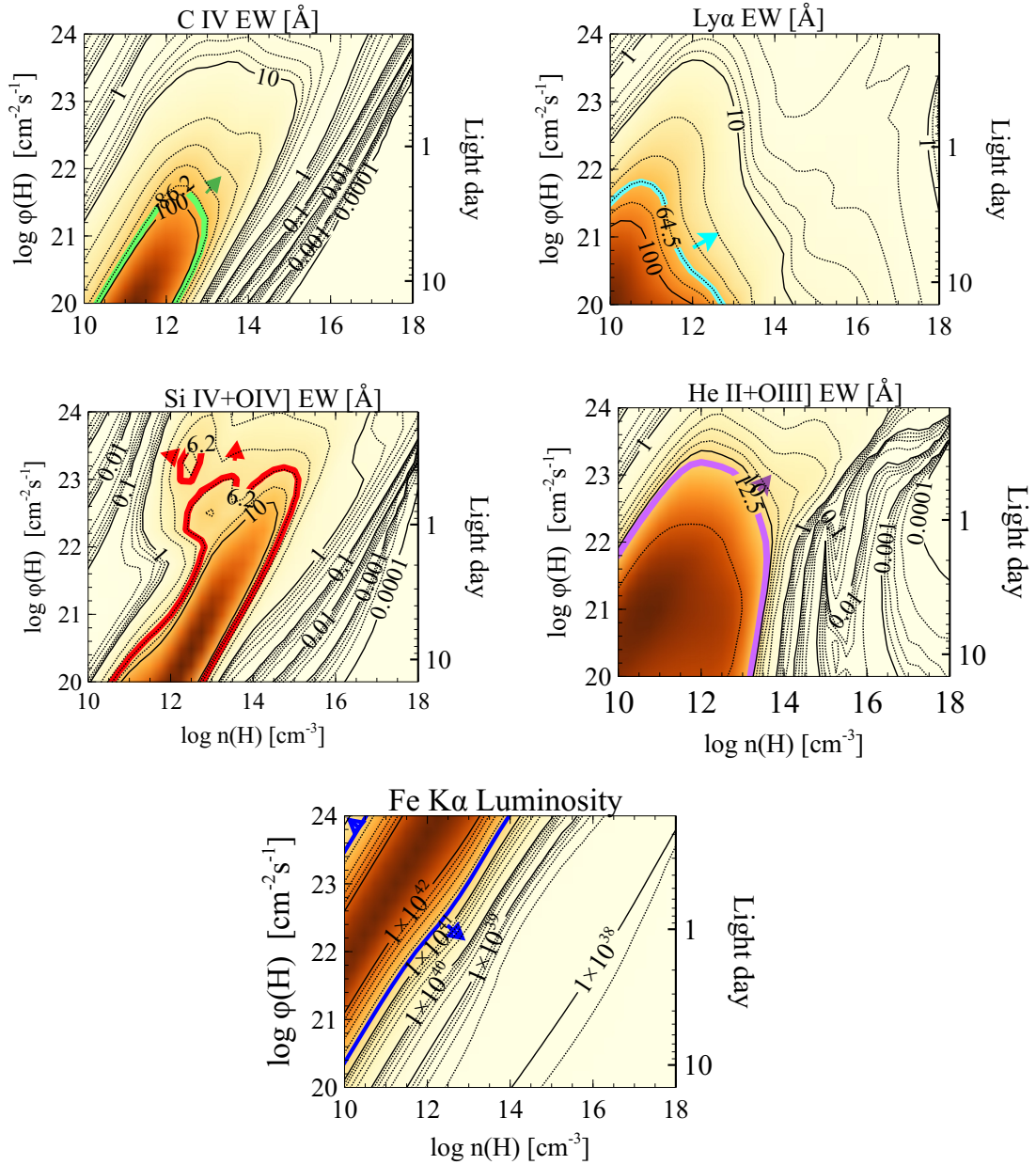


Figure 4.2: Upper four panels show the predicted EW of strong lines emitted by the equatorial obscurer as the contours. The colored lines indicate the HST observed value and arrows show the direction in which the equatorial obscurer must be chosen in order for its emission to not dominate the HST emission lines. All the EWs are relative to the 1215 Å continuum. The lowest panel shows the predicted luminosity of Fe K α as the contours and the blue lines show the XMM-Newton observed values.

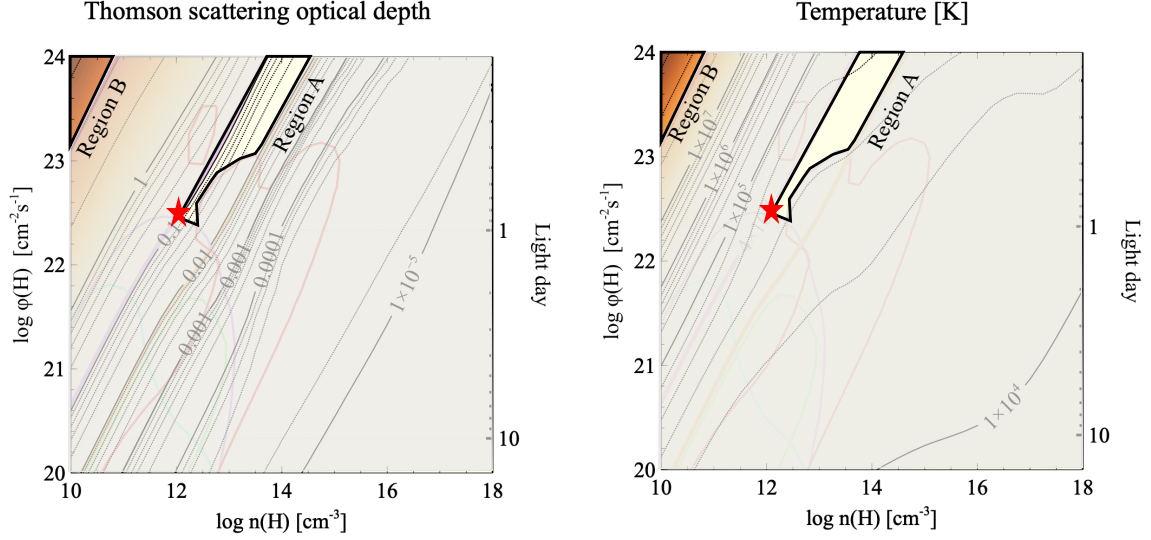


Figure 4.3: The left panel maps the Thomson scattering optical depth and the right panel maps the temperature of the obscurer. A and B are two regions with allowed properties of the equatorial obscurer. The red star indicates our preferred model, which is the most consistent with all observational constraints

As shown in both panels, there are two possible regions for the obscurer’s properties:

Region A: $r < 1$ light days, $10^{12} \text{ cm}^{-3} < n(\text{H}) < 10^{14} \text{ cm}^{-3}$, $\phi(\text{H}) > 10^{22.4} \text{ s}^{-1} \text{ cm}^{-2}$, $10^{4.6} \text{ K} < T < 10^{4.8} \text{ K}$, and $1.2 \times 10^{22} \text{ cm}^{-2} \leq N(\text{H}) < 2 \times 10^{23} \text{ cm}^{-2}$. The low-density bound of the region is set by the luminosity of Fe $K\alpha$, the lower bound by He II, and the high-density bound by LOS column density. It has a Thomson scattering optical depth between 0.01 and 0.1.

Region B: $r < 0.4$ light days, with $n(\text{H}) < 10^{11} \text{ cm}^{-3}$, and $\phi(\text{H}) > 10^{23} \text{ s}^{-1} \text{ cm}^{-2}$, $T \geq 3 \times 10^7$, and $N(\text{H}) \geq 10^{24} \text{ cm}^{-2}$. It has a very high ionization parameter and is Compton thick (Figure 4.2). The lower limit to this region is set by the Fe $K\alpha$ emission. The Thomson scattering optical depth is $\tau_e \geq 4$.

We prefer region A since it produces significant very broad HeII and Fe $K\alpha$ emission, but produces other UV lines with EWs less than half the observed values. The HeII velocity-delay map sets a ≤ 5 day limit to the lag (Horne et al. 2020). This is consistent with almost all of the observed HeII being produced in the equatorial obscurer. As with the UV lines, we assume that half of the Fe $K\alpha$ forms in the obscurer, with the other half in the BLR. Below we show that this is also suggested by the Fe $K\alpha$ line profile, in which half of the line EW forms in the BLR and the rest is a strong broad component that forms in the equatorial obscurer. This might be the very broad Fe $K\alpha$ component mentioned by Cappi et al. (2016) and is produced in the obscurer.

Region B is not of interest for our model of the wind since the EWs of the broad UV lines produced by any winds chosen from this region are almost 1% of the total observed values. Moreover, a wind chosen from region B will be very close to the central source and will emit lines much broader than what was observed.

The parameters for our final preferred model, $\phi(\text{H}) \approx 10^{22.5} \text{s}^{-1} \text{cm}^{-2}$, $n(\text{H}) \approx 10^{12} \text{cm}^{-3}$, $T \approx 5 \times 10^4 \text{K}$, and $\tau_e \approx 0.1$ are shown with a star in Figure 4.3. A wind with these parameters is our favorite model in region A, since it has a major contribution to the HeII and Fe K α emissions. Any other wind selected from region A will emit lower values of the mentioned lines. These conditions place the wind/equatorial obscurer at about one light day from the central source. Please note that although the mentioned hydrogen density seems to correspond to the changing look portion of figure 4 of D19b, since the current paper has adopted a different $\phi(\text{H})$ for the equatorial obscurer, the ionization parameter is nearly the same as case 2 in D19b. This means an obscurer with mentioned $\phi(\text{H})$ and $n(\text{H})$ belongs to the case 2 discussed in D19b and reproduces the holiday. This was expected since by keeping the optical depth constant, we made sure that all of the models in this paper belong to case 2 of d19b.

Figure 4.4 compares our predictions for the CIV and Fe K α line profiles with the observations. To illustrate our preferred model (panels A and C), we adopt a SMBH mass of $M = (5.2 \pm 0.2) \times 10^7 M_\odot$ (Bentz & Katz 2015). Assuming Keplerian motion and the equations given in the first paragraph in section 5.1 of Cappi et al. (2016), the lines produced by the equatorial obscurer have a FWHM of $18500 \pm 3500 \text{ km/s}$. The more recent BH mass estimations are about 50% larger than our adopted value (Horne et al. 2020). This represents the uncertainty in the BH mass measurements and causes 20% uncertainty on the FWHM of our model, since the line width estimation depends on the BH mass. We adopt the mass determined by (Bentz & Katz 2015), to be consistent with Kriss et al. (2019).

Figure 4.4 panels A (theory) and B (HST observations) show the case for CIV, in which we are using arbitrary vertical offsets in flux, simply for illustrative purposes. To produce panel A, we assume that the equatorial obscurer is emitting CIV with an EW half that observed and with FWHM=18500 km/s (blue line), while the BLR emits the flux with FWHM=5000km/s (red line, Kriss et al. 2019). Panel B is the best fit model to the HST STORM observations (Kriss et al. 2019). Those panels suggest that the equatorial obscurer could well be responsible for the very broad component.

Figure 4.4 panels C (theory) and D (NuSTAR and XMM-Newton observations, 2013 Jul 11-12, Jul 23-24, and Dec 20-21) show the same thing for the Fe K α line, but this time we assume that the obscurer produces the emission line with an EW equal to that observed and a FWHM=18500 \pm 3500 km/s (blue line), while the BLR emits Fe K α with FWHM=5500 km/s (red line, Cappi et al. 2016). Panel D shows the observations of Cappi et al. (2016) in which the vertical axis indicates the data as the ratio to a single power-law continuum model fitted to the XMM-Newton (black) and NuSTAR (red) observations. The green horizontal line shows the net FWHM which is calculated by adding the widths of two Gaussian functions with the same central wavelength position in quadrature (the core corresponding to the observed broad Fe K α FWHM=5500 km/s and the XMM-Newton resolution with $dE/E = 1/50$, so FWHM=6000 km/s). This results in a net BLR FWHM \leq 8000 km/s, consistent with the BLR core observed by HST and suggests that the core of the observed Fe K α profile is in good agreement with the our model. Comparing panels C and D, which are equally scaled, shows that the very broad emission from the obscurer might easily hide under the total emission and be just seen as a very broad continuum. This very broad base may be observable in Panel D at $\pm 7000 \text{ km s}^{-1}$.

The total observed Fe K α profile (panel C) is similar to the CIV seen by STORM,

although this is not a strong statement due to the S/N ratio in the X-ray data. Indeed, the total CIV is consistent with the “narrow” Fe K α discussed in Cappi et al. (2016). Motivated by this similarity, we propose that this line also includes the classical BLR emission and a very broad component originated from the wind, hidden in the noise. This scenario is a testable hypothesis for our model and can be the subject of future observations with Chandra / HETG.

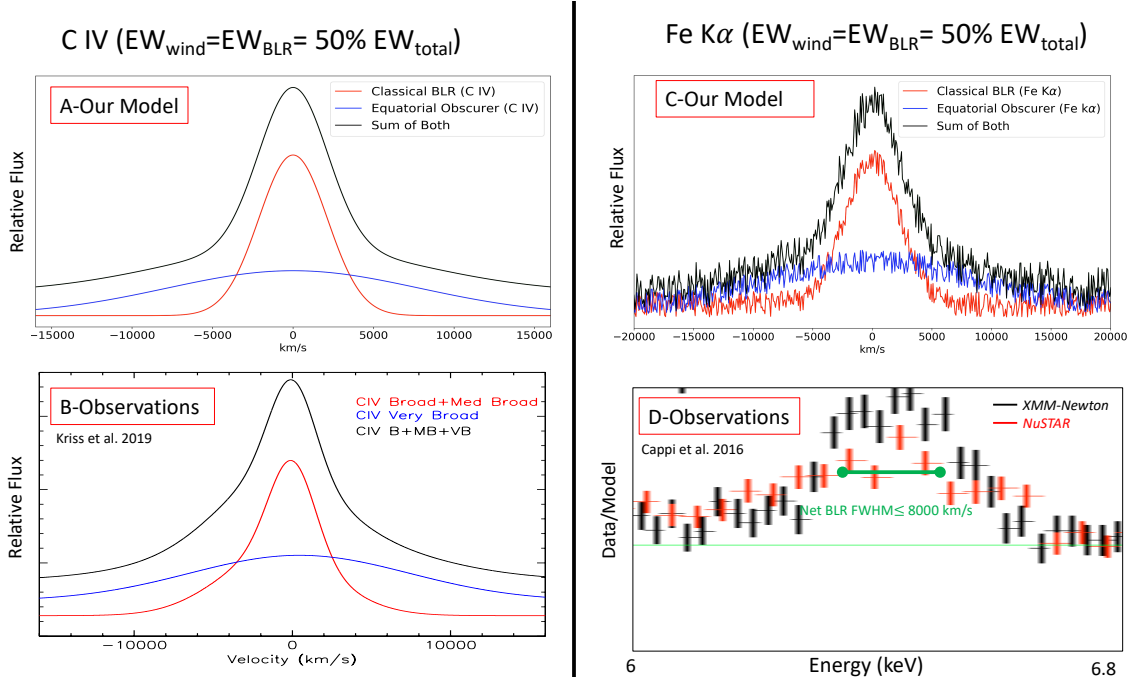


Figure 4.4: This Figure compares our model with the observations from HST, XMM-Newton, and NuSTAR. Panels A & B show the case for CIV, for which the obscurer produces a very broad component (panel A, blue) with an EW of half of that produced by the BLR (panel A, red). Panels C & D show the case for Fe K α , for which the obscurer produces a very broad component (panel C, blue) with an EW equal to that produced by the BLR (panel C, red). It is plausible that a broad base similar to CIV is present, although the S/N is not high enough to say for sure. In both cases our predictions are very similar to the observations, suggesting that the disk wind could be responsible for the observed very broad emission line components.

4.3 Discussion and summary

Here, we have used HST and XMM-Newton observational constraints to derive a model of the equatorial obscurer. We have shown that the equatorial obscurer, which modifies the SED to produce the emission-line holiday, is itself a significant source of line emission, solving several long-standing problems in emission-line physics. The model predicts that lines should have a core formed in the classical BLR and strong broad wings, a profile consistent with the line deconvolution presented in Kriss et al. (2019), and that much of the UV HeII and X-ray Fe K α can originate in the equatorial obscurer. Finally, we found that

the obscurer has a modest optical depth to electron scattering and so adds reflection and scattering to the physics of the line-continuum transfer function and emission-line profiles. This is a unified model of the disk wind in which the remarkable responses of the emission lines in NGC 5548 are explained and the properties of the unobservable part of the wind are derived.

Figure 4.5 shows a cartoon of our derived geometry. This Figure is consistent with figure 1 of D19b, however, here we also consider the emission from the wind. The very bright area, the base of the wind, indicates this emission from the equatorial obscurer. Variations in this part of the wind produce the emission-line holiday (D19b).

This model is also consistent with the Sim et al. (2010) Monte Carlo radiative transfer predictions of the X-ray spectra of a line-driven AGN disc wind. They argued that a disk wind can easily produce a significant strong, broad Fe $K\alpha$ component which has a complex line profile. Based on their simulations, the wind's effects on reflecting or reprocessing radiation is at least as important as the wind's effects on the absorption signatures. Their model was later followed by Tatum et al. (2012), in which a Compton-thick disk wind is responsible for all moderately broad Fe K emission components observed in a sample of AGNs. Their disk wind is not located in the LOS to the source and still affects the observed X-ray spectrum.

The electron scattering optical depth could be larger than estimated here, $\tau_e \sim 0.1$. Our derived parameters are highly approximate suggestions of the properties of the equatorial obscurer. We choose the smallest Lyman continuum optical depth (and H^0 column density) obscurer that is consistent with D19b. Other solutions with similar atomic column density but greater thickness are possible. They would have larger ionized column density and electron scattering optical depth. The Thomson optical depths reported in Figure 4.3 are normal to the slab. A ray passing into the slab at an angle θ will see an optical depth of $\tau_0/\cos\theta$. For isotropic illumination the mean optical depth is $\sqrt{2}$ larger than the normal.

A region with a significant electron scattering optical depth and warm temperature, $T \approx 5 \times 10^4 K$, would solve several outstanding problems, which we summarize next.

It could be a part of the Compton reflector and so constitutes a translucent mirror in the inner regions. Scattering off warm gas will help producing smooth line profiles (Arav et al. 1998), a long-standing mystery in the geometry of the BLR. Gas with these properties also produces bremsstrahlung emission with a temperature similar to that deduced by Antonucci, & Barvainis (1988) and so could provide the location of the non-disk emission. The obscurer modeled here is not a significant source of bremsstrahlung emission, however.

A model with an electron scattering optical depth ≥ 0.5 could provide an obscuration required for explaining the velocity-delay maps of Horne et al. (2020). They show that the emission from the far side of the BLR is much fainter than expected with isotropic emission from the central source and no obscuration. If the base of the wind is transparent we will observe both the near and far sides of the BLR. This indicates that there must be an obscuring cloud between the BLR and the source, acting like a mirror.

D19b proposed that the disk wind can be transparent or translucent. This hypothesis is compatible with figure 4 of Giustini & Proga (2019), in which NGC 5548 is on the border of having a line-driven disk wind or a failed wind. This means that small changes in the disk luminosity/ mass-loss rate will affect the state of the wind. The reason is that

decreasing the disk luminosity leads to a reduction in the mass flux density of the wind, making it over-ionized (Proga & Kallman 2004). A transparent wind has little effect on the SED and no spectral holidays occur, while holidays occur when the wind is translucent. In this state, the equatorial obscurer absorbs a great deal of the XUV / X-ray part of the SED which must be reemitted in other spectral regions.

In this paper, we introduced a new approach to derive the wind's properties. This will have important implications for future studies of AGN outflows and feedback. We used observations to discover the behavior of a part of the wind that can never be directly observed. Our models of the wind will be expanded to better approximate the hydrodynamics of the wind. Deriving these "next generation" hydrodynamical / microphysical models and comparing them with the observations will be the subject of our future study.

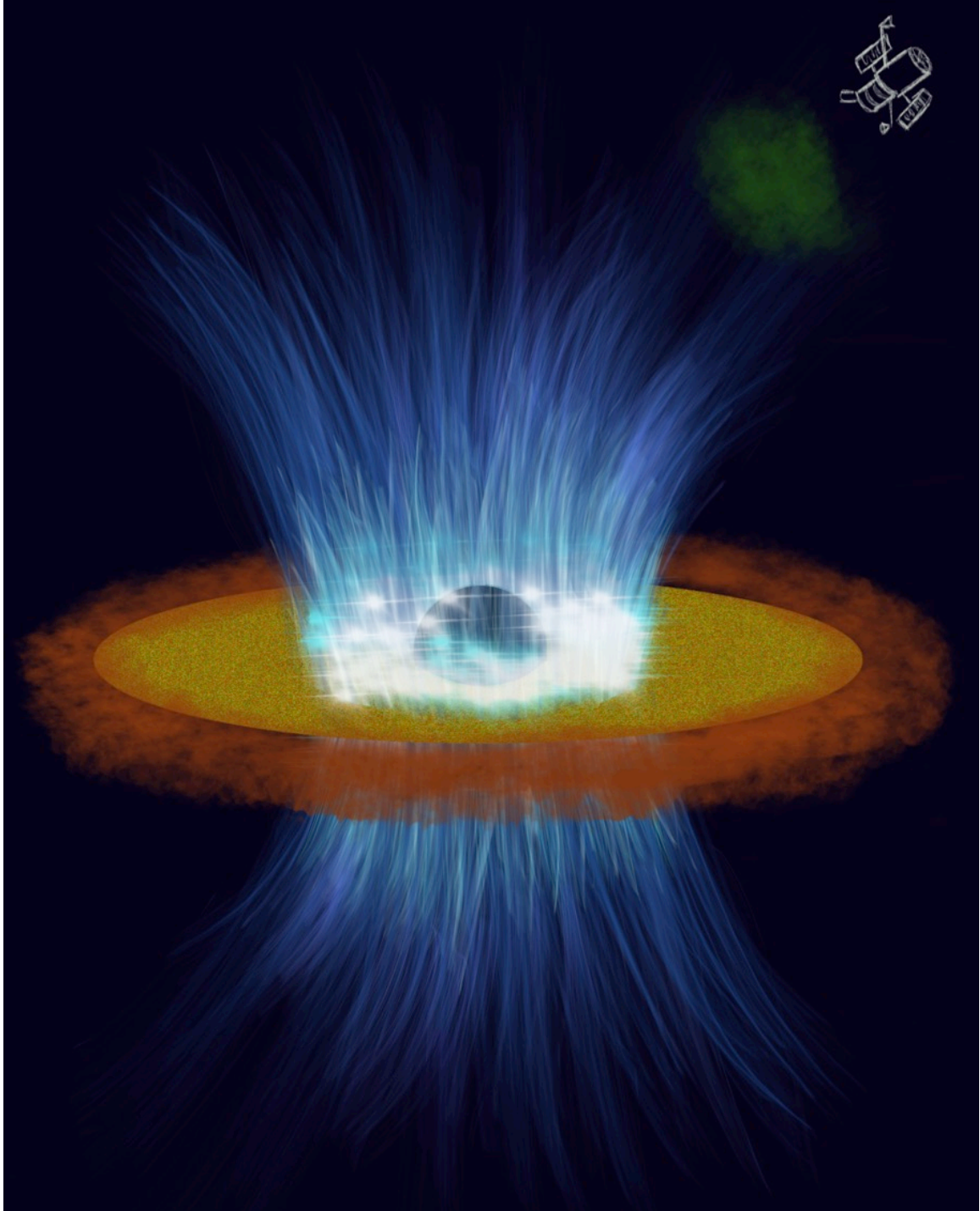


Figure 4.5: Cartoon of the disk wind in NGC 5548 (not to scale). The disk wind (blue) surrounds the central black hole and extends to the line of sight to HST in the upper right corner. The BLR is shown as the orange cloud around the disk. The green cloud at the upper right shows the absorbing cloud discussed in D19a. The bright region in the lower part of the wind indicates that the wind is a major contributor to the very broad components of the observed emission lines

Chapter 5 AN ATLAS OF UV AND X-RAY SPECTROSCOPIC SIGNATURES OF THE DISK WIND IN NGC 5548

While this chapter is motivated by the holiday observed in NGC 5548, we are not trying to model or analyze any specific observation. We examine several ways by which these kinds of winds could affect the SED emitted by the sources and cause a holiday. These results should apply to the family of AGNs. Our goal is to show that cloud shadowing can have a dramatic effect on the spectra, and it must be considered in all AGN studies.

5.1 The disk wind

Figure 1 of D19b shows the geometry of NGC 5548 and includes the disk wind. We refer to the upper part of the wind as the LOS obscurer since it blocks much of the soft X-rays. The LOS obscurer can be directly observed and has a well-determined column density, soft X-ray absorption, and variable covering factor. This obscurer affects the absorption lines (D19a), however, it does not directly affect the emission lines. The LOS obscurer first appeared in 2011 (Kaastra et al. 2014) and began to cover the central source. The portion of the source that is covered by the LOS obscurer varies with time (Mehdipour et al. 2016). During the holiday, it covered $\sim 86\%$ of the X-ray source and $\sim 30\%$ of the UV source (Kaastra et al. 2014).

5.1.1 The obscurers

The base of the wind, launched from the disk, is called the equatorial obscurer. This obscurer is the one which affects the BLR emission lines and produces the emission line holiday. There are no measurements of its column density or any other physical properties, but it is likely denser than the LOS obscurer and has a higher column density since it is closer to the accretion disk, where it was originally produced. D20 proposed physical properties for the translucent equatorial obscurer for which the wind has a constant optical depth to be located at the minimum threshold to produce a holiday (based on figure 4 of D19b). However, a wind from anywhere else within the Case 2 area of D19b figure 4, will still produce the holiday, but will have different properties.

The SED striking the BLR first passes through the equatorial obscurer and D19b argues that this filtering causes the emission-line holiday. This obscurer absorbs a great deal of the original SED, so its emission may be significant. Below we discuss this in more detail.

The hydrogen density and the ionization parameter of both obscurers are unknown. Regarding the LOS obscurer, Kaastra et al. (2014) derived an ionization parameter of $\log \xi = -1.2 \text{ erg cm s}^{-1}$, however, later Cappi et al. (2016), found a much higher ionization parameter, $\log \xi = 0.4 - 0.8 \text{ erg cm s}^{-1}$. Recently Kriss et al. (2019) suggested a still higher ionization parameter of $\log \xi = 0.8 - 0.95 \text{ erg cm s}^{-1}$.

We note that there are two different ionization parameters: ξ and U , which have been used in various STORM papers. The ionization parameter ξ is defined as (Kallman & Bautista 2001):

$$\begin{aligned}\xi &= (4\pi)^2 \int_{1R_{yd}}^{1000R_{yd}} \frac{J_\nu d\nu}{n(H)} = \frac{F_{ion}}{n(H)} \\ &= \frac{L_{ion}}{n(H)r^2} [\text{erg cm s}^{-1}]\end{aligned}\quad (5.1)$$

while the ionization parameter U is dimensionless and is defined by:

$$U = \frac{Q(H)}{4\pi r^2 n(H) c}, \quad (5.2)$$

in which $Q(H) = \int_{1R_{yd}}^{\infty} \frac{L_\nu d\nu}{h\nu}$ is the total ionizing photon luminosity. For the unobscured SED of NGC 5548, $\log U = \log \xi - 1.6$.

As figure 3 of D19b shows, the SED can be dramatically affected when the hydrogen density gets more substantial. The situation may be the same if other parameters, like metallicity, change. This paper examines a range of obscurer parameters to check for observed properties and possible predictions.

5.1.2 The covering factors and implications for explaining the holiday

Three different types of covering factors will enter in the following discussion. First, the line of sight covering factor, LOS CF. It is the fraction of the continuum source covered, as seen from our line of sight. This covering factor is directly measured through the hardness ratio estimations based on the *Swift* observations (Mehdipour et al. 2016). Second, the global covering factor, GCF, the fraction of the sky covered by a cloud, as seen from the central object (Wang et al. 2012). This type of CF is not in our LOS, and it matters when we study the total emission luminosity of an obscurer emission-line holiday. Third, the ensemble covering factor, ECF. This covering factor accounts for the total portion of the source covered by all clouds in all directions. The ensemble global covering factor is typically 20% and can be determined from the equivalent width (EW) of emission lines (Osterbrock & Ferland 2006).

D19a describes a physical model that explains the absorption-line holiday as a result of changes in the LOS CF of the obscurer. In this model, the SED passes through the LOS obscurer before striking the absorption cloud. There is a minimal transition in EUV and soft X-ray. However, the FUV part of the SED is almost not touched. High ionization species are affected by these changes in a way that the absorption-line holiday occurs. This explanation is only reliable for the case of a LOS obscurer and is consistent with 2013 *swift* observations of NGC 5548.

The equatorial obscurer shields the BLR, altering the SED striking it. The ECF of the BLR is unusually large, 50%, in NGC 5548 (integrated cloud covering fraction; Korista & Goad 2000), so the global covering factor of the equatorial obscurer must also be this large to explain the BLR holiday (D19b). For this reason, a CF-based model cannot explain the emission-line holiday. The equatorial obscurer, which is much closer to the BH than the BLR and is likely to be the base of the wind, has instabilities in its mass-loss rate leading to variations in its hydrogen density. D19b explains that the variations of the hydrogen density of the equatorial obscurer can give rise to the emission-line holiday.

These different covering factors matter because they define the portion of the spectrum absorbed by the obscurer. This affects the ability to block the SED striking the outer clouds, and also determines the emission from the obscurer. Below we show how changes in the parameters of the obscurer affect the SED transmitted through it or emitted by it.

5.2 The effects of different parameters-general considerations

As mentioned earlier, two obscurers affect the spectrum of NGC 5548: the LOS obscurer with its impact on intervening absorption lines, and the equatorial obscurer with its impact on the broad emission line clouds. These obscurers have many free parameters and variations of any of these parameters will change the transmitted SED. This section considers the effects of these parameters starting from a standard model of the LOS obscurer. This offers a good starting point since it is the one with direct measurements and modeling of its absorption properties. Surprisingly, there has never been a systematic exploration of the physical properties of absorbing gas and its effects on the SED transmitted through it.

5.2.1 A typical cloud

Mehdipour et al. (2015) derived a standard or baseline model for the LOS obscurer in NGC 5548. Their model suggested that the obscurer blocked all of the SED between the FUV (13.6 eV) and the X-ray (1 keV). The complicated changes in the narrow absorption lines, where their degree of line-continuum correlation depends on ionization potential (Kris et al. 2019), suggests that a portion of the SED may be transmitted through the obscurer. The EUV and XUV portions of the transmitted SED are incident upon and ionize the UV absorbing cloud. This transmitted SED depends on the obscurer's energy-dependent optical depth, which in turn depends on the the obscurer's metallicity (Z), hydrogen number density $n(\text{H})$, and ionization parameter (ξ or U).

Some of the physical properties of the LOS obscurer are known since we observe it in absorption, while no properties of the equatorial obscurer are observationally identified, although it is arguably more important since it changes the relative strength and response amplitude of the emission lines. D20 used a new approach to propose some parameters for the equatorial obscurer. The SED transmitted through or emitted by each of the obscurers is dependent on their column density, hydrogen density, ionization parameter (or distance from the source), and metallicity. Here we investigate this dependency by modeling different obscurers with different values for these parameters. We start with a typical cloud, assuming a density that is typical of the BLR, $n(\text{H}) = 10^{10} \text{cm}^{-3}$, and we adopt the intrinsic SED described in figure 3 of D19a. We assume solar abundances (photospheric), which is `Cloudy`'s default value (Ferland et al. 2017) unless otherwise specified. We start by keeping the optical depth at 1 keV constant at the value that was directly observed. This largely reproduces the obscured SED shown in Mehdipour et al. (2015). Please note that the best related models assume there are in fact two separate LOS obscurers with different physical properties such as column density, ionization parameter, and covering factor.

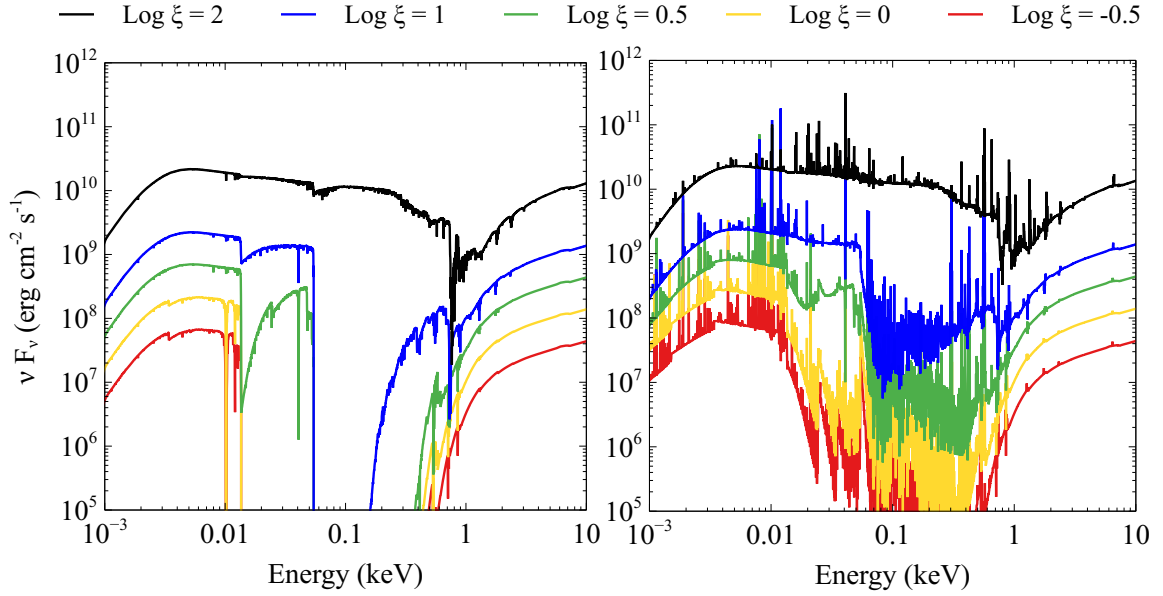


Figure 5.1: Left panel: The obscurer’s transmitted SED. As the lines show the transmitted SED is very sensitive to the ionization parameter in soft X-ray energies. Right panel: total emission (sum of the transmitted and reflected continua plus attenuated incident continuum) from the obscurer for different values of the ionization parameter. The attenuated incident continuum is included. The spectra represent $\log \xi = 2, 1, 0.5, 0,$ and -0.5 from top to bottom. (There is an animation associated with this Figure which shows how the transmitted SED responds to the variations of the ionization fraction).

5.2.2 Varying the ionization parameter

We predict transmitted and emitted SEDs by changing the ionization parameter (ξ) but keeping all other quantities constant. Changes in the ionization parameter are equivalent to changes in the luminosity of the source. Thus, this section also accounts for variations of the central source luminosity.

To keep the thickness of the cloud constant, we kept the optical depth constant. These models do not necessarily illustrate the obscurers of NGC 5548 but show how sensitive the transmitted/emitted SEDs could be to the variations of the ionization parameter. We ran `CLOUDY` (Ferland et al. 2017) for a grid of ionization parameters between -1.5 and 2 with steps as small as 0.025 dex. Figure 5.1 shows examples of both the transmitted SED and the total emission from the obscurer for five different values of the ionization parameter ξ . Please note that in this paper, all the Figures which are labeled to be the emission from the obscurer are actually the total emission, which is the sum of the transmitted and reflected continua and lines and assume 100% covering factor. The attenuated incident continuum is also shown.

As the left panel of Figure 5.1 shows, the transmitted SED is spectacularly dependent on the value of the ionization parameter: clearly, the EUV part of the SED strongly depends on the ionization parameter while the XUV is always strongly attenuated unless we adopt a very high ionization parameter. For some ionization parameters, the EUV region is totally

blocked, and for others, transmitted. When it comes to the emission from the obscurer, this dependency seems not to be as much as the transmitted SED, however, the higher the ξ is the more emission is predicted.

Figure 5.1, left panel, shows three different styles of transmitted SED. These correspond to three different ionization states for hydrogen and helium within the obscurer. In order of decreasing ionization parameter, which lowers the ionization, increases the opacity, and decreases the transmission, these are:

- Case 1) Very high ξ and ionization: Hydrogen is highly ionized, and the SED is fully transmitted. There is no ionization front in this case. The higher ionization means that all of the EUV and XUV passes through the cloud. There is not enough singly ionized helium to fully absorb the XUV. In other words, the obscurer is transparent.
- Case 2) Intermediate to high ξ and ionization: Some of the EUV is transmitted, while little XUV light is transmitted. In this case, there is no $\text{He}^0\text{-He}^+$ ionization front, but there is a $\text{He}^+ - \text{He}^{++}$ ionization front. Enough atomic hydrogen is present to block much of the EUV, and the XUV is fully blocked by large amounts of singly ionized helium. In some samples of Case 2 (green line), there is a shallow $\text{H}^0 - \text{H}^+$ ionization front, however in other samples (blue), there is almost no hydrogen ionization front.
- Case3) Low ξ , low ionization: All EUV and XUV light is blocked. There is an H^0 ionization front. There are significant amounts of atomic H that absorb much of the ionizing continuum. This is similar to the Mehdipour et al. (2015) standard model of the obscurer. This is also the case for the LOS obscurer during the AGN STORM campaign and was assumed by Arav et al. (2015) and D19a.

All the SEDs resulting from the full range of the adopted ionization parameters fall into one of these categories. Below we show that it does not matter which parameter of the obscurer is changing; the resulting transmitted SED will always be one of these three cases.

It is worth emphasizing that although we are motivated by the obscurers in NGC 5548 and we use this AGN as our point of reference, our discussion provides a framework for future AGN modeling. We study the effects of different obscurer properties on the transmitted SED. While all of the presented simulations use the properties of NGC 5548 and its obscurers as input, the approach should have a broader application.

5.2.2.1 A physical interpretation of three transmitted cases

We quantify the effects of these changes on the SED in Figure 5.2, which investigates variations of the ionization parameter, the independent axis, while the optical depth is kept constant. The upper panel gives the H^0 column density. The lower panel shows the ratio of the intensity of the transmitted continuum at 399 Å (EUV) relative to that at 1356 Å (FUV). We selected these two wavelengths because they belong to two separate energy regions with very different responses to the changes in the ionization parameter, so they quantify the changes between the Cases described above. *HST* measures the 1356 Å point while we expect that a photoionized cloud is most affected by the 399 Å point. This shows that the

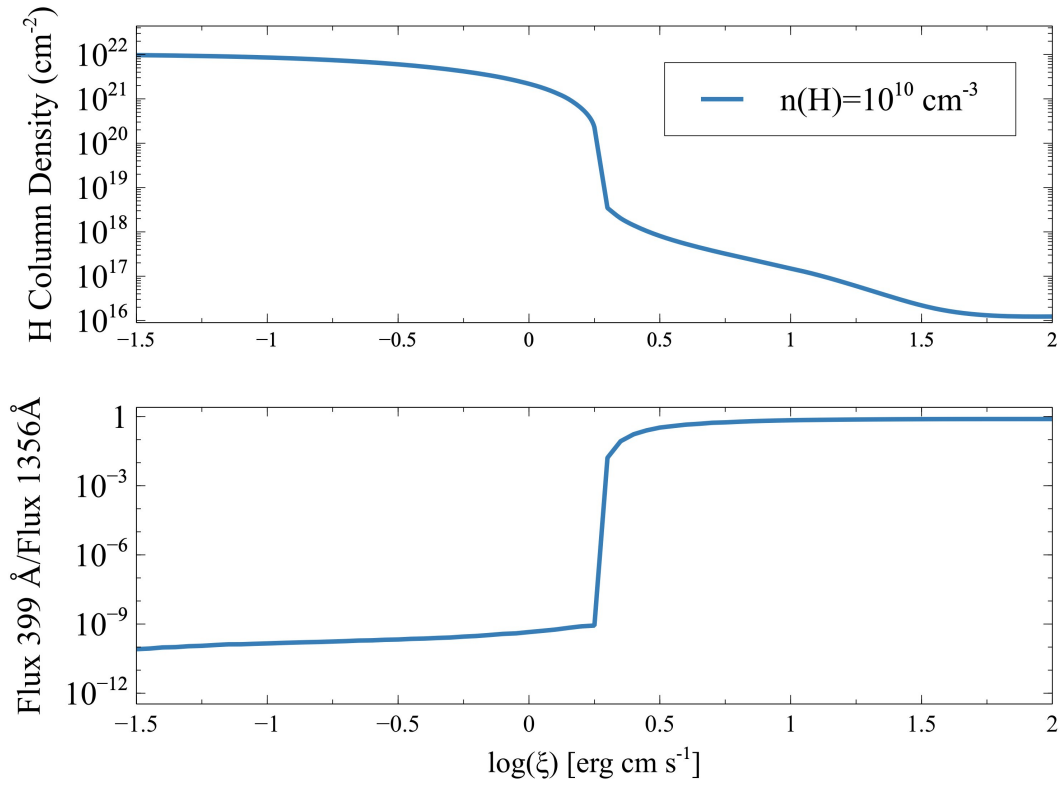


Figure 5.2: Top panel shows the variation of atomic hydrogen column density as the ionization parameter changes. The bottom panel shows the ratio of 399Å/1356Å as a function of the ionization parameter.

399 Å continuum is strongly extinguished for low ionization parameters, corresponding to Case 3. The abrupt change in the 399 Å transmission and the atomic hydrogen column density occurs at the ionization parameter where there is no longer a hydrogen ionization front, and the cloud is highly ionized. This is the transition from Case 3 to Case 2. If the extinction changes due to a transition between Case 3 and 2, then the ionization state of the absorption cloud will not directly track the *HST* continuum.

5.2.2.2 An upper limit for the ionization parameter

It is possible to calculate the upper limit of ionization parameter U (and so ξ) for which each of these cases could be possible. This will help to adjust the limit on the ionization parameter based on the model. Below we calculate three different maximum value ionization parameters for which a cloud could have ionization fronts and so modify the transmitted SED. We assume that the cloud has a column density of $N(\text{H}) = 1.2 \times 10^{22} \text{cm}^{-2}$. We also assume that the nebula is optically thick with a temperature of $T = 10^4 \text{K}$.

The transmitted continuum has to be opaque at the hydrogen edge to have an $\text{H}^0\text{-H}^+$ ionization front. This means that all the photons with energies more than 1 Rydberg are

absorbed by the neutral hydrogen and an electron and H^+ are produced ($H^0 + \gamma \rightarrow H^+ + e^-$) also there is an equilibrium balance. Photoionization balance is the detailed balance between photoionization and recombination by electrons and ions (Osterbrock & Ferland 2006):

$$\begin{aligned}\phi(H) &= n_e \alpha_B(H, T) n_{H^0} L_{Stromgren} \\ &= n_e \alpha_B(H, T) N_{IF}(H^+),\end{aligned}\tag{5.3}$$

in which IF stands for the ionization front.

$$\Rightarrow N_{IF} = \frac{\phi(H)}{n_e \alpha_B(H, T)}\tag{5.4}$$

Since it is always the case that $N_{IF} < N$:

$$\frac{\phi(H)}{n_e \alpha_B(H, T)} < 1.2 \times 10^{22} \text{cm}^{-2}\tag{5.5}$$

and:

$$\phi(H) = U c n_e\tag{5.6}$$

$$\Rightarrow \frac{U c}{\alpha_B(H, T)} < 1.2 \times 10^{22} \text{cm}^{-2}\tag{5.7}$$

while

$$, \alpha_B(H, 10^4 \text{K}) = 2.59 \times 10^{-13} \text{cm}^3 \text{s}^{-1}, \text{ so:}$$

$$\Rightarrow U < 10^{-0.98}\tag{5.8}$$

This is the upper limit in the hydrogen ionization parameter that ensures a hydrogen ionization front. We can always use the relationships explained in D19a to transform between U and ξ (for the SED of NGC 5548: $\log U \approx \log \xi - 1.6$).

The exact same discussion works for the $\text{He}^0\text{-He}^+$ ionization front, in which the equilibrium state is:

$$\begin{aligned}\phi(\text{He}^0) &= n_e \alpha_B(\text{He}^0, T) n_{\text{He}^0} L_{Stromgren} \\ &= n_e \alpha_B(\text{He}^0, T) N_{IF}(\text{He}^+)\end{aligned}\tag{5.9}$$

We assume the cosmic abundance ratio of He/H to be almost 10%. This results in a helium column density of $N(\text{He}^+) = 0.1 \times N(\text{H})$, so to have a helium ionization front:

$$\phi(\text{He}^0) = n_e \alpha_B(\text{He}^0, T) N_{IF}(\text{H}) \times 0.1\tag{5.10}$$

$$\begin{aligned}\frac{\phi(H)}{n_e} \times \frac{\phi(\text{He}^0)}{\phi(H)} \times \frac{1}{\alpha_B(\text{He}^0, T) \times 0.1} = \\ U c \times \frac{\phi(\text{He}^0)}{\phi(H)} \times \frac{1}{\alpha_B(\text{He}^0, T) \times 0.1} < 1.2 \times 10^{22},\end{aligned}\tag{5.11}$$

in which $\alpha_B(\text{He}^0, 10^4\text{K}) = 2.72 \times 10^{-13} \text{cm}^3 \text{s}^{-1}$.

For the adopted SED and an obscurer located at $r \approx 10^{18} \text{cm}$ (to be consistent with the LOS obscurer), we find:

$$\begin{aligned}\phi(\text{H}) &= 2.27 \times 10^{17} \text{cm}^{-2} \text{s}^{-1} \\ \phi(\text{He}^0) &= 1.12 \times 10^{17} \text{cm}^{-2} \text{s}^{-1} \\ \phi(\text{He}^+) &= 4.22 \times 10^{16} \text{cm}^{-2} \text{s}^{-1}\end{aligned}$$

These result in:

$$\Rightarrow U < 10^{-1.65} \quad (5.12)$$

And similarly, to have a $\text{He}^+ \text{-He}^{++}$ ionization front:

$$\phi(\text{He}^+) = n_e \alpha_B(\text{He}^+, T) N_{IF}(\text{He}^{++}) \quad (5.13)$$

for which $N_{IF}(\text{He}^{++}) \approx N_{IF}(\text{He}^+) = 0.1 \times N(\text{H})$ and $\alpha_B(\text{He}^+, 10^4\text{K}) = 1.5 \times 10^{-12} \text{cm}^3 \text{s}^{-1}$, so:

$$U c \times \frac{\phi(\text{He}^+)}{\phi(\text{H})} \times \frac{1}{\alpha_B(\text{He}^+, T) \times 0.1} < 1.2 \times 10^{22} \quad (5.14)$$

$$\Rightarrow U < 10^{-0.48}. \quad (5.15)$$

Table 5.1 summarizes the results. Please note that if we use a different location for the obscuring cloud, all the values for $\phi(\text{H})$, $\phi(\text{He}^0)$, and $\phi(\text{He}^+)$ will change accordingly and by the same scale. Thus, based on equations 5.11 and 5.14, the final results will stay unchanged.

Table 5.1: Upper limits for the ionization parameter to have various ionization fronts.

Ionization Front	$\log U_{\text{Max}}$	$\log \xi_{\text{Max}}$
$\text{H}^0 \text{-H}^+$	-0.98	0.62
$\text{He}^0 \text{-He}^+$	-1.65	-0.05
$\text{He}^+ \text{-He}^{++}$	-0.48	1.12

These results are more or less consistent with the expectations. The homology relation between the ionization parameter and the ionization of the gas assumes that the total recombination rate coefficient does not depend on the hydrogen density. This is true at low densities where recombination to highly excited states will decay to the ground state. At inter-mediate to high densities, electron collisions can ionize these levels, making recombination less efficient. A ‘‘collisional radiative model’’ (CRM) is needed to properly describe the recombination process at such densities. `Cloudy` has such a model for one and two electron ions (section 3.2, Ferland et al. 2017) but not for many-electron systems. CRM processes do not affect the X-ray opacity since that is produced by inner-shell electrons.

The models presented here keep the total X-ray optical depth (at 1 keV) the same. As the density increases, H and He tend to become more ionized due to the increasing contribution from collisional (CRM model), and the EUV and XUV transmission increases. Because of the CRM, changing the density is very similar to changing the ionization parameter, due to due to the decreased efficiency in recombination. (Ferland et al. 2017).

5.2.3 Varying the Column Density

The column density, $N(\text{H})$, is the number of atoms along the line of sight per unit area. In the simple case of a constant density $n(\text{H})$ cloud with thickness δR , $N(\text{H}) = n(\text{H})\delta R$. It is evident that a thicker or denser cloud would have a larger column density. To see how different values of the obscurer's column density will affect the shape of the transmitted/emitted SED, we first multiplied optical depth of the LOS obscurer by four to make the cloud thicker than what was observed. Figure 5.3 shows the ionization structure versus depth for such a thick cloud, with an ionization parameter of $\log \xi = -1.2 \text{ erg cm s}^{-1}$. In this Figure, the vertical dashed lines show three different depths that we will consider further. These are referred to as Case 1, Case 2, and Case 3 in the discussion below and we will show that they produce transmitted SEDs similar to those in Figure 5.1. These depths are chosen because, as the Figure shows, they correspond to different hydrogen and helium ionization states. The transmitted SED in each case reproduces one of the three cases discussed above and by D19b.

As Figure 5.3 shows, the ionization structure is very sensitive to the thickness of the cloud. The absorbing power of a cloud is proportional to the column density so larger column densities produce lower ionization as averaged over the cloud.

For the Case 1, both hydrogen and helium are fully ionized. As the red line shows, in Case 1, the amount of He^+ is much smaller than H^+ and He^{++} . There is not enough singly ionized helium to absorb the XUV. This means that the obscurer is transparent, and the intrinsic SED is fully transmitted. We propose that this is the case in most of AGNs: They DO have disk winds, but if the winds are in a transparent state no effects are observed. For Case 2, He^{++} recombines to form He^+ while H remains ionized. Both the transmitted SED and emitted He II photons will ionize any remaining H^0 . This is why the He^+ zone is also an H^+ zone. There is enough He^+ to block a portion of the XUV although a significant fraction is transmitted. The presence of a He^{++} - He^+ ionization front causes much of the $54 \text{ eV} < h\nu < 200 \text{ eV}$ transmitted SED to be absorbed. This reproduces Case 2 discussed by D19b: the case in which the BLR holiday happens. Finally, for Case 3, photons with energies more than 13.6 eV are absorbed and atomic H and He forms. This reproduces Case 3 of D19b: a changing look quasar. In this case H^+ , He^+ and He^{++} ionization fronts are present.

Figure 5.4 shows the transmitted SED and the emission from the cloud for the three cases. The red line shows the SED for the Case 1 cloud. This SED is not strongly extinguished since there is no ionization front and hydrogen and helium remain ionized. In Case 2 and Case 3 hydrogen and helium ionization fronts occur, the SED is strongly absorbed and the diffuse continuum emission increases (Korista & Goad 2001; Korista & Goad 2019; Lawther et al. 2018).

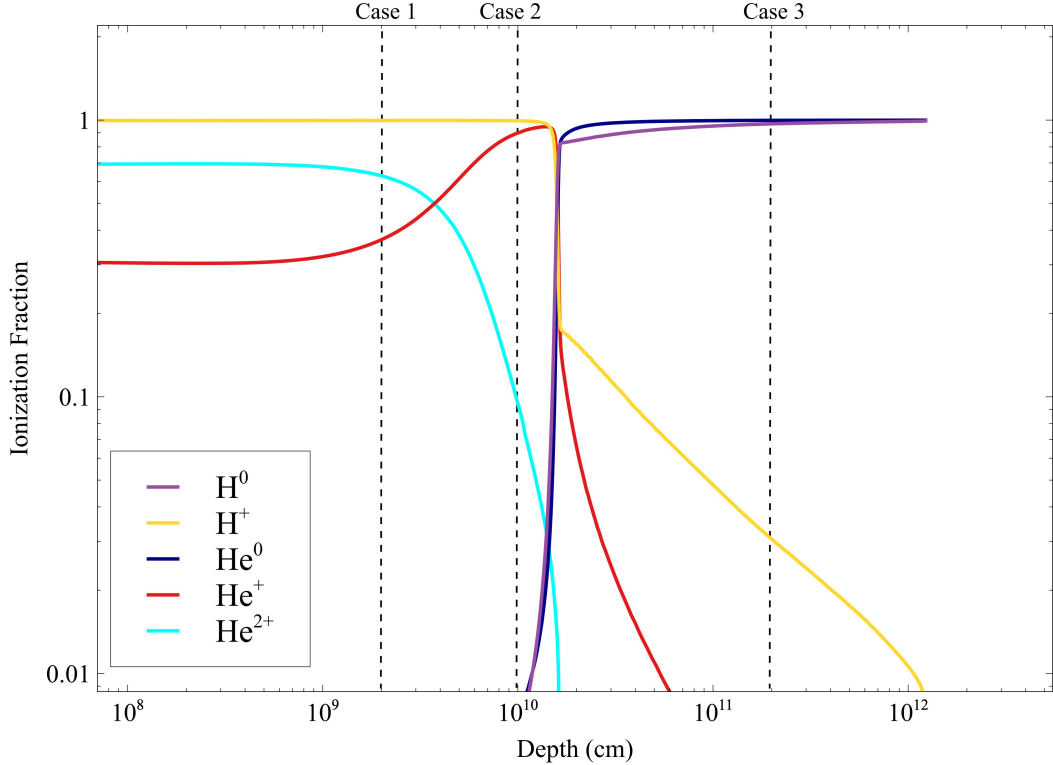


Figure 5.3: The ionization fraction of the noted ions as a function of the depth into the cloud (lower X-axis) in correspondence with the hydrogen column density (upper X-axis). The dashed lines show the depths corresponding to cases 1, 2, and 3, for assumptions of fixed gas density and incident ionizing photon flux. Figure 5.4 shows how the transmitted and emitted SEDs would be for these three different depths.

5.2.4 Varying the Hydrogen Density

The hydrogen density of the LOS obscurer is poorly constrained. Here, we predict SEDs for different hydrogen densities while keeping the soft X-ray optical depth constant. We investigate the effects of changing density for two different values of the ionization parameter ($\log \xi = 0.5 \text{ erg cm s}^{-1}$ corresponding to Case 2, and $\log \xi = -1.2 \text{ erg cm s}^{-1}$, corresponding to Case 3). Varying ξ is equivalent to changing the distance between the obscurer and the accretion disk. Figure 5.5 shows the results.

In each of the four panels of the Figure 5.5, the ionization parameter is kept constant while the density varies. As noted earlier, simple homology relations suggest that clouds with similar ionization parameters, but different densities and flux of ionizing photons, should have the same ionization (Ferland 2003). The results for the lower ionization clouds are fairly similar. The results for the higher ionization parameter shown in the lower-left panel are surprising because the higher density clouds are more highly ionized and transparent. This is caused by the increasingly important role of collisional ionization from

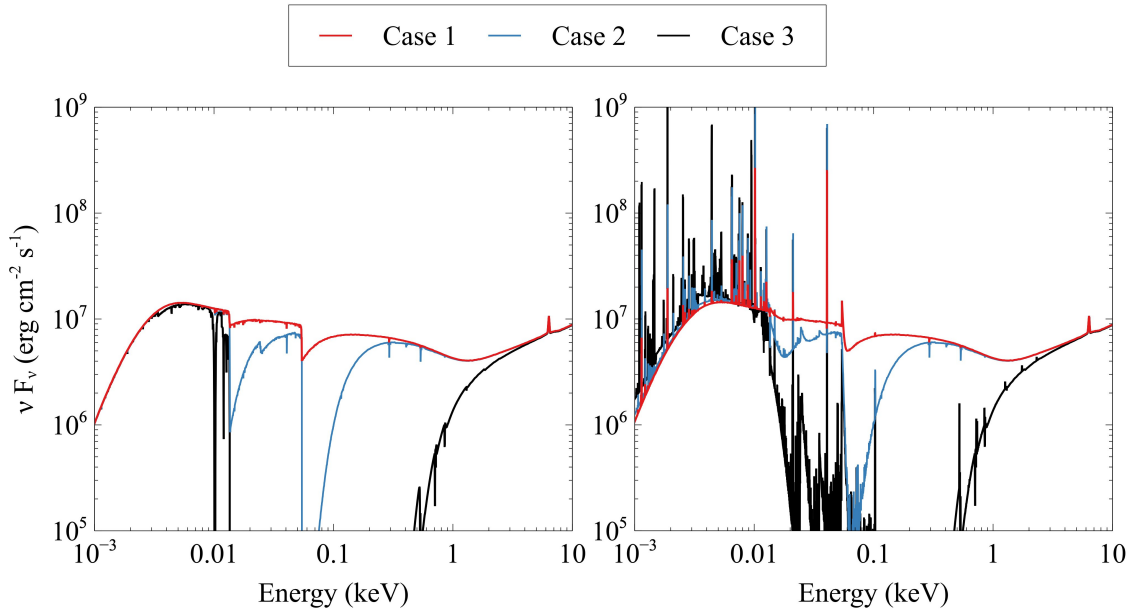


Figure 5.4: : Left panel: transmitted SED in different depths of a thick cloud. Right panel: total emission (sum of the transmitted and reflected continua plus attenuated incident continuum) from the obscurer for the same three cases.

highly excited states in the high-radiation environment, as discussed earlier.

As the right panels of Figure 5.5 show, for energies in UV/optical regions, the obscurer also emits. This extra emission is stronger when the obscurer is denser. This excess of emission is mainly due to hydrogen radiative recombination in the optical and NIR and bremsstrahlung in the IR.

Figure 5.6 is similar to Figure 5.2. In this Figure, the upper panel shows the variations of the H^0 column density as a function of the ionization parameter for three different hydrogen densities. As in Figure 5.2, the lower panel shows the ratio of the intensity of the transmitted continuum at 399 \AA (EUV) relative to that at 1356 \AA (FUV), this time for three different values of hydrogen density.

Please note that for the low densities, the CRM effects discussed earlier, are not important and simple photon conserving arguments hold. However, the CRM effects are considerable for higher densities and would affect the ionization front algorithm. This is the reason that we see different hydrogen ionization fronts for different values of the hydrogen density when the ionization parameter is $\log \xi = 0.5 \text{ erg cm s}^{-1}$.

5.2.5 Varying the Metallicity

We have assumed solar metallicity so far, and we next vary this. Since most soft X-ray absorption is produced by K-shell electrons of the heavy elements, one can expect that if we raise the metallicity by some factor, the hydrogen column density will fall by the same factor to keep the heavy element column density, and X-ray optical depth, the same. We

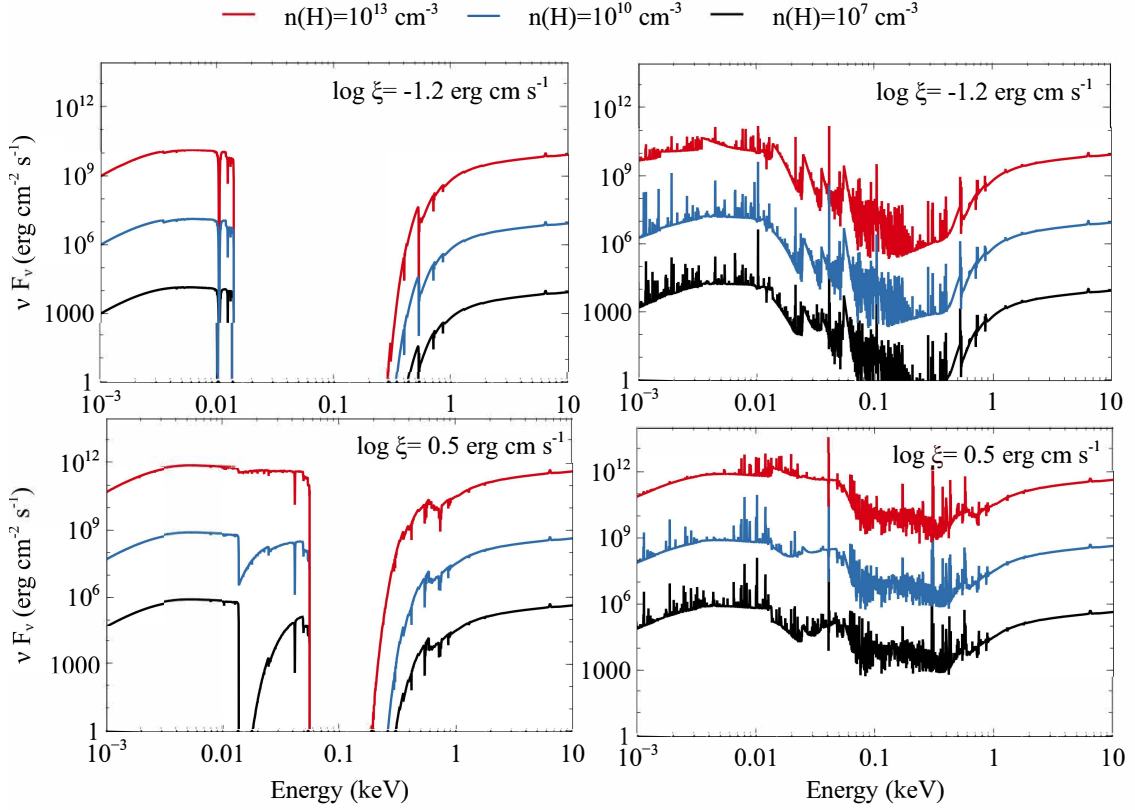


Figure 5.5: Changes in the SED for different values of the obscurer hydrogen density for two models of ionization parameters. Both upper panels have ionization parameter $\log \xi = -1.2 \text{ erg cm s}^{-1}$. Upper left panel shows the results for the transmitted SED and the upper right shows the results for the total emission from the obscurer (sum of the transmitted and reflected continua plus attenuated incident continuum). Lower panels show the same concept for an ionization parameter $\log \xi = 0.5 \text{ erg cm s}^{-1}$.

checked this by modeling the transmitted and emitted SEDs for two very different values of the metallicity in two different models of ionization parameters.

The upper panels of Figure 5.7 show the transmitted SEDs (upper left) and the emission from the obscurer (upper right) for solar metallicity (Z_{\odot}) and $10 \times Z_{\odot}$ for the ionization parameter $\log \xi = -1.2 \text{ erg cm s}^{-1}$. Clearly, the transmitted SEDs of the upper left panel fall in Case 3 category. As both upper panels show, changing the metallicity does not profoundly affect the SED when we are in this case.

The lower panels have an intermediate ionization parameter, $\log \xi = 0.5$. Much of the soft X-ray extinction in the lower-left panel is produced by inner shell photoabsorption of the heavy elements. Although the 1 keV extinction, mainly produced by inner shells of O, C, is the same, the extinction around 200 – 400 eV changes significantly. The opacity in this range is mainly due to He and H (figure 10 of D19a) and little H^0 or He^0 is present. There is almost no hydrogen ionization front in the $Z = 10 \times Z_{\odot}$ case because the hydrogen column density is ten times smaller, as shown next. So, in this respect, the model behaves like Case 2 with no hydrogen ionization front.

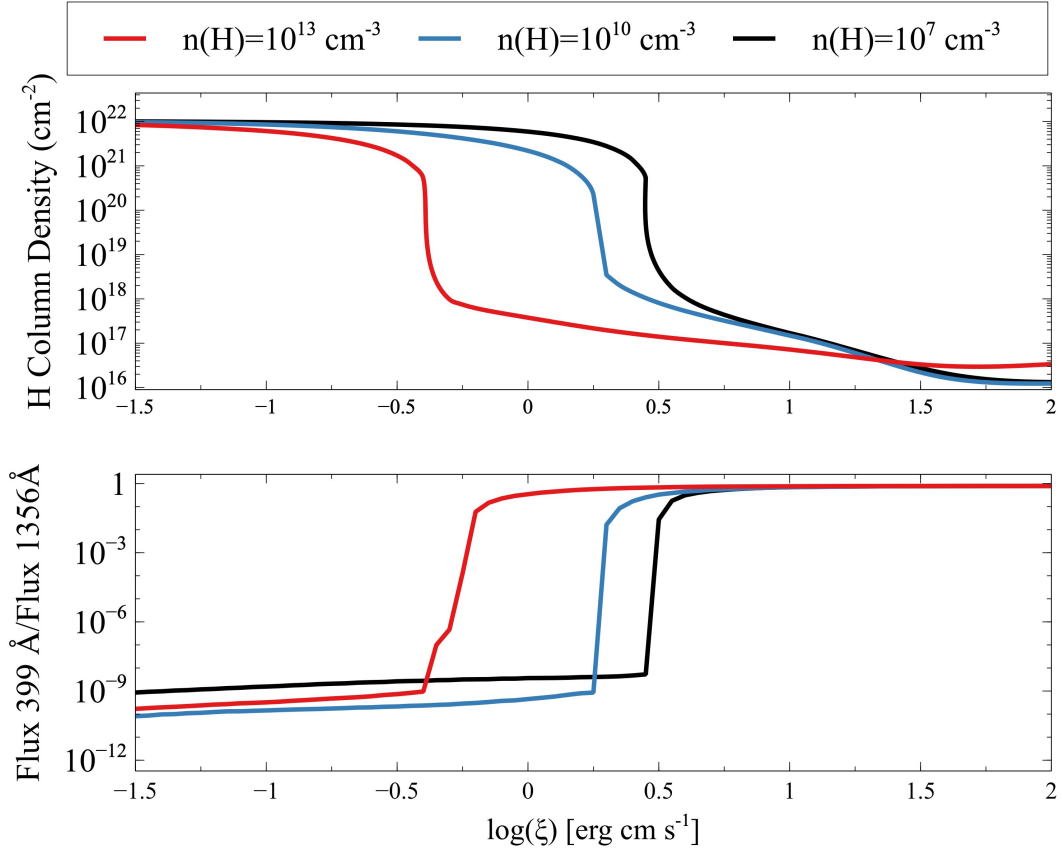


Figure 5.6: Top panel shows the variation of atomic hydrogen column density as the ionization parameter changes, for three different hydrogen densities. The bottom panel shows the ratio of 399Å/1365Å as a function of the ionization parameter for the same three hydrogen densities.

Figure 5.8 is the equivalent to Figure 5.6, but for different metallicities. As expected, for the case with higher metallicity, the hydrogen column density is about 10 times smaller at low and high ionization parameters. However, there are much greater differences at intermediate ξ , around $\log \xi = \pm 0 \text{ erg cm s}^{-1}$. For these parameters, the locations of the hydrogen and helium ionization fronts, in the high-Z case, straddle the outer edge of the cloud and large changes in opacity occur.

5.2.6 Summary

All of the above discussions show that the SED filtered through an obscurer or reflected by it might change slightly or dramatically, depending on the obscurer's properties. When the filtering happens, as in the case of NGC 5548, we could observe the original SED, the absorbed SED, and the reflected SED. Usually, it is not possible to directly measure the obscurer's properties, however, by having the SEDs transmitted/reflected through the obscurer, one can find the characteristics of the obscurer itself, as demonstrated in D19b & D20.

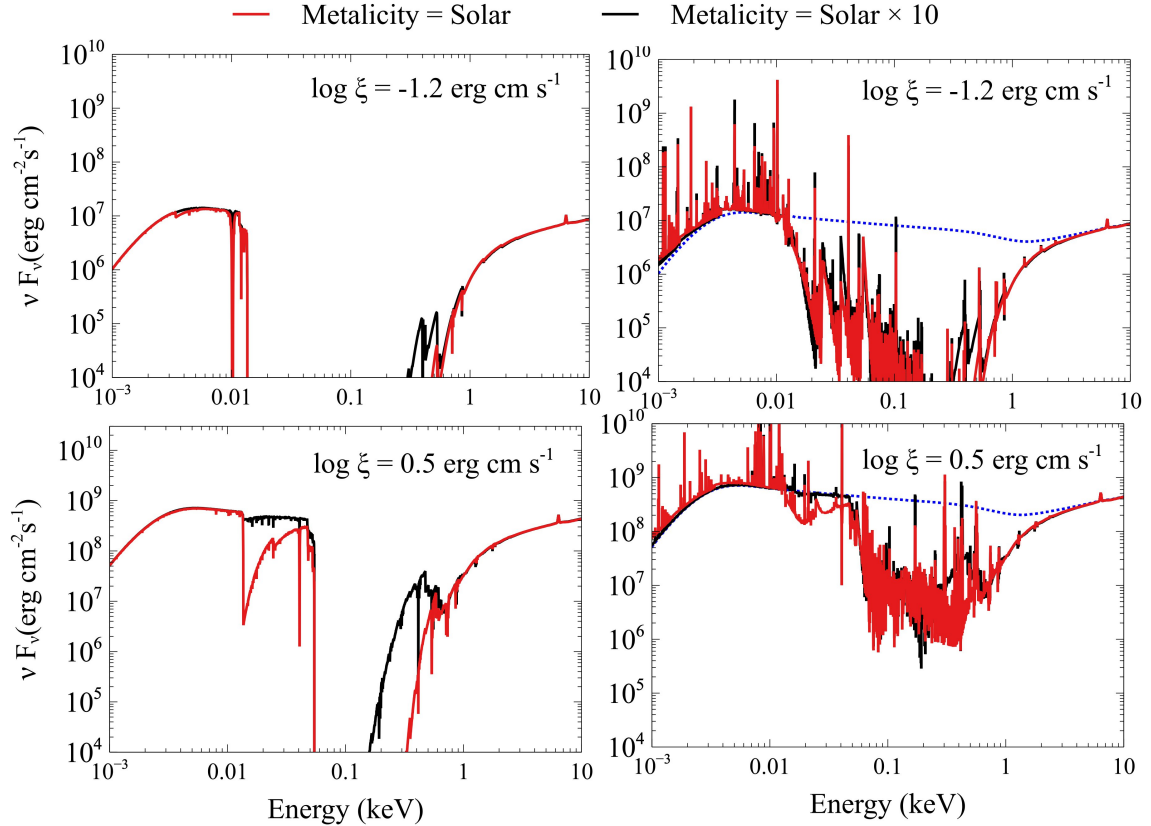


Figure 5.7: Changes in the SED for different values of the metallicity for two models of ionization parameters. Both upper panels have ionization parameter $\log \xi = -1.2 \text{ erg cm s}^{-1}$. Upper left panel shows the results for the transmitted SED and the upper right shows the results for the total emission from the obscurer (sum of the transmitted and reflected continua plus attenuated incident continuum). Lower panels show the same concept for an ionization parameter $\log \xi = 0.5 \text{ erg cm s}^{-1}$.

5.3 LIMITS ON THE OBSCURER: THE GLOBAL COVERING FACTOR

While the obscurer’s properties such as its hydrogen density and ionization parameter play a pivotal role in determination of the shape of the transmitted/reflected SED, we still need to know another characteristic of the obscurer, its global covering factor, to determine the geometry of the obscurer.

As seen from Earth, the obscurer in NGC 5548 absorbed a great deal of the energy emitted by the AGN since the ionizing photon luminosity fell from $2 \times 10^{44} \text{ erg s}^{-1}$ to roughly $7.7 \times 10^{43} \text{ erg s}^{-1}$ after obscuration (based on the SED modeling of Mehdipour et al. (2016)). The obscurer removed roughly $11.2 \times 10^{43} \text{ erg s}^{-1}$, as seen by us if it fully covers the continuum source. Energy is conserved, so this light must be reradiated.

The total energy absorbed and emitted by the obscurer is determined by its global covering factor (explained in section 2.2), which is unknown. However, we do know that it persists for several orbital timescales (Kaastra et al. 2014) so the geometry may be some-

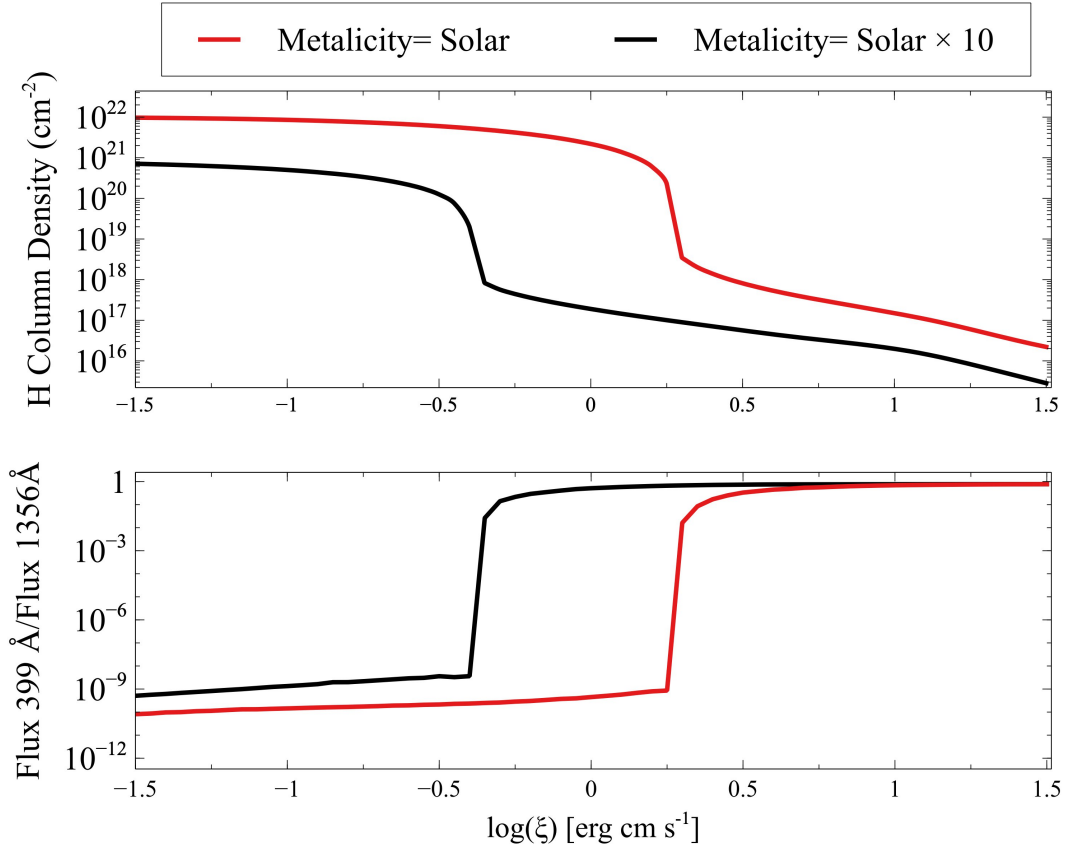


Figure 5.8: Top panel shows the variation of the obscurer atomic hydrogen column density as the ionization parameter changes for two different values of the metallicity. The bottom panel shows the ratio of the 399Å/1365Å transmitted continuum as a function of the ionization parameter.

thing like a symmetric cylinder covering 2π around the equator (Figure 1 of D19b). This suggests that the GCF may be significant. To check this, we derive the emission-line luminosities predicted by the LOS obscurer model to examine its spectrum and establish an upper limit on the LOS obscurer global covering factor.

5.3.1 The Luminosity of the Obscurer

Here we vary the distance between the obscurer and the central black hole (R_{obs}) to judge the magnitude of the effect on the obscurer's emission lines. The most significant impact of doing this is to change the ionization parameter since it is proportional to R_{obs}^{-2} . The location of the wind in NGC 5548 is fairly well known. There is spectroscopic evidence showing the wind is located between the BLR and the source (i.e. $R_{\text{obs}} < 10^{16}$ cm). However, this is not the case for all AGNs, so it is informative to show how variations of the distance affect some of the wind's properties to establish a diagnostic for other studies. Here we illustrate a novel method that uses limits to line intensities to establish bounds on the global covering factor and the location of the wind.

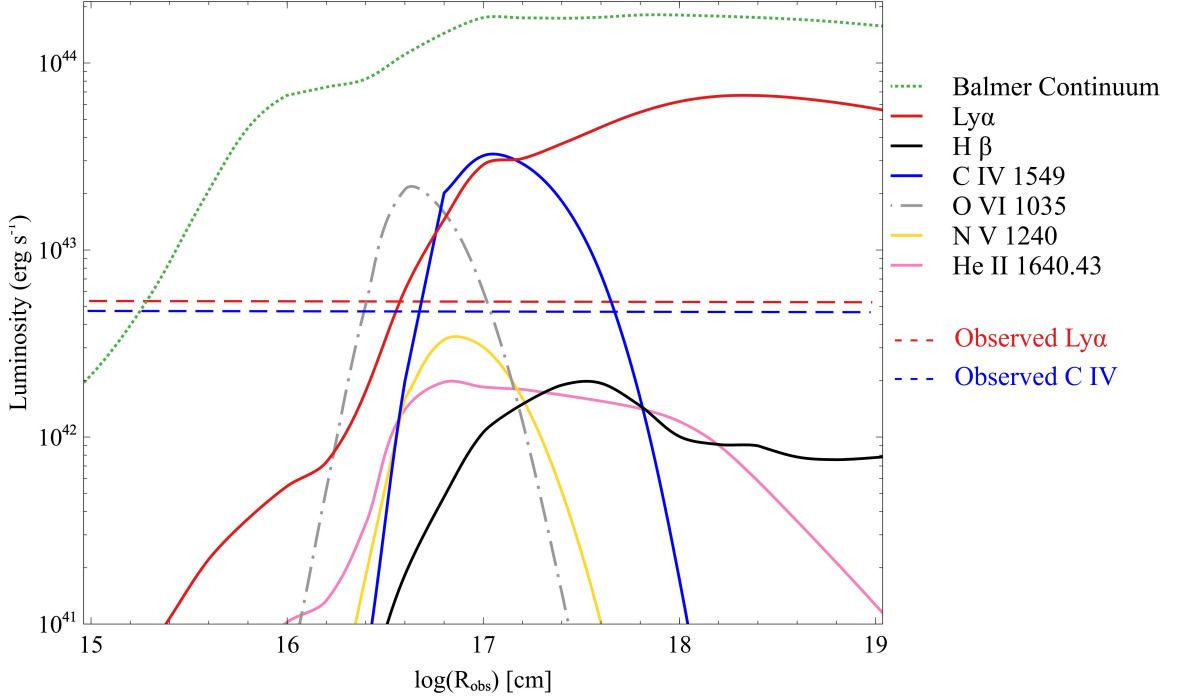


Figure 5.9: Changes in the luminosity of the emission features of the obscurer as the separation between the obscurer and the black hole varies between 10^{15} and 10^{19} cm. The luminosities are predicted for full source coverage. The observed values refer to a combination of broad, medium broad, and very broad emission components observed by HST.

Figure 5.9 shows predicted emission-line luminosities for an obscurer that fully covers the continuum source, a GCF of 100% and has a hydrogen density of 10^{10} cm^{-3} . To create the model we considered a constant optical depth at 1 keV.

The predicted luminosities in Figure 5.9 can be compared with observations to obtain an upper limit to the obscurer’s GCF. The range of radii corresponds to changing the ionization parameter by a factor of 10^8 . The strongest spectral features are the Balmer continuum, $\text{Ly}\alpha$, C IV, and O VI. Of these, the Balmer continuum and $\text{Ly}\alpha$ have the least dependence on the unknown radius. We can compare the observed luminosity of $\text{Ly}\alpha$ with these predictions to set an upper limit on the obscurer’s GCF.

Table 1 of Kriss et al. (2019) lists the UV emission lines in NGC 5548. Based on this information, the observed flux (broad+medium broad+very broad) for $\text{Ly}\alpha$ is $8.14 \times 10^{-12} \text{ erg cm}^{-2} \text{ s}^{-1}$ (after correction for foreground Milky Way Galaxy extinction), and for the luminosity distance given by Mehdipour et al. (2015), it has a luminosity of $5.36 \times 10^{42} \text{ erg s}^{-1}$. This value is shown with a red dashed line in Figure 5.9. The predicted $\text{Ly}\alpha$ luminosity can be either smaller or larger than this value. The Figure shows that we predict a $\text{Ly}\alpha$ luminosity of $\sim 5.46 \times 10^{41} \text{ erg s}^{-1}$ for $R_{\text{obs}} = 10^{16} \text{ cm}$ and full coverage. This value is almost 10 times smaller than that observed. It means that, based on the $\text{Ly}\alpha$ luminosity, if the obscurer is located at 10^{16} cm from the source, there is no need to constrain its GCF. If the same obscurer is located farther away, at $R_{\text{obs}} = 10^{17} \text{ cm}$ for instance, the predicted value is $\sim 2.85 \times 10^{43} \text{ erg s}^{-1}$. This limits the obscurer global covering factor to be less

than $\sim 19\%$. This shows that there is an interplay between the location of the obscurer, the emission line luminosities, and its global covering factor.

The CIV line is much more model sensitive due to its dependence on the ionization parameter. Based on table 1 of Kriss et al. (2019), the CIV flux (broad+medium broad+very broad) is $7.17 \times 10^{-12} \text{ erg cm}^{-2} \text{ s}^{-1}$ (after correction for foreground Milky Way Galaxy extinction), and this leads to a luminosity of $4.72 \times 10^{42} \text{ erg s}^{-1}$. Figure 5.9 shows that the predicted emission line luminosity varies by many orders of magnitude. For $R_{\text{Obs}} = 10^{16} \text{ cm}$, the predicted CIV line luminosity, is much smaller than the observed value, as indicated by the blue dashed line. This means that GCF can be as large as 100%. For larger radii, corresponding to smaller ionization parameters, the luminosity increases, reaching a maximum CIV luminosity of $3.19 \times 10^{43} \text{ erg s}^{-1}$, almost 7 times brighter than the observed value, requiring a covering factor less than one. We come away with the picture that the emission from the obscurer can be a contributor to the observed broad emission, and could, in fact, account for all of it, depending on the location of the obscurer. Next we investigate how the emission from the obscurer varies as a function of both its location and hydrogen density, for the three different cases discussed earlier.

5.4 EMISSION FROM THE WIND

D19b proposed that changes occurring in the base of the disk wind, the equatorial obscurer, explains the BLR holiday. This obscurer is located close to the central source and is assumed to absorb a significant amount of the SED striking the BLR. To conserve the energy, the obscurer must re-emit this energy. D20 showed that the equatorial obscurer produces its own emission lines and came up with a model in which the obscurer is not a dominant contributor to most of the strong emission lines, while it can be considered as the main He II and Fe $K\alpha$ emission source. In their model, the emission lines observed are indeed a combination of a broad core (produced in the BLR) and a very broad base (produced by the equatorial obscurer). Below we investigate various emission lines produced by the equatorial obscurer in each of the three cases that were discussed earlier.

5.4.1 Very broad emission lines

Figures 5.10 to 5.15 illustrate emission line equivalent widths for a variety of lines. Each of these Figures belongs to a single emission line and shows its behavior for the obscurer in Case 1, 2, or 3. To produce three different Cases, the optical depths are chosen such that each model of the obscurer falls in the middle of each region of figure 4 in D19b. This leads to a typical example of an obscurer for each case.

In each panel, the EW of the emission line is modeled as a function of both the flux of photons produced by the source ($\phi(\text{H})$) and the hydrogen density. To create these models, we used the SED of Mehdipour et al. (2015) in `CLOUDY` (developer version), while we assumed photospheric solar abundances (Ferland et al. 2017). We produced two-dimensional grids of photoionization models as we have done in D20. Each grid includes a range of total hydrogen density, $10^{10} \text{ cm}^{-3} < n(\text{H}) < 10^{18} \text{ cm}^{-3}$, and a range of incident ionizing

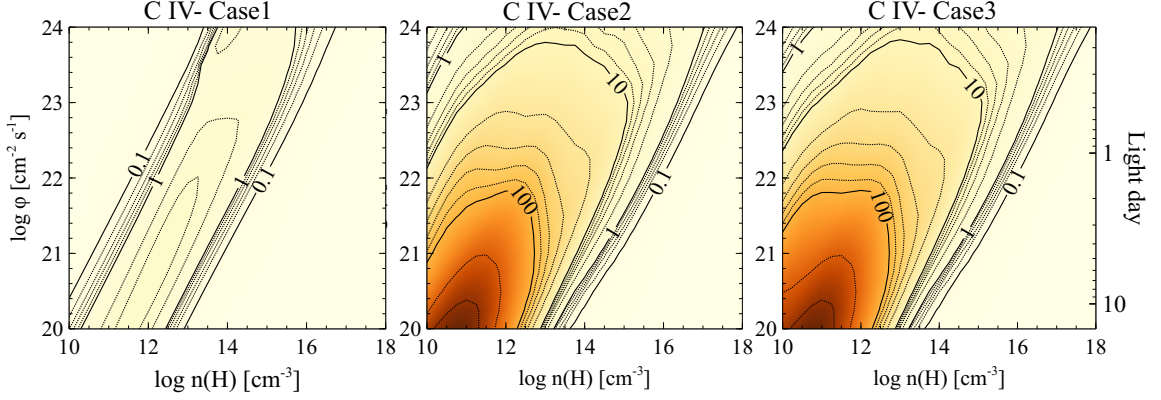


Figure 5.10: The EW of CIV emission line as a function of both the flux of hydrogen ionizing photons and the hydrogen density. Different panels show the variation of the EW for each of the discussed cases. The intervals between decades are logarithmic in 0.2 dex steps.

photon flux, $10^{20} \text{ s}^{-1} \text{ cm}^{-2} < \phi(\text{H}) < 10^{24} \text{ s}^{-1} \text{ cm}^{-2}$. The flux of ionizing photons, the total ionizing photon luminosity $Q(\text{H})$, and the distance in light days are related by:

$$\phi(\text{H}) = \frac{Q(\text{H})}{4\pi r^2}, \quad (5.16)$$

which indicates when the obscurer is closer to the source (smaller r), it will receive a larger amount of ionizing photon flux (larger $\phi(\text{H})$).

Considering the CIV lag and based on Figure 4 of D20, the CIV-forming region of the BLR has an incident ionizing photon flux of approximately $10^{21} \text{ cm}^{-2} \text{ s}^{-1}$, while the equatorial obscurer has an incident ionizing flux of almost $10^{22.5} \text{ cm}^{-2} \text{ s}^{-1}$, which means the equatorial obscurer is ~ 6 times closer to the central source than a typical point in the BLR. Such an obscurer emits lines with a FWHM ~ 4 time broader than the BLR if motions are virialized. As proposed by D20, the line EWs observed by HST and other space telescopes are a combination of the broad emission from the BLR and the very broad emission from the equatorial obscurer.

As Figures 5.10 to 5.13 show, when the wind is in a transparent state (Case 1), it emits very small amounts of CIV, HeII, $\text{Ly}\alpha$ and SiIV. In such a situation, almost all of the observed (broad+very broad) emission lines are mainly broad emission produced by the BLR and the equatorial obscurer has almost no contribution, regardless of where it is located or what its density is. This may be the case in most AGNs. However, when in Case 2 state, the contribution of the obscurer becomes significant. This means that by transformation from Case 1 to Case 2, there will be a change in the observed EW of the mentioned lines, which may lead to a holiday.

The predictions are different for Fe $\text{K}\alpha$ and $\text{H}\beta$ (Figures 5.14 and 5.15) emission lines. A transparent disk wind which is located close enough to the central source ($\phi(\text{H}) > 10^{21} \text{ s}^{-1} \text{ cm}^{-2}$) with a relatively low density ($n(\text{H}) < 10^{12} \text{ cm}^{-3}$) (Figure 5.14, Case 1, upper left corner) will produce Fe $\text{K}\alpha$ as much as a translucent disk wind. In this regime, the ions are too highly ionized to permit the Auger effect. Meanwhile, line photons are still affected

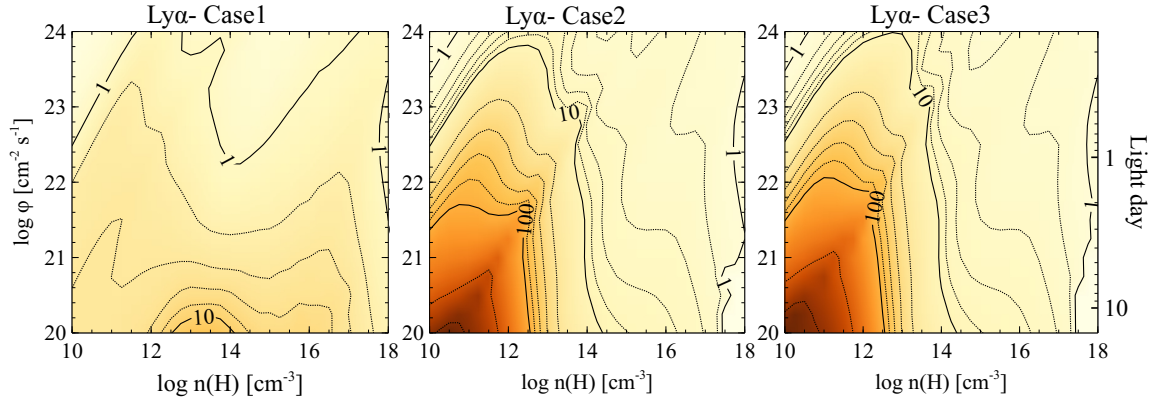


Figure 5.11: The EW of Ly α emission line as a function of both the flux of hydrogen ionizing photons and the hydrogen density. Different panels show the variation of the EW for each of the discussed cases.

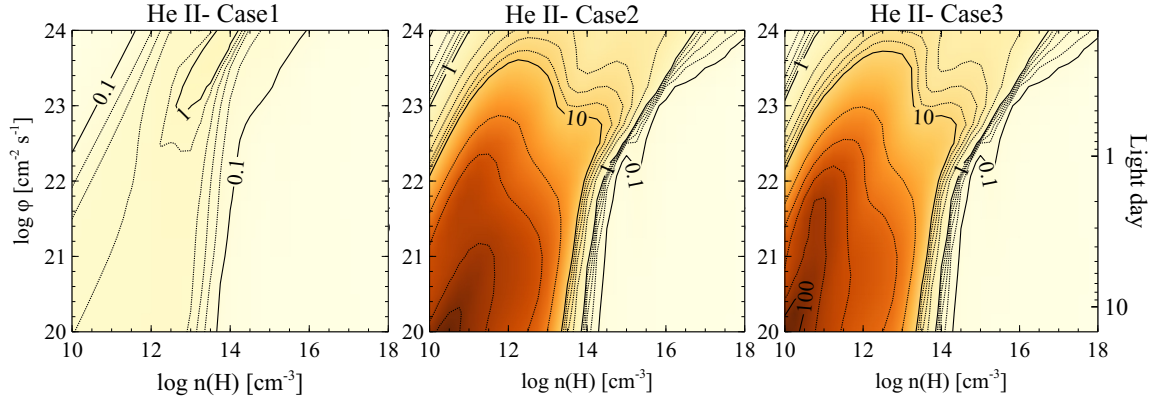


Figure 5.12: The EW of He II emission line as a function of both the flux of hydrogen ionizing photons and the hydrogen density. Different panels show the variation of the EW for each of the discussed cases.

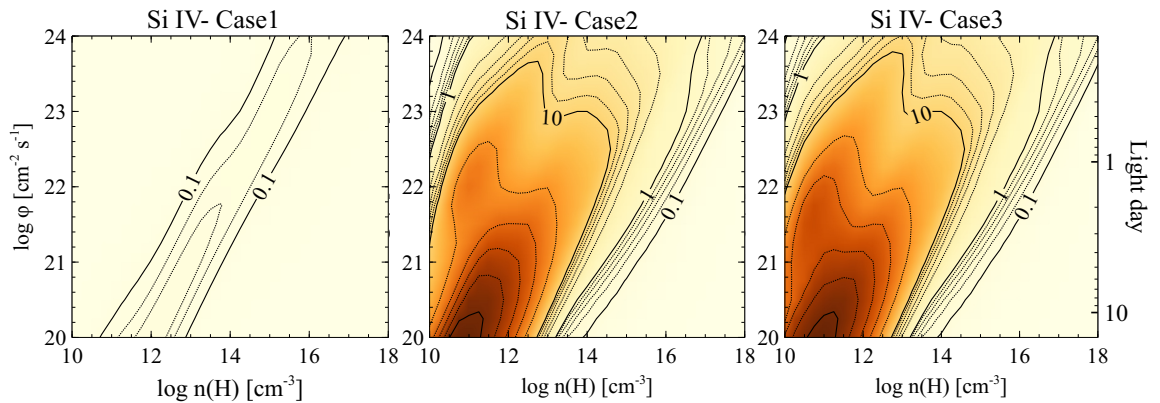


Figure 5.13: The EW of Si IV emission line as a function of both the flux of hydrogen ionizing photons and the hydrogen density. Different panels show the variation of the EW for each of the discussed cases.

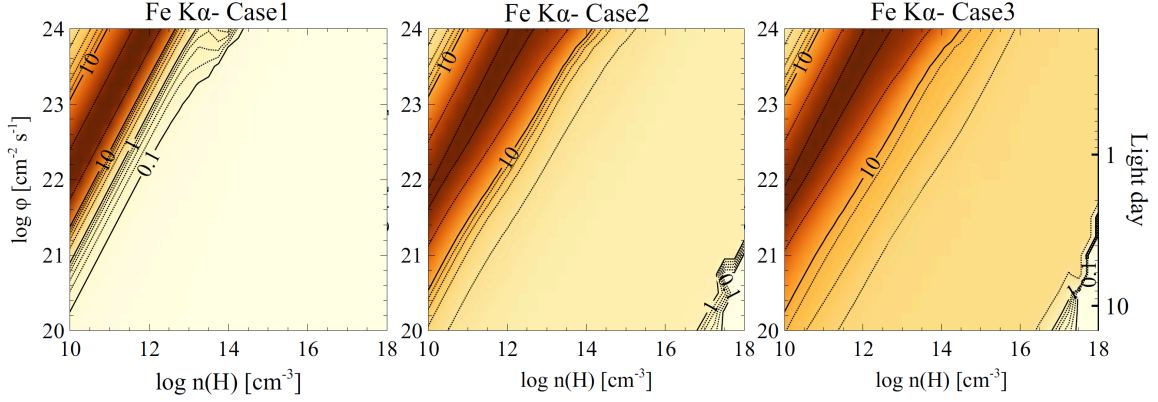


Figure 5.14: The EW of Fe K α emission line as a function of both the flux of hydrogen ionizing photons and the hydrogen density. Different panels show the variation of the EW for each of the discussed cases.

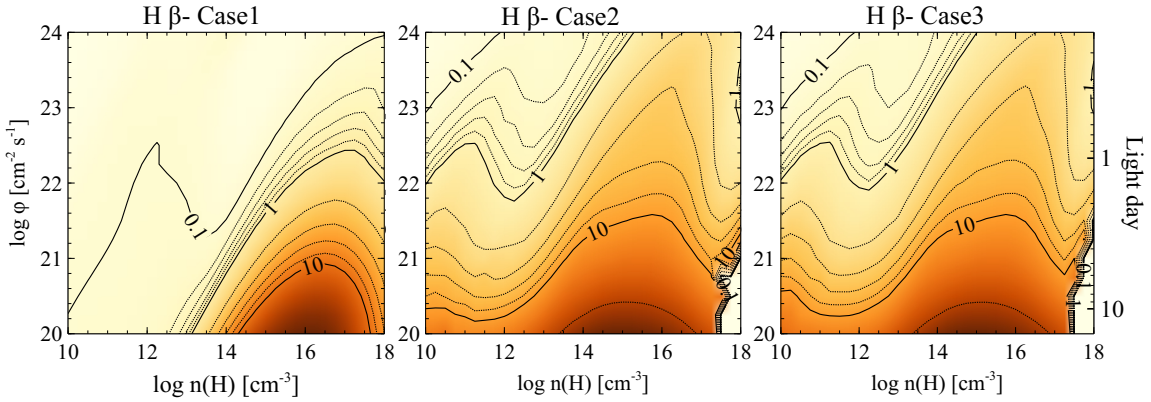


Figure 5.15: The EW of H β emission line as a function of both the flux of hydrogen ionizing photons and the hydrogen density. Different panels show the variation of the EW for each of the discussed cases.

by resonant scattering. There is no destruction mechanism so they can leave the disk. As a result, Fe K α XXV and XXVI will be emitted at 6.67 keV and 6.97 keV (Reynolds & Nowak 2003). In this case, and based on the discussion of D20, both transparent and translucent disk winds can be a major contributor to the observed Fe K α emission. For NGC 5548, this confirms that the total amount of observed Fe K α will be almost constant before, during or after the holiday. Indeed, it does not matter which Case the wind state is in, it will always produce roughly the same amount of Fe K α .

A transparent wind which is located far enough from the source ($\phi(\text{H}) < 10^{22}\text{s}^{-1}\text{cm}^{-2}$) with a large enough density ($n(\text{H}) > 10^{14}\text{cm}^{-3}$) would produce almost as much H β as produced by a translucent wind (Figure 5.15, Case 1, lower right corner). Table 6 of Pei et al. (2017) reports that the flux of H β had the smallest change (6%) among the other strong emission lines (CIV, HeII, Ly α and SiIV). This is consistent with the behavior of H β in our model, in which by transforming the wind from Case 1 (non-holiday) to Case 2 (holiday) the amount of H β emitted by the equatorial obscurer is not affected dramatically, how-

ever, as we mentioned earlier, it is still affected enough to be consistent with the observed emission-line holiday. Depending on the optical depth, a translucent wind can be considered as Case 2 or Case 3. As Figures 5.10 to 5.15 show, for all of the emission lines, the behavior of a Case 2 obscurer is very similar to that of Case 3. D20 explained that a Case 3 wind could be a contributor to the changing-look phenomenon.

5.4.2 Summary

The equatorial obscurer is located close to the central source and, depending on whether it is transparent or translucent, it absorbs a small or large portion of the SED striking the BLR. The obscurer conserves energy by emitting very broad emission lines which are explained and investigated by D20. For several of the strong UV emission lines, when the obscurer transforms from normal to a holiday phase, there is an increase in the very broad component, since the obscurer absorbs more energy than before. At the same time, the EWs of BLR broad emission components decrease due to receiving less energy from the source. The combination of these two phenomena leads to a decrease in the total (broad + very broad) observed emission line, i.e. a holiday. For some other lines, such as Fe $K\alpha$ and H β , the obscurer always emits almost the same amount of very broad emission line. This means its phase will not have any effects on absorbing that specific energy. As a result, it will not have a considerable effect on the BLR energy, and the total observed EWs of these lines seem almost constant during the transformation from normal to the holiday, and vice versa.

Chapter 6 CONCLUSION

During my PhD studies, I performed a systematic study of the NGC 5548 observational data obtained by two major campaigns (STORM and anatomy) during 2013 and 2014. This study includes modeling the multi-wavelength spectra and creating `Cloudy` simulations to predict the behavior of the AGN in order to provide a physical explanation for the unique observations.

The astonishing results from the STORM and anatomy campaigns have shown that an unexpected heavy obscuration is observed in both UV and X-rays. The other unforeseen outcome was the never-before-seen decorrelation between the broad emission lines and the continuum. The same thing happened for some of the narrow absorption lines and the continuum. These unusual behaviors are called "the holidays" and need to be explained.

I propose that the obscuration is a result of the presence of a disk wind which arises from the accretion disk. The wind acts like a shield preventing the BLR from receiving the original SED (cloud shadowing). I model the behaviour of the wind and predict its effects on the intrinsic SED. I show that changes in the covering factor of the upper part of the wind result in the decorrelation between the high ionization absorption lines and the continuum (the absorption-line holiday), while instabilities in the density of the lower part of the wind reproduces the emission line holiday.

I also show that the variations of the clouds' characteristics result in a different situation that can affect the state of the observations. There are times in which the wind is almost transparent, and so has no effect on the transmitted SED. Regarding NGC 5548, this can be the case before 2011/2012 when there were no heavy obscuration. This might be the case in most AGNs in which no holidays are observed.

In some other cases, the wind gets denser, or has a lower ionization parameter, so it will absorb a great deal of the intrinsic continuum. In such cases a holiday will happen and the behavior of the lines will differ from what is expected. There are also more extreme cases in which the obscurer is very dense or less ionized so the transmitted SED is significantly affected. I propose this might be a contributor to the changing look phenomenon.

The present simulations lead to novel approaches to probe the evolution of the winds and predict their existence while there are only single spectra data available. I also provide an atlas of spectra simulations which serves as a guide to future reverberation campaigns.

Based on the results presented here, it is clear that cloud shadowing plays a pivotal role in AGN variability. Clouds/winds might cover a major part of the intrinsic SED and thus dramatically affect the expected absorption and emission features. Such winds will have their own emission lines that form a very broad baseline in the observed line profiles. Disk winds are common, so holidays might be common as well. It means it is essential to consider cloud shadowing in all AGN studies.

Bibliography

- Antonucci, R., & Barvainis, R. 1988, *ApJL*, 332, L13
- Arav, N., Barlow, T. A., Laor, A., et al. 1998, *MNRAS*, 297, 990
- Arav, N., Chamberlain, C., Kriss, G. A., et al. 2015, *A&A* 577, 37
- Baldwin, J., Ferland, G., Korista, K., & Verner, D. 1995, *ApJL*, 455, L119
- Bentz, M. C., & Katz, S. 2015, *PASP*, 127, 67
- Bentz, M.C., Walsh, J.L., Barth, A.J., et al. 2009, *ApJ*, 705, 199
- Blandford, R.D., & McKee, C.F. 1982, *ApJ*, 255, 419
- Cappi, M., De Marco, B., Ponti, G., et al. 2016, *A&A* 592, A27
- Chelouche, D., Pozo Nuñez, F., Kaspi, Sh. 2019, *NatAs*, 3, 251
- Crenshaw, D. M., Kraemer, S. B., et al. 2003, *ApJ*, 594, 116
- Crenshaw, D. M., Kraemer, S. B., et al. 2009, *ApJ*, 698, 281
- Crudace, R., Paresce, F., Bowyer, S., Lampton, M. 1974, *ApJ*, 187, 497
- Dehghanian, M., Ferland, G. J., Kriss, G. A., et al. 2019a, *ApJ*, 877, 119
- Dehghanian, M., Ferland, G. J., Peterson, B. M., et al. 2019b, *ApJL*, 882, L30
- Dehghanian, M., Ferland, G. J., Kriss, G. A., et al. 2020a, *ApJ*, 898, 141
- Dehghanian, M., Ferland, G. J., Peterson, B. M., et al. 2021, *ApJ* 906, 14
- De Rosa, G., Peterson, B. M., Ely, J., et al. 2015, *ApJ*, 806:128
- Dexter, J. & Agol, E. 2011, *ApJ*, 727L, 24D
- Di Gesu, L., Costantini, E., Ebrero, J., et al. 2015, *A&A* 579, A42
- Ebrero, J., Kaastra, J.S., Kriss, G.A., et al. 2016, *A&A*, 587, A129
- Edelson, R., Gelbord, J. M., Horne, K., et al. 2015, *ApJ*, 806, 129
- Edelson, R., Gelbord, J. M., Cackett, E., et al. 2018, *arXiv:1811.07956*
- Fausnaugh, M. M., Denney, K. D., Barth, A. J., et al. 2016, *ApJ*, 821, 56
- Ferland, G. J. & Mushotzky, R. F. 1982, *ApJ*, 262, 564
- Ferland, G. J., Korista, K. T., Peterson, B. M. 1990, *ApJ*, 363L, 21

Ferland, G. J., Peterson, B. M., Horne, K., et al. 1992, ApJ, 387, 95

Ferland, G. J. 2003, ARA&A, 41, 517

Ferland, G. J., Chatzikos, M., Guzmán, F., et al. 2017, RMxAA, 53, 385

Ferrarese, L. & Merritt, D. 2000, ApJ, 539L, 9

Gardner, E. & Done, C. 2017, MNRAS, 470, 3591

Gaskell, C.M. 2017, MNRAS, 467, 226

Gaskell, C.M. & Harrington, P. Z. 2018, MNRAS, 478, 1660

Gaskell, C.M. & Klimek, E. S., 2003, A&AT, 22, 661G

Gebhardt, K., Bender, R., Bower, G., Dressler, A., et al., 2000, ApJ, 539L, 13

Gebhardt, K., Kormendy, J., Ho, L. C. et al. 2000a, ApJ, 543L, 5

Giustini, M. & Proga, D. 2019, A&A, 630A, 94

Goad, M., Korista, K. T., De Rosa, G., et al. 2016, ApJ, 824, 11

Goad, M. R., Knigge, C., Korista, K. T., Cackett, E., et al. 2019, MNRAS, 10, 1093

Goad, M., O'Brien, P. T., Gondhalekar, P.M. 1993, MNRAS, 263, 149

Goad, M. and Koratkar, A. 1998, ApJ, 495, 718

Häring, N., Rix, H., 2004, ApJ, 604L, 89

Hopkins, P. F., Strauss, M. A., Hall, P. B.; Richards, et al. 2004, ApJ, 128, 112H

Horne, K., Peterson, B. M., Collier, S. J., et al. 2004, PASP, 116, 465

Horne K., De Rosa, G., Peterson, B.M., et al. 2020, submitted to ApJ (arXiv:2003.01448)

Kaastra, J., S., Kriss, G. A., Cappi, M., et al. 2014, Science, 345, 64

King, A. 2003, ApJL, 596, L27. doi:10.1086/379143

Korista, K., Baldwin, J., Ferland, G., et al. 1997, ApJS, 108, 401

Kormendy, J. & Richstone, D. 1995, ARA&A, 33, 581

Kaastra, J. S., Mewe, R., Liedahl, D. A., et al. 2000, A&A, 345, 83

Kallman, T & Bautista, 2001, ApJS, 133, 221

Kaspi, Sh. Netzer, H. 1999, ApJ, 524, 71

Korista, K. T. & Goad, M. R. 2000, ApJ, 536, 284

Korista, K. T. & Goad, M. R. 2001, ApJ, 553, 695

Korista, K. T. & Goad, M. R. 2019, MNRAS, 489, 5284

Kriss, G.A., De Rosa, G., Ely, J., et al. 2019, in preparation

Lawther, D., Goad, M. R., Korista, K. T., et al. 2018, MNRAS, 481, 533

Leighly, K.M. 2004, ApJ, 611, 125

Lodders, K. 2003, ApJ, 591, 1220

Lynden-Bell, D. 1969 Nature 223, 690

Magorrian, J., Tremaine, S., Richstone, D., et al. 1998, AJ, 115, 2285

Mathews, W. G. & Blumenthal, G. R. 1977, ApJ, 214: 10

Mathews, W. G.; Ferland, G. J. 1987, ApJ, 323:456M

Mathur, S., Elvis, M. & Wilkes, B. 1995, ApJ, 452:230

Mathur, S., Elvis, M. & Wilkes, B. 1999, ApJ, 519:605

Mathur, S., Gupta, A., Page, K., et al. 2017, ApJ, 846:55

McLure, R. J. & Dunlop, J. S., 2004, MNRAS.352.1390

Mehdipour, M., Kaastra, J., S., Kriss, G. A., et al. 2015, A&A, 575, 22

Mehdipour, M., Kaastra, J., S., Kriss, G. A., et al. 2016, A&A, 588, 139

Murray, N., Chiang, J., Grossman, S. A., Voit, G, M. 1995, ApJ, 451, 498

Osterbrock D. E., & Ferland G. J., 2006, *Astrophysics of Gaseous Nebulae and Active Galactic Nuclei*, 2nd ed., Univ. Science Books, CA, Herndon, VA

Pei, L., Fausnaugh, M. M., Barth, A. J., et al. 2017, ApJ, 837: 131

Peterson, B.M. 1993, PASP, 105, 247

Peterson, B. M. 1997, An introduction to active galactic nuclei, Publisher: Cambridge, New York Cambridge University Press, 1997 Physical description xvi, 238 p. ISBN 0521473489

Peterson, B. & Grier, C. 2012, Proceedings of Nuclei of Seyfert galaxies and QSOs - Central engine & conditions of star formation (Seyfert 2012). 6-8 November, 30

Peterson, B.M., Denney, K.D., De Rosa, G, et al. 2013, ApJ, 779:109

Peterson, B. M., Ferrarese, L., Gilbert, K. M., et al. 2004, ApJ, 613, 682

PROGA, D., & Kallman, T. R. 2004, ApJ, 616, 688

Reynolds, C. S. & Nowak, M. A. 2003, PhR, 377, 389

Ride, S. K. & Walker, J. R. 1977, A&A, 61, 347

Shemmer, O., Lieber, S. 2015, ApJ, 805, 124

Shields, J. C., Ferland, G. J., Peterson, B. M. 1995, ApJ, 441, 507

Sim, S. A., Proga, D., Miller, L., Long, K. S., & Turner, T. J. 2010, MNRAS, 408, 1396

Starkey, D., Horne, K., Fausnaugh, M. M., et al. 2017, ApJ, 835: 65

Sun, M., Xue, Y., Cai, Z. & Guo, H. 2018, ApJ, 857:86

Tarter, C. B., Tucker, W. H. & Salpeter, E. E. 1969, ApJ, 156, 943

Tatum, M. M., Turner, T. J., Sim, S. A., et al. 2012, ApJ, 752, 94

Ursini, F., Boissay, R., Petrucci, P.-O., et al. 2015, A&A, 577, A38

Wang, Y., Ferland, G. J., Hu, C., et al. 2012, MNRAS, 424, 2255

Whewell, M., Branduardi-Raymont, G., Kaastra, J.S., et al. 2015, A&A, 581, A79

Williams, P. R., Pancoast, A., Treu, T., et al. 2020, ApJ, 902, 74

Vita

Educational institutions attended:

- ✓ M. Sc. in Physics, University of Kentucky, USA, 2018
- ✓ M. Sc. in Particle Physics, Sabzevar University, Iran, 2012
- ✓ B. Sc. in Physics, University of Kashan, Iran, 2008

Professional positions held:

- ✓ May 2020-Present: Graduate Research Associate, Department of Physics and Astronomy, UKy
- ✓ May 2019-May 2020: MacAdam Fellowship, Department of Physics and Astronomy, UKy
- ✓ Jan 2017-May 2019: Graduate Research Associate, Department of Physics and Astronomy, UKy
- ✓ Sep 2016- Jan 2017: Graduate Teaching Associate, Department of Physics and Astronomy, UKy

Awards and honors:

- ✓ Keith B. MacAdam Graduate Excellence Fellowship, the University of Kentucky, 2019
- ✓ Max Steckler Fellowship, the University of Kentucky, 2017
- ✓ Best presented poster, 2nd National particle physics Conference, Iran, 2011

Publications:

- ✓ “Space Telescope and Optical Reverberation Mapping Project. XIII. An Atlas of UV and X-ray Spectroscopic Signatures of the Disk Wind in NGC 5548”, Dehghanian et al., (10 more authors), 2021, ApJ, 906, 14 (15pp)
- ✓ “Space Telescope and Optical Reverberation Mapping Project. XII. Broad-line Region Modeling of NGC 5548”, Williams. et al (157 more authors including Dehghanian, M), ApJ, 902, 74 (26 pp)
- ✓ “Space Telescope and Optical Reverberation Mapping Project. XI. Disk-wind characteristics and contributions to the very broad emission lines of NGC 5548”, Dehghanian et al., (24 more authors), 2020a, ApJ, 898, 141 (8pp).
- ✓ “A wind-based unification model for NGC 5548: spectral holidays, non-disk emission, and implications for changing-look quasars”, Dehghanian, M., et al. (11 more authors),

2019b, ApJL, 882, 30 (6 pp).

✓“Space Telescope and Optical Reverberation Mapping Project. X: Understanding the Absorption-Line Holiday”, Dehghanian, M., et al. (29 more authors), 2019, ApJ, 877, 119 (10pp).

✓“Space Telescope and Optical Reverberation Mapping Project. IX. Velocity-Delay Maps for Broad Emission Lines in NGC 5548”, Horne, K. et al. (157 more authors, including Dehghanian, M) 2020arXiv200301448.

✓“Current and future development of the photoionization code Cloudy”, van Hoof, P.A.M., Van de Steene, G.C., Guzman, F., Dehghanian, M., M. Chatzikos and G.J. Ferland, 2019, accepted for publication in Spectral Line Shapes in Astrophysics and Related Topics.

✓“Space Telescope and Optical Reverberation Mapping Project. VIII. Time Variability of Emission and Absorption in NGC 5548 Based on Modeling the Ultraviolet Spectrum”, Kriss, G. A., et al. (166 more authors, including Dehghanian, M.), 2019, ApJ, 881, 153 (36 pp).

✓“H-, He-like recombination spectra - III. n-changing collisions in highly excited Rydberg states and their impact on the radio, IR, and optical recombination lines”, Guzmán, F.; Chatzikos, M., van Hoof, P. A. M., Balser, Dana S., Dehghanian, M., Badnell, N. R., Ferland, G. J., 2019, MNRAS, 486, 1003(16 pp).

Conference papers:

✓“HST insights into the missing piece of the AGN feedback puzzle: The role of disk winds”, Dehghanian, M. Ferland, G. J., Kriss, G. A., Peterson, B. M., Guzman, F., Chatzikos, 2020, AAS235, 52, 436.09

✓“The impact of inaccurate collisional excitation rates on radio recombination line observations”, Guzmán, F.; Chatzikos, M., van Hoof, P. A. M., Balser, Dana S., Dehghanian, M.; Badnell, N. R., Ferland, G. J., 2019, AAS233, id.412.08

✓“Uncorrelated behavior of narrow absorption Line in NGC5548”, Dehghanian, M.; Ferland, G. J., Kriss, G. A., Peterson, B. M., Guzman, F., Chatzikos, M., Van Hoof, P., 2019, AAS233, id.243.11